Inaugural Dissertation

for
obtaining the doctoral degree
of the
Combined Faculty of Mathematics, Engineering and Natural Sciences
of the
Ruprecht - Karls - University
Heidelberg

Presented by
Elisa Heinzelmann, M.Sc.
born in Crailsheim, Germany

Oral examination:
31st March, 2023

The role of MYT1L in brain tumor formation, progression and plasticity

Referees:
Prof. Dr. Henrik Kaessmann
Prof. Dr. Peter Angel

SUMMARY

Glioblastoma multiforme (GBM) is a devastating type of brain cancer characterized by infiltrative and aggressive growth. Transcriptional dysregulation is likely a key regulator of tumor initiation and plasticity. One transcription factor that has emerged as a potential novel regulator of these processes is myelin transcription factor 1-like (MYT1L). While it has been shown that MYT1L can drive neuronal differentiation and may play a role in suppressing GBM, it remains unclear whether MYT1L can also regulate tumor initiation and/or glioma cell plasticity.

In my doctoral study, I investigated whether loss of MYT1L can induce tumor formation in post-mitotic neurons and whether MYT1L regulates GBM subtype identity.

Genetic deletion of MYT1L in mature neurons of adult mice impaired the expression of neuronal genes but did not induce brain tumor formation. Unexpectedly, I found that genetic deletion of the tumor suppressors PTEN and TP53 could induce tumor formation in post-mitotic neurons. Additional deletion of MYT1L resulted in enhanced lethality and sudden death of mice.

In a cerebral organoid model, I examined the effects of MYT1L on human brain tumorigenesis. In this model, loss of MYT1L in combination with mutation of canonical GBM tumor suppressors caused increased cell expansion, supporting the hypothesis that MYT1L is a brain tumor suppressor. Furthermore, MYT1L overexpression in patient-derived glioma cell lines decreased cell invasion and proliferation. Mechanistically, activator/Repressor-fusion experiments showed that MYT1L acts predominantly as a transcriptional repressor to downregulate proliferation and invasion. To further explore the molecular mechanism of MYT1L on glioma cell fate, I performed transcriptomic analysis. Interestingly, gene signature analysis revealed that MYT1L switched the identity from a mesenchymal-like GBM subtype towards a proneural/NPC-like GBM subtype, a cancer subtype with better prognosis. The correlation of MYT1L expression in the proneural subtype was also found in patient datasets.

Overall, my work uncovered a novel mechanism in which MYT1L blocks cell fate plasticity to prevent dedifferentiation and tumor initiation and highlights MYT1L as a potential and repressive master regulator of NPC-like cell states in glioblastoma. These findings might lead towards subtype-specific treatments for glioma patients, which could prevent tumor progression towards more severe subtypes.

ZUSAMMENFASSUNG

Glioblastoma multiforme (GBM) wird zu der schlimmsten Art von Gehirntumoren gezählt und ist durch aggressives und infiltratives Wachstum gekennzeichnet. Ein entscheidender Faktor in der Tumorentstehung und der Plastizität der Tumore ist höchstwahrscheinlich die Dysregulation von transkriptionellen Prozessen. Ein potenzieller neuer Regulator dieser Prozesse ist der Transkriptionsfaktor MYT1L. MYT1L kann die neuronale Differenzierung fördern und spielt eine Rolle bei der Unterdrückung von Gehirntumoren, jedoch ist unklar, ob MYT1L auch die Tumorinitiation und/oder die Plastizität von Gliomzellen reguliert.

In meiner Doktorarbeit habe ich untersucht, ob der Verlust von MYT1L die Tumorentstehung in postmitotischen Neuronen induzieren kann und ob MYT1L die GBM-Identität reguliert.

Im Gegensatz zum etablierten wissenschaftlichen Verständnis konnte ich zeigen, dass die Tumorsuppressor-Mutation PTEN und TP53 die Tumorentstehung in differenzierten Neuronen verursachen können. Der Verlust von MYT1L in postmitotischen Neuronen führte, zusammen mit Tumorsuppressor-Mutationen, zu einer erhöhten Letalität und einem plötzlichen Tod von Mäusen. Zusammen deutet dies darauf hin, dass der Verlust von Tumorsuppressoren zu einer Destabilisierung der Zellidentität führen kann und zur Folge hat, dass postmitotische Neuronen zur Tumorentstehung beitragen können. Noch bemerkenswerter ist, dass der zusätzliche Verlust von MYT1L diese Prozesse scheinbar verstärken kann. Der Verlust von MYT1L in postmitotischen Neuronen beeinträchtigte außerdem die Expression neuronaler Gene.

In einem humanen Organoid-Modell untersuchte ich die Auswirkungen von MYT1L auf die Gehirntumorentstehung. In diesem Modell verursachte der Verlust von MYT1L in Kombination mit der Mutation bekannter GBM-Tumorsuppressoren eine erhöhte Zellproliferation. Diese Experimente stützen die Hypothese, dass MYT1L ein Gehirntumorsuppressor ist. Darüber hinaus konnte ich zeigen, dass MYT1L-Überexpression in Gliomzelllinien aus Patienten eine signifikante Reduktion der Invasion als auch der Proliferation hervorrief. Aktivator/Repressor-Fusionsexperimente zeigten, dass MYT1L vorwiegend als transkriptioneller Repressor fungiert, um Proliferation und Invasion zu hemmen. Um zu untersuchen, welche molekularen Auswirkungen MYT1L auf die Identität von Gliomzellen hat, habe ich die Genexpression in Abhängigkeit von MYT1L genauer analysiert. Interessanterweise konnte ich zeigen, dass MYT1L die Identität der Zellen von einem mesenchymal-ähnlichen Zustand zu einem neuralen Vorläuferzellen-ähnlichen, kurz NPC-ähnlichen, GBM-Subtypen trans-differenzierte. Dieser Subtyp geht mit einer besseren Prognose für Patienten einher.

Meine Arbeit weist auf einen neuartigen Mechanismus hin, bei dem MYT1L die Plastizität von Zellen verhindert, um Dedifferenzierung von postmitotischen Zellen und Tumorentstehung zu vermeiden.

Weiterhin wird MYT1L als potenzieller und repressiver Regulator von NPC-ähnlichen Zellzuständen beim Glioblastom vorgestellt. Diese Ergebnisse könnten zu einer Subtyp-spezifischen Behandlungen führen und somit die Therapiemöglichkeiten für Glioma-Patienten verbessern.

TABLE OF CONTENTS

LIST OF FIGURES

SUPPLEMENT

LIST OF TABLES

LIST OF ABBREVIATIONS

AAV	Adeno-associated virus
AAP	Antarctic Phosphatase
AC-like	Astrocyte-like
BF	Bright field
bp	Base pairs
CNS	Central nervous system
CL	Classical
CRISPR	CRISPR-associated protein-9 nuclease
CT	Cycle of threshold
DEG	Differentially expressed gene
DBD	DNA-binding domain
DNA	Deoxyribonucleic acid
Dox	Doxycycline
EB	Embryoid body
EGFR	Epidermal growth factor receptor
EMT	Epithelial-to-mesenchymal
FACS	Fluorescence Activated Cell Sorting
GJA	Gap junction alpha-1 protein
GEPIA	Gene Expression Profiling Interactive Analysis
GFAP	Glial fibrillary acidic protein
GEMM	Genetically engineered mouse model
GTEx	Genotype-Tissue Expression
GBM	Glioblastoma multiforme
GFP	Green fluorescent protein
GO	Gene Ontology
GSC	Glioma stem/stem-like cell
hESC	Human embryonic stem cell
IBA1	Ionized calcium-binding adapter molecule 1
IDH	Isocitrate dehydrogenase
IF	Immunofluorescence
iN	Induced neuron
IPA	Ingenuity Pathway Analysis
iPSC	Induced pluripotent stem cell
KD	Knockdown

MEF	Mouse embryonic fibroblasts
MES	Mesenchymal
MYT1L	Myelin transcription factor 1-Like
N	Neural
NGN2	Neurogenin 2
NF1	Neurofibromin 1
NPC	Neural progenitor cell
NSC	Neural stem cell
MGMT	O-6-Methylguanine DNA methyltransferase
mNG	mNeonGreen
MRI	Magnetic resonance imaging
OPC	Oligodendrocyte progenitor cell
PBS	Phosphate buffered saline
PCR	Polymerase chain reaction
PDGC	Patient-derived glioma cell
PDX	Patient-derived xenograft
PFA	Paraformaldehyde
PMT	Proneural-to-mesenchymal transition
PN	Proneural
PI(3)K	Phosphatidylinositol-3-OH kinase
PTEN	Phosphatase and tensin homolig
ROI	Region of interest
RPM	Rounds per minute
RT	Room temperature
RTK	Receptor tyrosine kinase
RTqPCR	Real time quantitative polymerase chain reaction
shRNA	Short hairpin RNA
scRNA-Seq	single cell RNA sequencing
SD	Standard deviation
SEM	Standard error of mean
STAT3	Signal transducer and activator of transcription 3
SIN3D	Sin3-interaction domain
SVZ	Subventricular zone
Syn	Synapsin
Tam	Tamoxifen

TCGA	The Cancer Genome Atlas
TF	Transcription factor
tdTom	tdTomato
TIDE	Tracking of Indels by decomposition
TM	Tumor microtube
TMZ	Temozolomide
TP53	Tumor protein p53
TTF	Tumor-Treating Fields
VEGF	Vascular endothelial growth factor
WT	Wildtype
YAP1	Yes-associated protein 1
ZEB1	Zinc finger E-box-binding homeobox 1
ZF	Zinc finger

1 INTRODUCTION

1. INTRODUCTION

1.1 Hallmarks of cancer

Cancer is a disease with tremendous complexity, at all levels – based on genetics, histology, pathology, prognosis, and therapy. The hallmarks of cancer present a logical framework for the different characteristics of cancer pathogenesis and disease progression. This framework rationalizes the complexity and incredible diversity of neoplastic diseases (Hanahan and Weinberg 2000). Eight hallmarks were originally proposed to form the core organizing principles of cancer, comprising the acquired capabilities for *sustaining proliferative signaling, evading growth suppressors, resisting cell death, enabling replicative immortality, inducing/accessing vasculature, activating invasion and metastasis, reprogramming cellular metabolism,* and *avoiding immune destruction*. Later, two "enabling characteristics", namely *tumor-promoting inflammation* and *gene instability and mutation*, were added to the framework (Hanahan and Weinberg 2011). They do not necessarily cause cancer but assist cells in turning from normal to oncogenic. Recently, four additional emerging hallmarks were suggested to complement the existing framework. These new hallmarks are termed *unlocking phenotypic plasticity*, *non-mutational epigenetic reprogramming*, *polymorphic microbiomes,* and *senescent cells* (Hanahan 2022). Together, these hallmarks and their current refinements provide a basic foundation for understanding cancer initiation, progression, and resistance to therapy, and have served to identify specific tumor cell functions that have become therapeutic targets.

1.1.2 Unlocking phenotypic plasticity – a new emerging cancer hallmark

Phenotypic plasticity is defined as the capability of cells to change their phenotypes without genetic mutations in response to environmental cues (Shen and Clairambault 2020). The plasticity of cells is of great relevance in many fields, most notably for normal development, stem cell biology as well as cancer biology (Mills et al. 2019). Regarding the development of multicellular organisms, changes in cellular identity represent an intrinsic feature. Here, cells differentiate from progenitors to progeny and acquire increasingly specialized features. In major tissue types, such as the brain and heart, progenitor cells give rise to post-mitotic, terminally differentiated cell types during development (Zglinicki et al. 2021). These post-mitotic cells are thought to maintain their differentiated features in adult tissues under stable, homeostatic conditions. However, in most tissues, a small number of so-called adult stem cells still exist and are still able to differentiate into a limited number of cell types. Because of their long life, tissue stem cells have an enhanced potential to accumulate oncogenic hits that can enable tumor formation, and they are the

suspected cells of origin for many cancers (Visvader 2011). For brain cancer this idea was supported by studies led by Alcantara Laguna et al., who induced tumorigenic mutations in the tumor suppressors *Nf1*, *Tp53* and *Pten* in neural stem and progenitor cells, which subsequently gave rise to glioblastoma. (Alcantara Llaguno et al. 2019; Alcantara Llaguno et al. 2009; Alcantara Llaguno and Parada 2016; Alcantara Llaguno et al. 2019). This well-accepted concept, that only stem cells or progenitor cells are the origin of brain cancer was however challenged in the past decade by Fiedmann-Morvinski and colleagues. They proposed, that also fully differentiated neurons and astrocytes retain the potential to change their fate, re-enter the cell cycle, and can contribute to brain cancer formation (Friedmann-Morvinski et al. 2012). These findings, while still lacking appropriate genetic drivers, directly link dedifferentiation of mature cell states to tumor formation and support the idea that phenotypic plasticity presents a critical component of cancer pathogenesis (Yuan et al. 2019).

The controversial hypothesis, that even post-mitotic differentiated cells, given the required signals or mutations, could initiate cancer formation, gained momentum by the recently introduced and new emerging cancer hallmark unlocking phenotypic plasticity (Fig. 1A) (Hanahan 2022).

This new hallmark proposes that mutation or deregulation of transcriptional regulators causes cancer formation. In this framework, either dedifferentiation, blocked differentiation, or trans-differentiation can contribute to neoplasia (Fig. 1B). These different mechanisms can be explained as follows:

Dedifferentiation denotes the loss of lineage commitment in differentiated cells and reacquisition of stem cell features. This is exemplified by the loss of SMAD4, a differentiation-enforcing transcription factor (TF) that causes oncogenesis in the differentiated gut epithelium (Perekatt et al. 2018).

Blocked differentiation manifests in progenitor cells that are blocked from advancing into a non-proliferative differentiated state. This can, for example, be observed in melanoma. Here, the developmental transcription factor SOX10 is normally downregulated during melanocyte differentiation. When expression of SOX10 is maintained, differentiation of neural progenitor cells into melanocytes is blocked and BRAF-driven melanomas can form (Kaufman et al. 2016).

Transdifferentiation describes a direct fate switch to another differentiated cell type. One example is the epithelial-to-mesenchymal (EMT) transition (Lee et al. 2021). During EMT, cells become more mesenchymal-like, lose apicobasal polarity, and gain motility, resulting in an invasive growth capability of cancer cells (Gupta et al. 2019).

Hence, understanding the principles of phenotypic plasticity can offer the opportunity to take cancer research to a new level. Each of these mechanisms are governed by TFs, which regulate cell

fate by gene expression and/or repression of unwanted genes (Hanahan 2022). Subsequently, mutations or deregulation of those master regulators can unlock plasticity. Several TFs and their deregulation have been associated with cancer formation. Almost all these TFs have been characterized as transcriptional activators (Perekatt et al. 2018; Drápela et al. 2020; Ganguly et al. 2013). In addition to gene activators, TFs can also function as repressors (Berest et al. 2019). However, the role of transcriptional repressors that prevent unwanted plasticity by silencing of unwanted genes is likely equally important. This is exemplified by the recent discovery of the neuron-specific repressor Myelin Transcription Factor 1-Like (MYT1L) which blocks several pathways that counteract neurogenesis (e.g., WNT and NOTCH) and promotes proliferation (e.g. YAP and TEAD) to induce and maintain neuronal cell fate (Mall et al. 2017). These functions suggest that loss or mutation of MYT1L could lead to dedifferentiation and promote brain tumor formation. Indeed, MYT1L mutations have been reported in brain cancer patients, and a tumor suppressor role was previously suggested in murine, as well as in human cells (Melhuish et al. 2018; Hu et al. 2013, 2013; Melhuish et al. 2018). However, the responsible underlying gene regulatory programs and molecular mechanisms remain poorly understood.

I propose that mutation or loss of MYT1L could cause dedifferentiation, blocked differentiation, and phenotypic plasticity, and play essential roles in brain tumors. This raises the following question that I want to address in my doctoral work: Can mature neurons indeed serve as the origin of brain cancer formation upon loss of MYT1L?

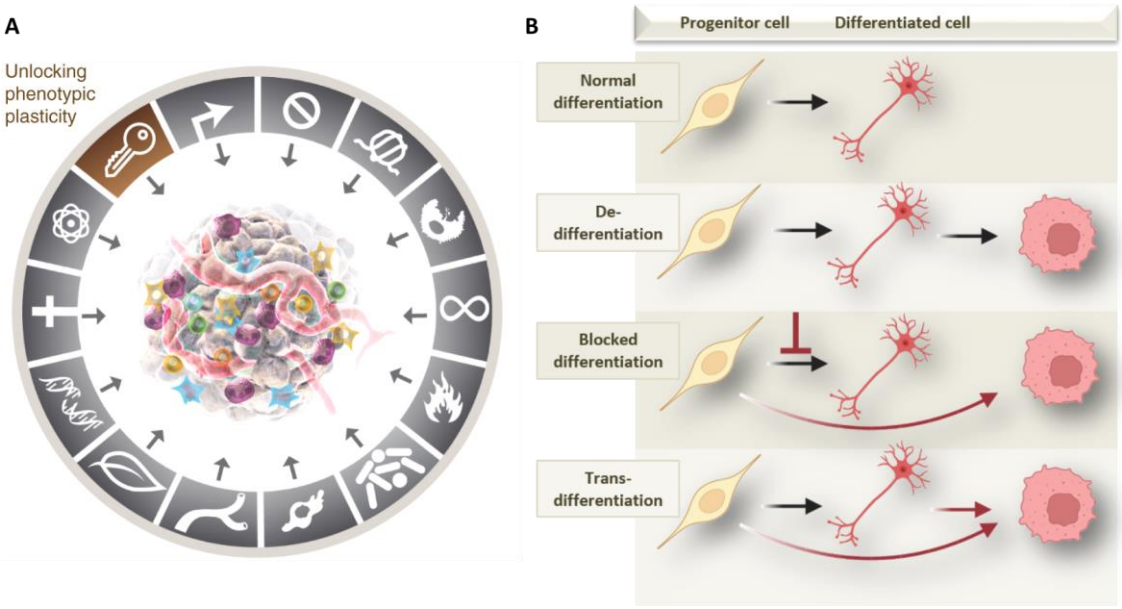

Figure 1: Phenotypic plasticity as new cancer hallmark
(A) Phenotypic plasticity represents one of the newly emerging cancer hallmarks. (B) Phenotypic plasticity redirectsnormal cellular differentiation, e.g. by including dedifferentiation from mature to progenitor states, blocked differentiation from progenitor cell states, and transdifferentiation into different cell lineages to contribute to cancer pathogenesis. Illustration adapted from Hanahan et al. (2022).

1.2 Brain tumors

In 2021, over 80.000 individuals were diagnosed with brain tumors and other central nervous system (CNS) tumors in the United States. It is estimated that almost 20.000 people succumb to the disease annually (Miller et al. 2021). Tumors of the brain and CNS are categorized as primary or secondary brain tumors. Primary brain tumors arise from tissues of the CNS, whereas secondary brain tumors are defined as metastatic tumors that originate from a primary tumor outside the CNS (Behin et al. 2003). With more than 130 different subtypes, primary brain tumors comprise a large variety that differ in many phenotypic, molecular, and genotypic parameters (Louis et al. 2016). Diffuse gliomas are the largest primary brain tumor group and are sub-classified into oligodendrogliomas (IDH mutation in combination with 1p/19q co-deletion) and astrocytomas (IDH wild-type or mutant) (Louis et al. 2016). Furthermore, gliomas are subdivided into grade *I*–*IV* according to the WHO grading system (Louis et al. 2007). Gliomas categorized by grade *I* have the most favorable prognosis, whereas grade *IV* gliomas, like glioblastomas, are associated with the poorest survival (Visser et al. 2015).

Gliomas are characterized by a strong heterogeneity regarding pathology, genetic signature, and response to treatment. Nevertheless, they share some common aberrations in various molecular pathways. Large-scale genetic analysis revealed the common aberrations: (i) Dysregulation of

growth factor signaling via amplification or mutational activation of receptor tyrosine kinase (RTK) genes; (ii) activation or loss of suppression of the phosphatidylinositol-3-OH kinase (PI(3)K) pathway; (iii) frequent disruption of tumor suppressor pathways like the p53 pathway (Cancer Genome Atlas Research 2008). Furthermore, in comprehensive genetic studies, Parsons and colleagues identified the mutation of the isocitrate dehydrogenase (IDH) gene 1 and 2 as major genetic characteristics shared by glioma patients (Parsons et al. 2008). Thus, IDH mutations can serve as a marker and potential therapeutic target in brain tumor patients.

Current clinical research benefits from great advances in single cell sequencing and spatial transcriptomics, which provide an even more dynamic classification as these methods reveal molecular identity and cellular state. This has been intensely evaluated, especially in the case of glioblastoma multiforme.

1.1.2 Glioblastoma multiforme – the most malignant primary brain tumor

Glioblastoma multiforme (GBM) is a highly aggressive and infiltrative tumor of the central nervous system and is therefore categorized as the most malignant glioma subtype (grade *IV*). Furthermore, it represents the most frequent malignant primary brain tumor, with an incidence rate of 6 per 100,000 individuals globally (Visser et al. 2015; Weller et al. 2017). GBM is one of the deadliest cancers and has median survival estimates that range from 8 months (Miller et al. 2021) to 12-14 months (Stupp et al. 2005). The current standard-of-care treatment only slightly improves patient survival through maximal safe surgical resection, radiotherapy, and temozolomide (TMZ) chemotherapy. More recently, Tumor-Treating Fields (TTF) are used as an adjuvant with TMZ and showed a significant improvement in overall survival and progression-free survival for patients with newly diagnosed GBM (Stupp et al. 2017). Nonetheless, tumor recurrence remains unpreventable and long-term survival is rare, with only 6.8% of patients surviving past 5 years (Wen et al. 2020). Complete tumor resection is challenging due to the deep infiltration of neoplastic cells into the surrounding tissue, often leaving a small population of cells that can acquire resistance to therapies.

On a histological level, GBM manifests with a high mitotic index, hypervascularization, necrotic areas and fencelike hypercellular arrangements of tumor cells that migrate from necrotic locations, also known as palisades (Brat et al. 2004; Aldape et al. 2015). Primary GBM, which accounts for 90% of all GBM, is characterized by IDH wildtype status (Han et al. 2020). Despite the high degree of heterogeneity in GBM, there are common aberrations in numerous molecular pathways and genetic mutations shared between GBM patients. These include oncogenic events such as amplification of the EGFR gene (40%), and activation or loss of suppression of the PI3K-AKT (50%) and/or RAS-MAPK signaling pathways (Parsons et al. 2008). Additionally, disruptions in tumor

suppressor pathways such as NF1- (15%), PTEN- (30%), p53- (64%), and Rb-pathways (68%) are characteristic of GBM (Parsons et al. 2008; Jung et al. 2017). One of the most clinically relevant prognostic and predictive markers for GBM patients is the promoter methylation of the O-6-methylguanine-DNA methyltransferase (MGMT) (Stupp et al. 2009). MGMT is a nuclear protein involved in DNA repair. It removes alkyl groups from O6-position of guanine, preventing base damage, and protects not only normal cells, but also tumor cells from apoptosis (Belanich et al. 1996). Glioma cells with a methylated MGMT promoter show decreased levels of MGMT protein, which impedes DNA repair and results in the accumulation of DNA damage. This plays an important role in GBM therapy, where TMZ is applied to introduce DNA damage and thus cell death. Hence, TMZ therapy is generally more effective in GBM patients with decreased levels of MGMT and hypermethylation of the MGMT promoter (Hegi et al. 2005).

Taken together, this demonstrates that there are multiple approaches to characterize GBM. Besides these classifications there is enormous heterogeneity and plasticity, which represents the major challenge in GBM research.

1.2.1 Heterogeneity and phenotypic plasticity in GBM

The major reason for the varying therapeutic responses and distinct outcomes of GBM patients is the high degree of intra-tumoral heterogeneity in GBM. During tumor progression, neoplastic cells from the same tumor in distinct locations in the brain will acquire different additional mutations or exhibit specific phenotypic or epigenetic states (Eder and Kalman 2014). Given this plasticity, radio- and chemotherapy may only be effective against certain subpopulations of cells within the tumor (Wick and Kessler 2018). Hence, understanding the intra-tumoral heterogeneity and identity of the tumor is essential to develop an accurate treatment strategy and improving the therapeutic outcome. For this purpose, classification methods based on key molecular events and genetic alterations were introduced.

In 2010, a well-accepted study divided GBM into four subtypes based on bulk tumor sequencing data from the Cancer Genome Atlas (TCGA): classical (CL), mesenchymal (MES), neural (N), and proneural (PN) (Verhaak et al. 2010). Further revisions excluded the neural subtype, which likely arose due to the inclusion of non-tumor cells in the analyses (Wang et al. 2017; Sidaway 2017). Recent single cell analyses and lineage tracing experiments have revealed four major cellular states of malignant GBM: neural progenitor-like (NPC1/2-like), oligodendrocyte-progenitor-like (OPC-like), astrocyte-like (AC-like), and mesenchymal-like (MES1/2-like) (Neftel et al. 2019). In this study, most tumors contained all four cellular states, and all tumors contained at least two. Both the Verhaak and Neftel classification converge to some extent. The proneural tumors tend to comprise

NPC-like and OPC-like cells, mesenchymal tumors are predominantly MES-like cells, and classical tumors consist of mostly AC-like and MES-like cells (Neftel et al. 2019). The plasticity among these cell states in GBM tumors has emerged as an important factor that may underlie the process of transdifferentiation and subtype switching, including epithelial-to-mesenchymal (EMT) and proneural-to-mesenchymal transitions (PMT) (Kim et al. 2021).

Subtype identification can play an important role in clinical predictions. For example, proneural GBM was found to respond better to bevacizumab, a monoclonal antibody targeting vascular endothelial growth factor (VEGF), than other subtypes of GBM (Sandmann et al. 2015). Another study showed that in the classical subtype of GBM, promoter methylation status of O6-methylguanine DNA methyltransferase (MGMT) is a predictive biomarker, but not for other subtypes (Brennan et al. 2013). Furthermore, mesenchymal transformation has been associated with high therapy resistance to both bevacizumab (Piao et al. 2013) and TMZ (Guo et al. 2020). Some studies also associated the proneural subtype with the most favorable outcome and the mesenchymal subtype with the poorest survival (Phillips et al. 2006; Huse et al. 2011; Zheng et al. 2012). However, these findings were skewed by the less-aggressive IDH mutant GBM previously defined as part of the proneural subgroup (Wang et al. 2017). More recently, it was shown that there is a link between subtype identity and tumor cell connectivity (Venkataramani et al. 2022). AC and MES-like GBM cells showed the highest connectivity signature scores in single cell RNA sequencing (scRNA-Seq) data of patient-derived xenografts and patient samples, where higher connectivity appeared to correlate with poorer survival. Accordingly, NPC and OPC-like represented the subtypes with lower connectivity and thus better survival.

Therefore, understanding the underlying mechanisms driving GBM subtype identity and phenotypic plasticity is of huge medical interest, as it could facilitate the identification of optimal therapeutic strategies in a personalized fashion and improve patient prognosis. However, the underlying regulatory circuitry that gives rise to different subtypes and cell states and that drives the plasticity between those states remains unclear (Liu et al. 2020). Identifying the transcription factors responsible for shaping distinct GBM transcriptional subtypes could provide a mechanistic insight into the cause of this heterogeneity and, more importantly, enable the design of targeted therapies.

1.3 The Transcription Factor MYT1L

1.3.1 MYT1L and its role in GBM

Transcription factors (TFs) are proteins that bind DNA to regulate gene expression. They shape a wide range of cellular processes, such as proliferation, differentiation, apoptosis, immune responses, and metabolism. Given their overarching role in determining cell fate, dysregulation or malfunction of TFs can contribute to cancer by affecting tumor initiation, progression, invasion, metastasis, and chemo-resistance of cancer (Vishnoi et al. 2020). Dysregulated or mutated TFs are also involved in many aspects of GBM and can have both oncogenic and tumor-suppressive effects (Papavassiliou and Papavassiliou 2022).

For example, the TFs such as signal transducer and activator of transcription 3 (STAT3) or mesenchyme homeobox 2 (MEOX2) exhibit oncogenic effects by promoting GBM cell proliferation (Gu et al. 2008; Schönrock et al. 2022). Glioma-associated oncogene homolog 1 (GLI1) is another oncogenic TF and is correlated with glioma stem cells (GSC) self-renewal, GBM cell migration, invasion, and metastasis (Clement et al. 2007; Lo et al. 2009). On the other hand, tumor-suppressing TFs in GBM include tumor protein Tp53 (Tp53), neurofibromin 1 (NF1), and phosphatase and tensin homolog (PTEN) (Parsons et al. 2008).

Besides these well-characterized tumor suppressors, TFs involved in early and key developmental stages often have strong cancer associations (Whyte et al. 2013). The proposed TF MYT1L could represent one such candidate fulfilling both criteria. MYT1L is directly involved in neuronal differentiation with an important role in establishing and maintaining neuronal cell fate (Mall et al. 2017; Vierbuchen et al. 2010). Moreover, several studies have found a correlation between MYT1L levels and cancer formation. These studies revealed decreased MYT1L levels in over 80% of GBM tissue samples (Hu et al. 2013). They also found that shRNA-mediated knockdown of MYT1L in *Tp53*$^{-/-}$*Pten*$^{+/-}$ mouse neural stem cells induced orthotopic tumor formation in mice whereas the control group remained tumor-free (Hu et al. 2013). On the other hand, enforced MYT1L expression inhibited tumor formation, which suggests MYT1L as a potential tumor suppressor (Fig. 2B). In addition, MYT1L expression reduced proliferation in different human GBM cell lines (Melhuish et al. 2018). Furthermore, gene expression analysis of TCGA data revealed that MYT1L-expressing cells show decreased expression of genes associated with proliferation (Melhuish et al. 2018) (Fig. 2C).

Given the impact of MYT1L expression in the mouse model, and the correlation between MYT1L expression and patient survival, the question arises about the underlying molecular mechanisms. Utilizing MYT1L for neuronal reprogramming, it has been shown that MYT1L downregulates several pathways that counteract neurogenesis and proliferation (e.g., WNT and NOTCH), including genes

such as hairy enhancer of split 1 (HES1), a member of the Notch signaling pathway, signal transducer and activator of transcription (Stat3), yes-associated protein 1 (YAP1), and Wnt family member 5A (Wnt5a) (Mall et al. 2017) (Fig. 2A). These genes do not only play an important role in neuronal development, but also promote tumor cell proliferation in gliomas (Shafi and Siddiqui 2022). Given the broad range of genes that are repressed by MYT1L, it appears evident that MYT1L could also acts as a tumor suppressor in the context of GBM.

In fact, MYT1L overexpression in two different patient-derived GBM cell lines revealed that gene programs related to neuronal differentiation were activated, while programs related to EMT and proliferation were downregulated (Melhuish et al. 2018). This study also introduced a direct mechanistic link between MYT1L and the transcription cofactor YAP1 and suggested that MYT1L directly represses YAP1. As an effector in the Hippo pathway, YAP1 acts as a major regulator of organ size, proliferation, and apoptosis (Huang et al. 2005). YAP1 plays an important role in GBM pathogenesis by increasing proliferation and invasion of tumor cells and tumor drug resistance (Overholtzer et al. 2006; Meng et al. 2016). Interestingly, YAP1 interacts directly with the members of the TEAD transcription factor family to promote gene programs that lead to proliferation and cell survival and EMT of GBM cells (Lu et al. 2017). Based on these findings, MYT1L represents a promising potential target to interfere with the tumor-promoting function of YAP1 and its interaction with the TEAD family.

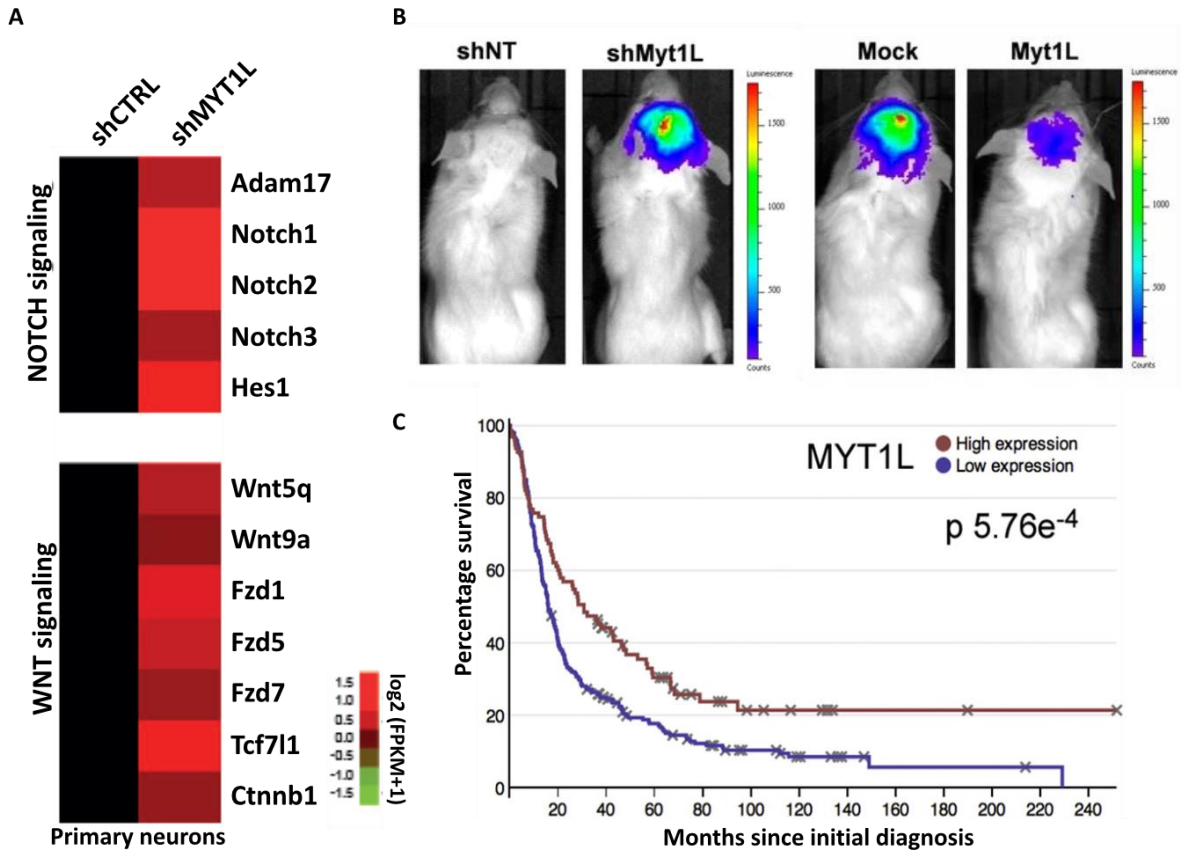

Figure 2: The potential role of MYT1L as tumor suppressor and GBM subtype marker
(A) RNA-seq expression values of selected MYT1L targets from primary neurons upon MYT1L knockdown. Tumor promoting pathways, such as Wnt and Notch-pathway, are upregulated. (FPKM, fragments per kilobase of transcript per million mapped reads) (Mall et al. 2017) (B) Representative images of intracranial tumor formation of *p53*$^{-/-}$*Pten*$^{+/-}$ NSCs with sh*Myt1l* or control and representative images of intracranial tumor formation of *p53*$^{-/-}$*Pten*$^{-/-}$ GSCs with MYT1L overexpression or control (mock). From Hu et al. (2013). (C) Patient survival of low and high MYT1L expression cohorts, from Melhuish et al. (2018).

Taken together, high MYT1L correlated with better GBM patient prognosis and MYT1L target gen regulation can be linked to relevant processes of GBM, such as proliferation and invasion. However, whether MYT1L indeed functions as a tumor suppressor, *in vitro* and *in vivo*, as well as the identification of the exact tumor-suppressive functions of MYT1L remain unclear. My work therefore includes studies in patient-derived glioma cell lines to investigate the effect of the proposed function of MYT1L.

1.3.2 Correlation of MYT1L and GBM subtype identity

While TFs have been shown to play a key roles in GBM, driving tumor initiation, progression, invasion, metastasis, and resistance to treatment (Papavassiliou and Papavassiliou 2022), they are also emerging as relevant markers or potential drivers of GBM subtype identities that may represent targets for therapeutic intervention in GBM (Xu et al. 2021). Indeed, several TFs have

been described to be specifically expressed in distinct GBM subtypes. For example, FOSL1 was identified as a key regulator of the mesenchymal (MES) subtype (Marques et al. 2021). Another TF, RP58, has a similar function to MYT1L in repressing alternate identities in neurons, and was found to have significantly higher expression in the proneural (PN) GBM subtype compared to other subtypes, such as the MES subtype (Xiang Chaomei et al. 2021). Based on this, and since MYT1L was found to downregulate gene programs related to EMT, I propose that MYT1L is also associated with maintenance or even induction of a specific subtype. Indeed, analyzing single cell RNA sequencing data sets revealed that MYT1L expression was strongly and almost exclusively associated with NPC2-like cells (Neftel et al. 2019). Most primary GBMs originate from proneural-like tumors and then switch to a MES-like state (Fedele et al. 2019). While proneural GBM is associated with a relatively better overall survival compared to other subtypes, mesenchymal GBM accounts to the most aggressive type (Ozawa et al. 2014). Hence, transformation into mesenchymal-like cells is one factor underlying the acquisition of radio- and chemotherapy resistance (Huang et al. 2020; Bhat et al. 2013). Therefore, MYT1L may have prognostic value and may also guide treatment choice. Whether MYT1L indeed functions as a potential regulator of the proneural/NPC2-like subtype, or even regulates transdifferentiation processes, remains to be further investigated and represents a major goal of my doctoral work. Understanding transcriptional changes and underlying cell state transitions in GBM represents a major current focus in glioma research.

1.3.3 The molecular role of MYT1L

From a physiological perspective, MYT1L is a highly conserved neuronal transcription factor that regulates neuronal differentiation in vertebrate nervous system development (Kameyama et al. 2011). MYT1L is unique in its almost exclusive expression in virtually all neurons that is maintained throughout life (Matsushita et al. 2014; Cardoso-Moreira et al. 2019) (Fig. 3A,B). In line with these features, MYT1L plays an important role in enhancing neuronal identity *in vitro* (Mall et al. 2017; Vierbuchen et al. 2010). MYT1L belongs to the family of noncanonical Cys-Cys-His-Cys zinc-finger (ZF) proteins with a total of six ZF domains. The two central ZF domains have been evaluated extensively regarding their DNA-binding function to 5'-AAGTT-3' motifs (Besold et al. 2013).

In vitro, it has been shown that MYT1L supports reprogramming of mouse embryonic fibroblasts (MEFs) into induced neurons (iNs) when overexpressed together with proneural TFs (Vierbuchen et al. 2010). Subsequently, researchers focused on studying whether MYT1L promotes neuronal differentiation and maturation (Chen et al. 2021; Chen et al. 2022), and whether MYT1L exerts its function by transcriptional activation or repressor in neuronal tissue (Manukyan et al. 2018; Kepa

et al. 2017). In 2017, these questions were intensively addressed by Mall et al., who showed that MYT1L specifically represses non-neuronal genes by binding the 5'-AAGTT-3' core motif within target gene promoters. This motif is enriched in non-neuronal genes and is less abundant in promoters of neuronal genes. In the same study, MYT1L was further shown to interact with SIN3B, which in turn recruits the repressive histone deacetylase 1 (HDAC1) (Mall et al. 2017). Histone deacetylases modulate open chromatin structures towards compaction (D'Mello 2019), preventing access by the transcriptional machinery and resulting in transcriptional repression (Berger 2002). These interaction partners might explain how the repressive function of MYT1L is mediated. Among the target genes of MYT1L are multiple members of the NOTCH and WNT signaling pathway (Mall et al. 2017) which act as negative regulators of neurogenesis. Upon DNA-binding and clustering with the SIN3B complex, Notch-signaling mediators such as HES1 are directly repressed, resulting in neuronal differentiation and elevated neuronal gene expression (Mall et al. 2017).

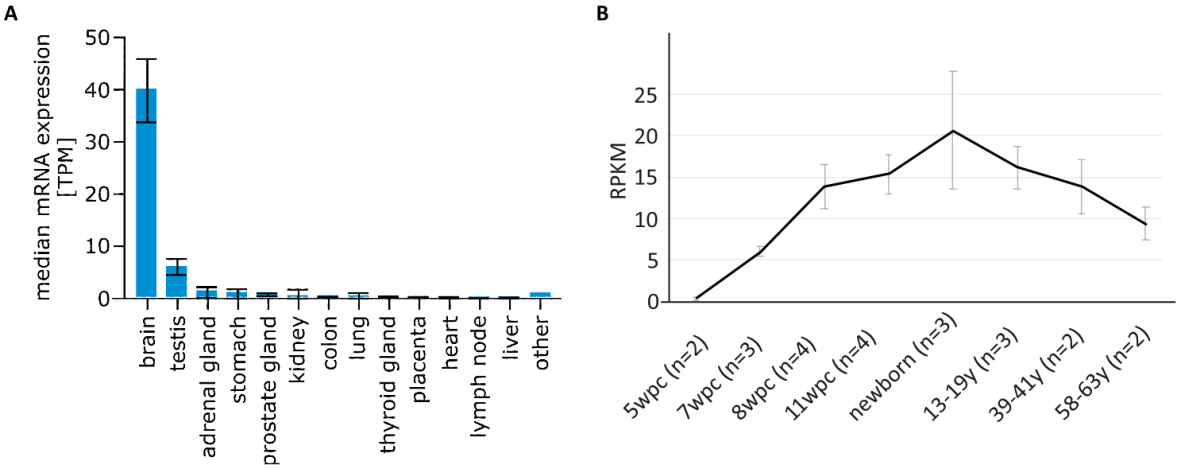

Figure 3: MYT1L in the human brain

(A) MYT1L is almost exclusively expressed in the brain. TPM = transcripts per million. Adopted from ProteomicsDB (https://www.proteomicsdb.org/). (B) MYT1L expression in the human brain peaks in new-born age but is still expressed in adulthood (data from). RPKM= Reads per kilo base per million mapped reads; wpc= weeks post conception; y = years. (Cardoso-Moreira et al. 2019)

Given its important role in neuronal differentiation throughout life, it is noticeable that loss or mutation of MYT1L triggers severe and disease related phenotypes. Most reported genetic alterations in MYT1L are linked to neurodevelopmental disorders, such as schizophrenia, autism spectrum disorder (ASD) and intellectual disability (Mansfield et al. 2020). MYT1L mutant mice exhibit neurodevelopmental delays with thinner cortices, behavioral phenotypes, and gene expression changes that are associated with ASD (Chen et al. 2021; Kim et al. 2022; Wöhr et al. 2022).

While MYT1L loss induced dysregulation of developmental pathways and in turn neurodevelopmental disorders, it is conceivable that the deregulation of such pathways, together with other tumorigenic events, also plays a key role in brain cancer initiation and progression.

1.4 GBM model systems

To study novel key players in GBM such as MYT1L, we depend on cutting-edge models that mimic the disease of patients. Over the past decades, a variety of *in vitro* and *in vivo* GBM models were established in for brain cancer research.

Classical approaches to study GBM include *in vitro* glioma cell culture, and *in vivo* models such as xenograft or genetically engineered mouse models (GEMMs) (Gómez-Oliva et al. 2021). *In vitro* modeling using GBM cell lines and patient-derived cells offer a simple and fast system, with minor ethical concerns and high reproducibility, but they do not allow to study complex tumor microenvironment interactions. GEMMs are based on inactivation of one or several tumor suppressors or overexpression of oncogenes (Miyai et al. 2017). They are suitable models to study many aspects of glioma biology because normal brain and tumor architectures and histological characteristics are maintained. However, the genetics and histology of the modified tumor models are often not representative of the original human tumor. Hence, xenograft and GEMM models come with major limitations.

In contrast, novel technologies in GBM research focus on reproducing realistic cellular environment surrounding the brain tumor cells while using human cells (Gómez-Oliva et al. 2021). Promising approaches include human induced pluripotent stem cells (iPSCs) and embryonic stem (ES) cells, which can be used to generate human cerebral organoid cultures. By mimicking key features of brain development, human cerebral organoids have been found to model aspects of human brain histology and physiology with a certain accuracy (Lancaster et al. 2013). Moreover, cerebral organoids offer great potential to model brain tumorigenesis by introducing oncogenic mutations found in brain cancer (Bian et al. 2018; Ogawa et al. 2018).

1.5 Aim of the study

Previous work revealed that the neuron-specific transcriptional repressor MYT1L plays an integral role in blocking pathways which counteract neurogenesis and promote proliferation in order to induce and maintain neuronal identity. While an important role for MYT1L in neurodevelopmental disorders has been described, the function of MYT1L in cancer including malignant gliomas is still unclear.

Recently the concept that dysregulated transcription factor expression can cause dedifferentiation of mature cell states, thus enabling tumor initiation, was introduced. This raises the central question of my doctoral study: Can loss of MYT1L destabilize cell fate and indeed cause tumor formation by dedifferentiation in post-mitotic neurons? To that end, I present genetic models for neuron specific targeting of MYT1L and additional GBM tumor suppressors.

The proneural/NPC2-like subtype specific expression of MYT1L motivates my second question: Can MYT1L regulate transdifferentiation processes and function as a regulator of GBM subtype identity?

Overall, the aim of my thesis was to investigate whether loss of MYT1L unlocks phenotypic plasticity resulting in brain tumor initiation, progression, and identity shifts. I investigated whether loss of MYT1L enables dedifferentiation resulting in destabilization of neuronal cell fate and promoting tumor formation (Fig. 4A), whether MYT1L has a potential tumor-suppressive role (Fig. 4B), and finally whether MYT1L is a GBM subtype marker and may be involved in regulating subtype transitions (Fig 4C). My work presents role of MYT1L in tumor formation, progression and plasticity and shows that MYT1L could be instrumental in helping to develop novel and more effective targeted GBM therapies.

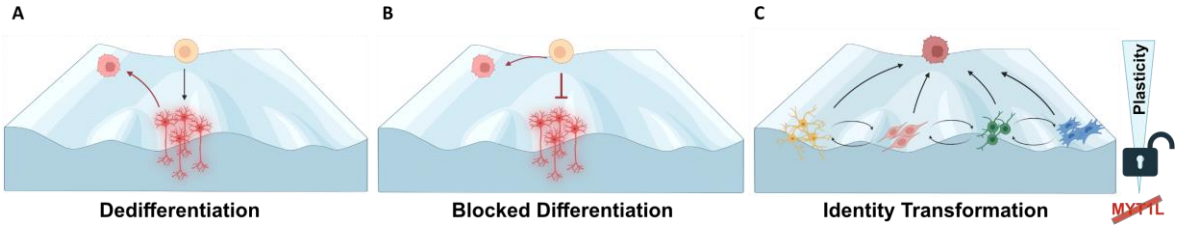

Figure 4: Aim of the study

This study investigated whether loss of MYT1L could unlock phenotypic plasticity and drive tumor formation, progression, and tumor identity changes. The three mechanisms that could result phenotypic plasticity are described as *dedifferentiation*, *blocked differentiation* and *transdifferentiation,* the latter being denoted here as *identity transformation*. In (A), I examined whether loss of MYT1L could result in loss of lineage commitment of fully differentiated neurons, reacquisition of stem cell features, and potentially initiate tumor formation. In (B), I investigated whether loss of MYT1L could block differentiation and, on the other hand, whether overexpression of MYT1L could have a tumor-suppressive role. In (C), I studied MYT1L as a potential GBM subtype marker and addressed the question whether it may be a transcriptional master regulator regulating GBM subtype transitions.

2 MATERIALS

2. MATERIAL

2.1 Cell Culture

Table 1: Cell Lines

Cell type	Source
Human embryonic stem cells H1	Human embryonic stem cells H1
Human induced pluripotent stem cells C6	NIMH (Bethesda, USA)
HEK-293T cells	ATCC (Manassas, USA)
P3XX patient-derived glioma cells	Winkler lab (DKFZ Heidelberg)
S24tdTomato patient-derived glioma cells	Winkler lab (DKFZ Heidelberg)
S24 patient-derived glioma cells	Winkler lab (DKFZ Heidelberg)
BG5 tdTom patient-derived glioma cells	Winkler lab (DKFZ Heidelberg)
P3XX pLVX MYT1L	Elisa Heinzelmann
P3XX pLVX puro (control)	Elisa Heinzelmann
S24 pLVX MYT1L	Elisa Heinzelmann
S24 pLVX puro (control)	Elisa Heinzelmann
S24 tdTom pLVX MYT1L	Elisa Heinzelmann
S24 tdTom pLVX puro (control)	Elisa Heinzelmann
BG5 tdTom shMYT1L	Elisa Heinzelmann
BG5 tdTom sh0 (control)	Elisa Heinzelmann

2.2 Commercially available cell culture reagents and buffers

Table 2: Commercially available cell culture reagents and buffers

Reagent	Supplier
Accutase (Cell Dissociation Reagent)	Life Technologies/Thermo Fisher Scientific (Carlsbad, USA)
AlamarBlue Cell Viability Reagent	Life Technologies/Thermo Fisher Scientific (Carlsbad, USA)
A83-01	StemGent (Glasgow, United Kingdom)
β-mercaptoethanol	Life Technologies/Thermo Fisher Scientific (Carlsbad, USA)
B-27 supplement	Life Technologies/Thermo Fisher Scientific (Carlsbad, USA)
B-27 Supplement (50x), minus Vitamin A	Life Technologies/Thermo Fisher Scientific (Carlsbad, USA)
bFGF	Gibco/Thermo Fisher Scientific (Carlsbad, USA)
brain-derived neurotrophic factor (BDNF)	PeproTech (Rocky Hill, NJ, USA)
Calcium chloride (CaCl2, 0.1M)	Sigma-Aldrich/Merck (Darmstadt, Germany)
Cosmic Calf Serum (CCS)	HyClone/Thermo Fisher Scientific (Carlsbad, USA)
Cytosine β-D-arabinofuranoside (AraC)	Sigma-Aldrich/Merck (Darmstadt, Germany)
D-Glucose	Sigma-Aldrich/Merck (Darmstadt, Germany)
DMEM	Gibco/Thermo Fisher Scientific (Carlsbad, USA)
DMEM-F12	Gibco/Thermo Fisher Scientific (Carlsbad, USA)
Doxycycline	Sigma-Aldrich/Merck (Darmstadt, Germany)
EDTA (Ultra pure, 0.5M, pH 8.0)	Invitrogen/Thermo Fisher Scientific (Carlsbad, USA)
rhEGF	R&D System (Minneapolis, MN, USA)

Fetal Bovine Serum (FBS)	Sigma-Aldrich/Merck (Darmstadt, Germany)
Gelatine	Sigma-Aldrich/Merck (Darmstadt, Germany)
Geltrex	Life Technologies/Thermo Fisher Scientific (Carlsbad, USA)
GlutaMAX	Gibco/Thermo Fisher Scientific (Carlsbad, USA)
Hank's Balanced Salt Solution (HBSS)	Gibco/Thermo Fisher Scientific (Carlsbad, USA)
Heparin	Sigma-Aldrich/Merck (Darmstadt, Germany)
Hygromycin B	Life Technologies/Thermo Fisher Scientific (Carlsbad, USA)
Insulin	Gibco/Thermo Fisher Scientific (Carlsbad, USA)
Knockout Serum Replacement	Gibco/Thermo Fisher Scientific (Carlsbad, USA)
Laminin mouse protein	Life Technologies/Thermo Fisher Scientific (Carlsbad, USA)
Lipofectamine Stem Transfection Reagent	Life Technologies/Thermo Fisher Scientific (Carlsbad, USA)
L-Glutamine	Lipofectamine Stem Transfection Reagent
LDN-193189	Miltenyi Biotec (Bergisch Gladbach, Germany)
Matrigel	
Minimum Essential Medium Non-Essential Amino Acids (MEM NEAA)	Gibco/Thermo Fisher Scientific (Carlsbad, USA)
mTeSR medium	StemCell Technologies (Vancouver, BC, Canada)
N2 supplement	Gibco/Thermo Fisher Scientific (Carlsbad, USA)
Neurobasal-A medium	Gibco/Thermo Fisher Scientific (Carlsbad, USA)
Opti-MEM	Gibco/Thermo Fisher Scientific (Carlsbad, USA)
Penicillin/ Streptomycin (Pen/Strep)	Gibco/Thermo Fisher Scientific (Carlsbad, USA)
Phosphate Buffered Saline (PBS, sterile)	Gibco/Thermo Fisher Scientific (Carlsbad, USA)
Polybrene	Sigma-Aldrich/Merck (Darmstadt, Germany)
Polyethyleneimine (PEI)	Polysciences (Warrington, USA)
Poly-L-ornithine (PO)	Sigma-Aldrich/Merck (Darmstadt, Germany)
Puromycin	Sigma-Aldrich/Merck (Darmstadt, Germany)
Sodium pyruvate	Gibco/Thermo Fisher Scientific (Carlsbad, USA)
TrypLE Express Enzyme	Gibco/Thermo Fisher Scientific (Carlsbad, USA)
Trypan blue	Gibco/Thermo Fisher Scientific (Carlsbad, USA)
Trypsin-EDTA, 0.25%	Gibco/Thermo Fisher Scientific (Carlsbad, USA)
XAV939	Santa Cruz Biotechnology (Dallas, TX, USA)
Y27632 (ROCK inhibitor)	Axon MEDCHEM (Groningen, Netherlands)

2.3 Homemade cell culture media and reagents

Table 3: Homemade cell culture media and reagents

Media	**Composition**
MEF medium	DMEM supplemented with GlutaMAX (1x), penicillin-streptomycin (1x), MEM non-essential amino acids (1x), sodium pyruvate (1 mM), β-mercaptoethanol (0.1 mM), cosmic calf serum (10% v/v)
Cortical induction medium	DMEM-F12; N2 (1:200), B27 (1:100), Glucose (0.2 mg/mL), cAMP (0.15 µg/mL), NEAA (0.5%), Glutamaxx (0.5%), LDN (180 nM), A83 (500 nM), Wnt-Inh. (2µM), Heparin (10 µg/mL)
Cortical differentiation medium	DMEM-F12 N2 (1:200), B27 (1:100), Glucose (0.2 mg/mL), cAMP (0.15 µg/mL), NEAA (0.5%), Glutamaxx (0.5%), Insulin (2.5 µg/mL)

GBM medium	DMEM/F12, B27 (without vit.A) (50X), Insulin (5 µg/mL), Heparin (5 µg/mL), bFGF (20 ng/ml), rhEGF (20 ng/ml), Puromycin (2 µg/mL) as needed

2.4 Commercially available molecular biology reagents

Table 4: Commercially available molecular biology reagents

Reagent	Supplier
1 kb plus DNA ladder	Invitrogen/Thermo Fisher Scientific (Carlsbad, USA)
4',6-diamidino-2-phenylindole (DAPI)	Invitrogen/Thermo Fisher Scientific (Carlsbad, USA)
Acetic acid	Honeywell (Charlotte, USA)
Agarose	Carl Roth (Karlsruhe, Germany)
Ampicillin	Sigma-Aldrich/Merck (Darmstadt, Germany)
Antarctic Phosphatase	New England Biolabs (Ipswich, USA)
Antarctic Phosphatase Buffer	New England Biolabs (Ipswich, USA)
Benzonase	Merck (Darmstadt, Germany)
Bovine Serum Albumin (BSA)	Sigma-Aldrich/Merck (Darmstadt, Germany)
Bromophenol blue sodium salt	Sigma-Aldrich/Merck (Darmstadt, Germany)
Complete protease inhibitor	Sigma-Aldrich/Merck (Darmstadt, Germany)
CutSmart buffer (10X)	New England Biolabs (Ipswich, USA)
D-Glucose	Sigma-Aldrich/Merck (Darmstadt, Germany)
DNAse	Sigma-Aldrich/Merck (Darmstadt, Germany)
Dithiothreitol (DTT)	Sigma-Aldrich/Merck (Darmstadt, Germany)
dNTP mix, 10 mM	Thermo Fisher Scientific (Carlsbad, USA)
EDTA	GERBU Biotechnik (Heidelberg, Germany)
Ethanol absoulte	VWR International (Radnor, USA)
Gel Loading Dye, Purple (6X)	New England Biolabs (Ipswich, USA)
Glacial Acetic Acid	Thermo Fisher Scientific (Carlsbad, USA)
Glycerol	Sigma-Aldrich/Merck (Darmstadt, Germany)
Isopropanol	Sigma-Aldrich/Merck (Darmstadt, Germany)
JM109 competent cells	Promega (Madison, USA)
LB Broth	Sigma-Aldrich/Merck (Darmstadt, Germany)
LB-Agar Amp	Carl Roth (Karlsruhe, Germany)
LunaScript RT SuperMix	New England Biolabs (Ipswich, USA)
Methanol	VWR International (Radnor, USA)
NP-40/IGEPAL CA 630	Sigma-Aldrich/Merck (Darmstadt, Germany)
Nucelase-free water	Qiagen (Hilden, Germany)
NuPAGE MOPS buffer (20x)	Novex/Thermo Fisher Scientific (Carlsbad, USA)
NuPAGE Transfer buffer (20x)	Novex/Thermo Fisher Scientific (Carlsbad, USA)
PageRuler Plus Pre-stained Protein Ladder	PageRuler Plus Pre-stained Protein Ladder)
Papain from papaya latex buffered aqueo	Sigma-Aldrich/Merck (Darmstadt, Germany)
Paraformaldehyde (PFA), 4%	Boster Biological Technology (Pleasanton, CA, USA)
Phosphate Buffered Saline (PBS) pellets	Th. Geyer GmbH & Co. KG (Renningen, Germany)
Power SYBR Green PCR Master Mix	Thermo Fisher Scientific (Carlsbad, USA)
QuickExtract DNA Extraction Solution	Lucigen (Middleton, USA)
Restrictions enzymes	New England Biolabs (Ipswich, USA)
Revert-700 total protein stain	LI-COR Biosciences (Lincoln, USA)

RNAse Inhibitor	Takara (CA, USA)
Roti®-GelStain Red	Carl Roth (Karlsruhe, Germany)
Sodium bicarbonate (NaHCO3)	Santa Cruz Biotechnology (Dallas, TX, USA)
Sodium chloride (NaCl)	Sigma-Aldrich/Merck (Darmstadt, Germany)
Sodium dodecyl sulfate (SDS)	GERBU Biotechnik (Heidelberg, Germany)
Sodium hydroxide solution (NaOH), 1M	Fluca/Thermo Fisher Scientific (Carlsbad, USA)
T4 DNA Ligase	New England Biolabs (Ipswich, USA)
T4 DNA Ligase Reaction Buffer	New England Biolabs (Ipswich, USA)
Trisma base (Tris base)	Honeywell (Charlotte, USA)
Triton X-100	Sigma-Aldrich/Merck (Darmstadt, Germany)
TRIzol	Life Technologies/Thermo Fisher Scientific (Carlsbad, USA)
Tween-20	Sigma-Aldrich/Merck (Darmstadt, Germany)
Vectashield mounting medium	Vectorlabs (Burlingame, CA, USA)

2.5 Homemade buffers for molecular biology

Table 5: Homemade buffers for molecular biology

Buffer	**Composition**
50X TAE-buffer	2 M Tris base, 50 mM EDTA pH 8.0, 5.75% (v/v) pure acetic acid in ddH_2O
5X SDS sample buffer	250 mM Tris base pH 6.8, 50% (v/v) glycerol, 20% (w/v) SDS, 250 mM DTT, 0.1% (w/v) bromophenol blue in ddH_2O
Base-Buffer	HBSS, EDTA (1:1000)
Embedding Solution	1x PBS, Gelatine (7,5%), Sucrose (10%)
Papain-buffer	Papain, N2, DNase I (0.025 U/µl)
PBS-T	0.1% Tween-20 in PBS
NSB Buffer	1x PBS, 0.01% BSA, 0.5 U/µl RNase Inhibitor
RIPA Buffer	150 mM NaCl, 25 mM Tris pH 7.4, 1% NP-40/IGEPAL CA 630, 0.5% sodium deoxycholate, 0.1% SDS, 1X complete protease inhibitor
Total protein stain Reversal Buffer	6.7% (v/v) glacial acetic acid, 30% (v/v) methanol in ddH_2O
Total protein stain wash solution	6.7% (v/v) glacial acetic acid, 30% (v/v) methanol in deionized water
Transfer buffer	20% methanol, 1x NuPAGE transfer buffer in ddH_2O
Virus lysis solution	1M Tris-HCl (pH 8,5) (50mM), 8,8g NaCl (0,15M), $MgCl_2$(2mM)

2.6 Commercially available kits

Table 6: Commercially available kits

Kit	**Supplier**
Direct-zol RNA MiniPrep	Zymo Research (Irvine, USA)
GenElute™ Plasmid Miniprep Kit	Macherey-Nagel (Düren, Germany)
NucleoSpin Gel and PCR Clean-up	Macherey-Nagel (Düren, Germany)
NucleoBond Xtra Midi Kit	Macherey-Nagel (Düren, Germany)
P3 Primary Cell 4D-Nucleofector X Kit	Lonza (Basel, Switzerland)
Phusion High-Fidelity PCR Kit	Thermo Fisher Scientific (Carlsbad, USA)

QiaPrep Spin Miniprep Kit	Qiagen (Hilden, Germany)

2.7 Antibodies

Table 7: Primary antibodies

Primary antibody	Dilution and application	Supplier
anti-Actin (mouse)	1:1000 Western blot	Sigma-Aldrich (Merck, Darmstadt, Germany)
anti-BrdU (mouse)	2 µg/mL Immunofluorescence	Sigma-Aldrich (Merck, Darmstadt, Germany)
anti-DCX (rabbit)	2 µg/mL Immunofluorescence	Abcam (Cambridge, UK)
anti-FLAG M2 (mouse)	1:1000 Western blot	Sigma-Aldrich/Merck (Darmstadt, Germany)
anti-GFAP (chicken)	1:500 Immunofluorescence	Sigma-Aldrich/Merck (Darmstadt, Germany)
anti-GFP (chicken)	1:1000 Immunofluorescence	Abcam (Cambridge, UK)
anti-Ki67 (rabbit)	1:500 Immunofluorescence	Abcam (Cambridge, UK)
anti-Ki67 (mouse)	1:1000 Immunofluorescence	Abcam (Cambridge, UK)
anti-MAP2 (chicken)	1:10000 Immunofluorescence	Abcam (Cambridge, UK)
anti-MAP2 (mouse)	1:1000 Western blot	Sigma-Aldrich/Merck (Darmstadt, Germany)
anti-mNeonGreen (mouse)	1:400 Immunofluorescence	Chromotek (Planeg, Germany)
anti-MYT1L (rabbit)	1:1000 Western blot, 1:1000 Immunofluorescence	Dr. Moritz Mall (Mall et al., 2017)
anti-Nestin (chicken)	1:500 Immunofluorescence	Novus Biologicals (USA)
anti-NeuN (guinea pig)	1:1000 Immunofluorescence	Synaptic Systems (Göttingen, Germany)
anti-N-CADHERIN (mouse)	1:500 Immunofluorescence	BD Bioscience (Heidelberg, Germany)
anti- p38α MAPK	1:200 Immunofluorescence	Cell Signaling Technology (Massachusetts, USA)
anti-PTEN (rabbit)	1:200 Immunofluorescence	Cell Signaling Technology (Massachusetts, USA)
anti- Phospho-S6 (rabbit)	1:200 Immunofluorescence	Cell Signaling Technology (Massachusetts, USA)
anti-SOX2 (mouse)	1:500 Immunofluorescence	Santa Cruz Biotechnology (Dallas, USA)
anti-TUJ1 (mouse)	1:1000 Western blot, Immunofluorescence	BioLegend (San Diego, USA)
anti-RFP (rabbit)	1:100 Immunofluorescence	Abcam (Cambridge, UK)

Table 8: Secondary antibodies

Secondary antibody	Dilution and application	Supplier
Alexa Fluor 488 Donkey anti-chicken	1:2000 Immunofluorescence	Thermo Fisher Scientific (Carlsbad, USA)
Alexa Fluor 488 Donkey anti-mouse	1:2000 Immunofluorescence	Thermo Fisher Scientific (Carlsbad, USA)
Alexa Fluor 488 Donkey anti-rabbit	1:2000 Immunofluorescence	Thermo Fisher Scientific (Carlsbad, USA)

Alexa Fluor 555 Donkey anti-mouse	1:2000 Immunofluorescence	Thermo Fisher Scientific (Carlsbad, USA)
Alexa Fluor 555 Donkey anti-rabbit	1:2000 Immunofluorescence	Thermo Fisher Scientific (Carlsbad, USA)
Alexa Fluor 647 Donkey anti-guinea pig	1:2000 Immunofluorescence	Thermo Fisher Scientific (Carlsbad, USA)
Alexa Fluor 647 Donkey anti-chicken	1:2000 Immunofluorescence	Thermo Fisher Scientific (Carlsbad, USA)

2.8 Plasmids

Table 9: Plasmids

Name	Source
AAV helper	Dr. Moritz Mall (DKFZ, Heidelberg)
AAV DJ	Dr. Moritz Mall (DKFZ, Heidelberg)
B3-plentiv2-NTC1 (CRISPR control)	Puch Lab (DKFZ, Heidelberg)
CAG Cre GFP	Dr. Moritz Mall (DKFZ, Heidelberg)
CAG deltaCre GFP	Dr. Moritz Mall (DKFZ, Heidelberg)
FUW-rtTA	Dr. Moritz Mall (DKFZ, Heidelberg)
lentiCRISPRv2 NF1	Lea Ballenberger
lentiCRISPRv2 PTEN	Lea Ballenberger
lentiCRISPRv2 p53	Lea Ballenberger
PB-linker-CAG MCS T2A mNeonGreen	Elisa Heinzelmann (DKFZ, Heidelberg)
PB-linker CAG_Kozak_mNeonGreen_T2A_MCS	Elisa Heinzelmann (DKFZ, Heidelberg)
PB-Transposase	Sarah Grieder (DKFZ Heidelberg)
pLVX puro	Elisa Heinzelmann (DKFZ, Heidelberg)
pVLX puro mMyt1l	Elisa Heinzelmann (DKFZ, Heidelberg)
pMDL	Addgene (#12251)
pRSV	Addgene (#12253)
pVSV-G	Addgene (#12259)
pLIX-hsMYT1L	Heather Schloo (DKFZ, Heidelberg)
pLIX-empty	Heather Schloo (DKFZ, Heidelberg)
pLIX-FLAG-NLS-MYT1L-DBD	Heather Schloo (DKFZ, Heidelberg)
pLIX-FLAG-NLS-MYT1L-DBD-VP64	Heather Schloo (DKFZ, Heidelberg)
pLIX-FLAG-NLS-MYT1L-DBD-EnR	Heather Schloo (DKFZ, Heidelberg)
pSICO-Puro-sh0	Elisa Heinzelmann (DKFZ, Heidelberg)
pSicoR-Puro-hsMYT1L sh43	Elisa Heinzelmann (DKFZ, Heidelberg)
pSicoR-Puro-hsMYT1L sh45	Elisa Heinzelmann (DKFZ, Heidelberg)

2.9 Primer

Table 10: RTqPCR primer

Target gene	Sequence
EnR	FW: CTGAGCGATCGTTTCGGAGA REV: CCTCGAAGGGGCGGAATATG
hsACTIN	FW: GGCACCCAGCACAATGAAG REV: CCGATCCACACGGAGTACTTG
hsFOXG1	FW: TGGCCCATGTCGCCCTTCCT REV: GCCGACGTGGTGCCGTTGTA

hsGAPDH	FW: CGACAGTCAGCCGCATCTT REV: GCCCAATACGACCAAATCCG
hsHES1	FW: AGGCGGACATTCTGGAAATG REV: CGGTACTTCCCCAGCACACTT
hsKi67	FW: TGCTCTGGGTTACCTGGTCT REV: GGCTTCTCCCCTTTTGAGAG
hsMAP2	FW: CAGGAGACAGAGATGAGAATTCC REV: CAGGAGTGATGGCAGTAGAC
hsMYT1L	FW: GGGCCAGCAACGGTATAGAA REV: TCAGGTTGCTCTCCATCGTG
hsNOTCH1	FW: TGAATGGCGGGAAGTGTGAAG REV: GGTTGGGGTCCTGGCATCG
hsOTX1	FW: CCAGACATCTTCATGCGAGAG REV: GGCAGGTCTCACTTTGTTTTG
hsPAX6	FW: TCCACCCGGCAGAAGATTGTA REV: TGTCTCGGATTTCCCAAGCAA
hsWNT5a	FW: ATTCTTGGTGGTCGCTAGG REV: CTGTCCTTGAGAAAGTCCTG
hsYAP1	FW: TAGCCCTGCGTAGCCAGTTA REV: TCATGCTTAGTCCACTGTCTGT
VP64	FW: GCTGACGCATTGGACGATTT REV: GCATCCGAACCAAGCATGTC

Table 11: Genotyping primer

Genomic target	**Sequence**
CamK2a	FW: CCACTTAATCCCATCCCGTC REV: ATGCAGGCAAATTTTGGTGT
mMYT1L (WT/mut)	FW: GTATGGGGAAACTGCTGAATGAA REV: GCATCCAGACAGACTGCGGTGA
mMYT1L (Δflox)	FW: GTATGGGGAAACTGCTGAATGAA REV: GAGGAGGCAACATAACTGAAGA
Nestin	FW: CGCCGCTACTTCTTTTCAAC REV: ATGCAGGCAAATTTTGGTGT
mT/mG	FW: CTCTGCTGCCTCCTGGCTTCT REV (WT): CGAGGCGGATCACAAGCAATA REV (Mut): TCAATGGGCGGGGGTCGTT
PTEN (WT/mut)	FW: CAAGCACTCTGCGAACTGAG REV: GCATTGTGCTCTTCACTCCA
PTEN (5'loxP; 4F,4R)	FW: ACTCAAGGCAGGGATGAGC REV: AATCTAGGGCCTCTTGTGCC
PTEN (Δflox; 4F,5R)	FW: ACTCAAGGCAGGGATGAGC REV: GCTTGATATCGAATTCCTGCAGC
TP53 (WT/mut)	FW: CACAAAAACAGGTTAAACCCAG REV: AGCACATAGGAGGCAGAGAC
TP53 (5'loxP; 1F,1R)	FW: CACAAAAACAGGTTAAACCCA REV: AGCACATAGGAGGCAGAGAC
TP53 (3'loxP; 10F, 10R)	FW: AAGGGGTATGAGGGACAAGG REV: GAAGACAGAAAAGGGGAGGG
TP53 (Δflox 1F, 10R)	FW: CACAAAAACAGGTTAAACCCA REV: GAAGACAGAAAAGGGGAGGG

2.10 Technical equipment and consumables

Table 12: Technical equipment

Device	Supplier
4D-Nucleofector	Lonza (Basel, Switzerland)
BioRad T100 Thermal Cycler	BioRad (Hercules, USA)
Cell Observer®	Zeiss (Oberkochen, Germany)
Centrifuge S424	Eppendorf (Hamburg, Germany)
CM3050 S Cryostat	Leica (Oberkochen, Germany)
Countess II FL Cell Counter	Invitrogen/Thermo Fisher Scientific (Carlsbad, USA)
DM IL LED Fluorescence Microscope	Leica (Oberkochen, Germany)
EasyPhor gel electrophoresis chamber	Biozym (Hessisch Oldendorf, Germany)
Electrophoresis power supply	BioRad (Hercules, USA)
GelDoc XR+ Molecular Imager	BioRad (Hercules, USA)
Hamilton Syringe	Hamilton (Bonaduz, Switzerland)
HERA cell 240i CO2 incubator	Thermo Fisher Scientific (Carlsbad, USA)
Mini Gel Tank	Invitrogen/Thermo Fisher Scientific (Carlsbad, USA)
NanoDrop One	Thermo Fisher Scientific (Carlsbad, USA)
neoBlock 1 heatblock	neoLab (Heidelberg, Germany)
ODYSSEY CLx Imaging System	LI-COR Biosciences (Lincoln, USA)
Precision balance	Kern & Sohn GmbH (Balingen, Germany)
QuantStudio 5 Real-Time PCR system	Thermo Fisher Scientific (Carlsbad, USA)
Rotanta 460R centrifuge	Hettich (Kirchlengern, Germany)
Taumelschüttler TL 10	Edmund Bühler™/Thermo Fisher Scientific (Carlsbad, USA)
Thermomixer compact	Eppendorf (Hamburg, Germany)
TI-HCS microscope	Nikon (Tokyo, Japan)
Vortexgenie 2	Scientific Industries (Bohemia, USA)

Table 13: Software

Software/Program	Supplier
Affinity Designer (version 1.10.4.1198)	Serif (West Bridgford, UK)
Benchling	Benchling Inc. (San Francisco, CA, USA)
Design and Analysis software, QuantStudio (version 2.5.1)	Thermo Fisher Scientific (Carlsbad, USA)
Fiji ImageJ (version 1.52n)	Rasband, W.S., National Institutes of Health (Maryland, USA)
GraphPad Prism (version 8+9)	GraphPad Software (San Diego, USA)
Image Lab (version 6.1)	BioRad (Hercules, USA)
Image Studio Lite (for WB, version 5.2)	LI-COR Biosciences (Lincoln, USA)
Leica Application Suite X (version 3.7.1.21655)	Leica Mikrosysteme Vertrieb GmbH Mikroskopie und Histologie (Wetzlar, Germany)
Zen Lite (version 3.4.91.0000)	Carl Zeiss Microscopy GmbH (Oberkochen, Germany)

Table 14: Consumables

Consumable	Supplier
6 cm low adhesion plates	Greiner Bio-One (Kremsmünster, Austria)
6-well tissue culture plates	Thermo Fisher Scientific (Carlsbad, USA)
12-well tissue culture plates	Corning Inc. (Corning, USA)
24-wel tissue culture plates	Corning Inc. (Corning, USA)
48-well tissue culture plates	Thermo Fisher Scientific (Carlsbad, USA)
96-well tissue culture microplate, round base	Sarstedt (Nümbrecht, Germany)
96-well tissue culture plates	Thermo Fisher Scientific (Carlsbad, USA)
384-well qPCR plate	Biozym (Hessisch Oldendorf, Germany)
Bacteria culture tubes with closure	VWR International (Radnor, PA, USA)
Blotting (Whatman) paper	neoLab (Heidelberg, Germany)
Cell culture dish (10 cm)	Thermo Fisher Scientific (Carlsbad, USA)
Cell culture dish (15 cm)	Greiner Bio-One (Kremsmünster, Austria)
Cell lifters	Santa Cruz Biotechnology (Dallas, USA)
Conical centrifuge tubes, 15 ml and 50 ml	Corning (Corning, USA)
Countess Cell Counting Chamber Slides	Life Technologies/Thermo Fisher Scientific (Carlsbad, USA)
FACS tubes	Corning (Corning, USA)
Microcentrifugation tubes (1.5 ml)	Axygen/Thermo Fisher Scientific (Carlsbad, USA)
Microcentrifugation tubes (2.0 ml)	Eppendorf (Hamburg, Germany)
Millex syringe filters (45 µm)	Sigma-Aldrich/Merck (Darmstadt, Germany)
Neubauer Cell Counting Chamber	Life Technologies/Thermo Fisher Scientific (Carlsbad, USA)
Nitrocellulose membrane	Invitrogen/Thermo Fisher Scientific (Carlsbad, USA)
NuPAGE 4 – 12% bis-tris gel	Invitrogen/Thermo Fisher Scientific (Carlsbad, USA)
Parafilm® M	Sigma-Aldrich/Merck (Darmstadt, Germany)
PCR tubes (8-strips)	Sigma-Aldrich/Merck (Darmstadt, Germany)
Petri dishes	Greiner Bio-One (Kremsmünster, Austria)
Pipette tips (10 µl, 20 µl, 200 µl, 1000 µl)	Mettler Toledo (Columbus, USA)
Pipette tips with filter (10 µl, 20 µl, 200 µl, 1000 µl)	Starlab (Hamburg, Germany)
qPCR Seal Sheets	Biozym (Hessisch Oldendorf, Germany)
Roti® Liquid barrier marker	Carl Roth (Karlsruhe, Germany)
S3023 Fluorescence Mounting Medium	Agilent (Santa Clara, USA)
Serological pipettes (5 ml, 10 ml, 25 ml, 50 ml)	Greiner Bio-One (Kremsmünster, Austria)
Syringe (30 ml)	TH. Gyer (Renningen, Germany)
Syringe (50 ml)	Sigma-Aldrich/Merck (Darmstadt, Germany)
TissueTek® OCT™	Sakura Finetek (Umkirch, Germany)
X72 Superfrost plus slides	Fisherbrand/ Thermo Fisher Scientific (Carlsbad, USA)

2.11 Mouse lines

Table 15: Mouse lines

No.	Full Name	Abbreviation	Source
1	B6;129S6-Tg(Camk2a-cre/ERT2)1Aibs/J	CamK2aCreER^{T2}	Jacksons Lab
2	B6-Tg(Nes-cre/ERT2)KEisc/J	NestinCreER^{T2}	Jacksons Lab
3	B6-Tg(Camk2a-cre/ERT2)1Aibs Gt(ROSA)26Sortm4(ACTB-tdTomato,-EGFP)Luo /Mall	CamK2aCreER^{T2} mT/mG	Generated by Elisa Heinzelmann
4	B6-Tg(Nes-cre/ERT2)KEisc Gt(ROSA)26Sortm4(ACTB-tdTomato,-EGFP)Luo /Mall	NestinCreER^{T2} mT/mG	Generated by Elisa Heinzelmann
5	B6-Myt1ltm1Ggu	Myt1l^{flox}	Guoqiang Gu (Vanderbilt School of Medicine)
6	B6-Tg Ptenm1Hwu Trp53tm1Brn / Mall	PTEN^{flox} TP53^{flox}	AG Angel (DKFZ Heidelberg)
7	B6-Ptenm1Hwu Trp53tm1Brn Myt1ltm1Ggu	PTEN^{flox} TP53^{flox}MYT1L^{flox}	Generated by Elisa Heinzelmann
8	B6-Tg(Camk2a-cre/ERT2)1Aibs Myt1ltm1Ggu	CamK2aCreER^{T2} MYT1L^{flox}	Generated by Elisa Heinzelmann
9	B6-Tg(Camk2a-cre/ERT2)1Aibs Ptenm1Hwu Trp53tm1Brn /Mall	CamK2aCreER^{T2} PTEN^{flox} TP53^{flox}	Generated by Elisa Heinzelmann
10	B6-Tg(CamK2a-cre/ERT2)KEisc Ptenm1Hwu Trp53tm1Brn Myt1ltm1Ggu	CamK2aCreER^{T2} PTEN^{flox} TP53^{flox}MYT1L^{flox}	Generated by Elisa Heinzelmann
11	B6-Tg(Nes-cre/ERT2)KEisc Myt1ltm1a(EUCOMM)Wtsi	NestinCreER^{T2} MYT1L^{flox}	Generated by Elisa Heinzelmann
12	B6-Tg(Nes-cre/ERT2)KEisc Ptenm1Hwu Trp53tm1Brn/ Mall	NestinCreER^{T2} PTEN^{flox} TP53^{flox}	Generated by Elisa Heinzelmann
13	B6-Tg(Nes-cre/ERT2)KEisc Ptenm1Hwu Trp53tm1Brn/ Mall	NestinCreER^{T2} PTEN^{flox} TP53^{flox}MYT1L^{flox}	Generated by Elisa Heinzelmann

3 METHODS

3. METHODES

3.1 Cloning

3.1.1 Molecular cloning

All plasmids (Table 9) were designed in silico using Benchling (https://benchling.com.; biology software). Vector plasmids were digested for 2 h at 37°C using the respective enzymes and dephosphorylated for 10 min at 37°C by Antarctic Phosphatase (APP). Phosphatase was heat inactivated for 20 min at 65°C. The inserts were amplified by PCR from the respective source plasmids by using Phusion polymerase and appropriate PCR programs and inserts were purified using the NucleoSpin Gel and PCR Clean-up Kit (Macherey-Nagel). The PCR amplicon was digested the same way as the plasmid vector and both were recovered with a 1.5 % agarose gel and extracted using the NucleoSpin Gel and PCR Clean-up Kit (Macherey-Nagel). By using T4 Ligase the insert was ligated into the vector plasmid in a four times molar excess and incubated for 20 min at room temperature or overnight at 16°C.

The transformation was performed in JM109 E.coli (ProMega). The competent cells were thawed on ice and 50 µl of the cells were added to 5 µl of the ligated plasmid and carefully mixed my flicking the tube followed by 20 min incubation on ice, or alternatively at 16°C overnight. Heat shock was performed for 30 sec at 42°C in a preheated water bath and tubes were recovered for 2 min on ice. Next, 1 ml LB medium was added to the mix under sterile conditions and incubated for 1 h at 37°C at the shaker (750 rpm). Cells were centrifuged for 3 min at 3000 rpm and 900 µl of the supernatant was removed. The pellet was resuspended in the remaining supernatant and plated on a LB-ampicillin-agar plate to be incubated overnight at 37°C. The next day, single colonies were transferred into 2 ml LB media containing ampicillin (100 µg/µl) and incubated for a minimum of 24 h at 37°C. The next day, plasmid DNA was extracted from 1 ml of the bacterial culture using the GenElute™ Plasmid Miniprep Kit (Macherey-Nagel). To check for successful ligation, a test digest of the plasmid was performed for 1.5 h at 37°C by the previously used digestion enzymes. Insert and plasmid vector bands were checked on a 1.5% agarose gel and sent for Sanger sequencing (Genewiz).

Remaining bacterial cultures of the successfully cloned plasmids were grown in 250 ml LB medium containing ampicillin (100 µg/µl) and shaked (250 rpm) overnight at 37°C. The plasmids were purified by using the “NucleoBond Xtra Midi Kit” (Macherey-Nagel) and concentrations were determined using a Nanodrop spectrophotometer (Thermo Fisher Scientific).

3.1.2 Gibson assembly

The Gibson assembly cloning method was used to clone multiple DNA fragments into a digested and dephosphorylated vector plasmid. Therefore, the inserts were amplified by PCR with primers containing homology arms for the respective expression vector. The plasmid vector was processed as before (1.1) and purified DNA fragments were assembled in a Gibson assembly reaction and transformed in JM109 E.coli. The following steps were performed as described in 1.1.

3.2 Virus production

3.2.1 Lentivirus production

Lentivirus was produced in HEK293T cells that were cultured in MEF media (Table 3) and kept at 37°C and 5% CO_2. One day before transfection, 8 million cells were seeded in 10 ml MEF media on a poly-L-Ornithine (15 mg/L in PBS) pre-coated 10 cm dish. One hour before transfection media was exchanged with 10 ml fresh MEF media. Per transfection reaction, lentiviral envelope, and packaging plasmids (3.125 µg pRSV, 3.125 µg pVSV-G, and 6.25 µg pMDL) were combined with the transfer plasmid of interest (12.5 µg) in 500 µL OptiMEM and vortexed. The mix was added to 500 µL PEI transfection mix (425 µL OptiMEM+75 µL polyethyleneimine) and thoroughly vortexed for 10 sec. After incubation for 15 min at RT, the transfection mix was added dropwise to the cells. The cells were washed with PBS after 4-5 hours and supplied with fresh MEF media. At 24 and 48 h post transfection, the supernatant was collected and stored at 4°C. The supernatant was filtered through a 0.45 µm filter to remove cell debris and subsequently ultracentrifuged for 2 h at 4°C at 23,000g. Supernatant was removed and the virus pellet was resuspended in DMEM to 100X concentration overnight. Next day, the virus was aliquoted and stored at -80°C.

3.2.2 AAV virus production

AAV Virus was produced following the protocol established by the lab of Prof. Dr. Grimm (DKFZ Heidelberg). HEK293 cells were seeded in a density of $4x10^6$ cells per 15 cm dishes. After two days, transfection by a PEI transfection mix containing the plasmids (construct, pHelper and pAAV-DJ; 14,7 µg each plasmid per plate), 0.4 ml PEI, 1.25 ml sterile water and 1.9 ml sterile NaCl per plate was performed. After vortexing and incubating for 10 min, the mix was added drop wise to the plates. The virus was harvested three days after transfection by scraping of the cells and collecting the cell suspension in conical tubes. Cell suspension was centrifuged for 15 min at 400g at RT. The supernatant was discarded, and the pellet was resuspended in 20 ml PBS, followed by another round of centrifugation with the same settings. The supernatant was removed, and the pellet was resuspended in 20 ml virus lysis solution. In five repeating freeze-thaw cycles, the mix was kept in liquid nitrogen for 5 min and transferred to 37°C for thawing. Next, the virus was purified by

iodixanol gradient centrifugation. Therefore, the solution was sonicated for 1 min and 20 sec and 75 µl/ml benzonase was added. The samples were then incubated for 1 h at 37°C and inverted every 10 min. Afterwards, samples were centrifuged for 15 min at 4000g at 4°C. The supernatant was transferred to a new falcon. New virus solution was added, and the step was repeated. The virus solution was then transferred to a Beckman centrifuge tube and Iodixanol was added in the following order: 7 ml 15% Iodixanol, 5 ml 25% Iodixanol, 4 ml 40% Iodixanol, 4 ml 60% Iodixanol. Tubes were sealed and centrifuged 2.5 h with 50,000 RPM at 4°C in an ultracentrifuge. After centrifugation the virus particles, which accumulate in the 40% Iodixanol phase, were soaked out by using the needle (20Gx1.5, Nr.2, 0.8x40mm). Virus was aliquoted and stored at -80°C

3.3 Cell culture

3.3.1 hESC and iPSC culture

H1 human embryonic stem cells (hESCs) and C6 induced pluripotent stem cells (iPSCs) were maintained in mTeSR medium in feeder-free conditions at 37°C and 5% CO_2. Both hESCs and iPSCs were passaged when confluent on 6-well plates precoated with Geltrex (1:200 in DMEM) for at least 30 min at 37°C. First, cells were washed with PBS and then incubated for 3 min at 37°C in 1 mL EDTA (0.5mM) in PBS. After two washes with PBS, the cells were resuspended in 1 mL mTeSR and seeded in a ratio between 1:4 to 1:6 in 1.5 mL mTeSR with ROCK inhibitor (Y-27632, 10 µM).

3.3.2 Patient-derived glioma cell lines

Different patient-derived glioma cell lines (Table 1) were cultured in suspension in GBM medium (Table 3). Media was changed every 3-4 days. Growth factor supplements bFGF and rhEGF, as well as puromycin (each 2 µg/µl) when required, were added immediately prior to medium changes.

3.3.3 Transduction of patient-derived glioma cell lines

In order to genetically manipulate patient-derived glioma cell lines, they were transduced with lentiviruses containing doxycycline-inducible or constitutive expressed insert with puromycin resistance domains. Therefore, the spheroid suspension was centrifuged at 300g for 4 min and resuspended in 500 µL Accutase to create a single cell suspension. After 4 min of incubation at room temperature with gentle pipetting midway, the reaction was quenched with 4.5 mL DMEM-F12 and centrifuged for another 4 min at 300g and resuspended in GBM medium. Cells were seeded at a density of between $1x10^6$ to $0.4x10^6$ cells per well of a 6-well plate in 2 mL GBM medium and incubated with polybrene (10 µg/mL) for 15-30 min at 37°C. After the incubation, 16 µL of virus was added per well and gently mixed. After 24 h the medium was changed, and after 48 h cells were exposed to puromycin selection (2 µg/mL) with medium changes every 3-4 days.

3.4 Molecular biology

3.4.1 Agarose gel electrophoresis

Gel electrophoresis was used for analysis and purification of DNA. Samples were mixed with 6x gel loading buffer and loaded onto a 1 -1.5% (w/v) agarose gel prepared with 1xTAE and supplemented with Gel Red Stain (1:10,000). Gels were run at 120V for 30-60 min. A 1 kb DNA Ladder (Thermo Fisher Scientific) was used as a reference and gels were detected with the Geldoc System (Bio-Rad).

3.4.2 Isolation of DNA

Plasmid DNA from bacteria was purified, using the Plasmid Miniprep Kit (Macherey-Nagel) and NucleoBond Xtra Midi Kit (Macherey-Nagel) according to the manufacturer's protocol.
Genomic DNA from cells was isolated by using the QIAamp DNA Blood Mini Kit (Qiagen) according to the manufacturer's protocol.
Genomic DNA from formalin-fixed mouse brain sections was extracted using the QIAamp DNA FFPE Advanced Kit (Qiagen) according to the manufacturer's protocol. DNA was eluted in 25 µl nuclease-free water and the final concentration was determined by the Nanodrop spectrophotometer (Thermo Fisher Scientific).

3.4.3 RNA isolation

For RNA isolation, cells were harvested, washed, and centrifuged at 13.000 rpm for 3 min and resuspended in 200 µl TRIzol. RNA was extracted with the Direct-zol RNA Miniprep kit (Zymo Research, Irvine, USA) according to the manufacturer's manual. RNA was eluted in 25 µl nuclease-free water and the final concentration was determined by the Nanodrop spectrophotometer (Thermo Fisher Scientific) and stored at -80°C.

3.4.4 Reverse Transcription

The LunaScript RT Super Mix Kit (New England Biolabs) was used to prepare cDNA of isolated RNA samples according to the manufacturer's protocol. cDNA was diluted in nuclease-free water depending on the required concentrations and stored at -20°C.

3.4.5 Real time quantitative polymerase chain reaction (RTqPCR)

Transcription levels from cDNA templates were determined by RTqPCR using SYBR Green PCR Master Mix (Thermo Fisher Scientific) and the QuantStudio5 Real Time PCR system (Thermo Fisher Scientific). qPCR reactions were performed in triplicates in 384-well plates, per well containing 2.5 µl cDNA, 5 µl SYBR Master mix, 2.1 µl nuclease-free water and 0.4 µl primer mix. RTqPCR results were analyzed using the ExpressionSuite software (Applied Biosystems by Thermo Fisher Scientific).

Ct values were normalized to GAPDH and Actin as housekeeping genes. Mean fold changes of expression were calculated by the ΔΔCT method. Data processing and visualization was performed in MS Excel and GraphPad prism.

3.5 Protein Biochemistry

3.5.1 Protein harvest and quantification of concentration

Cells were washed with PBS and harvested in RIPA buffer containing protease inhibitor (1:100) and sonicated for 45 sec in 3 cycles with a 60 sec cool down in between. Then, protein concentration was determined by the Pierce BCA Protein Assay Kit (Thermo Fisher Scientific) according to the manufacturer's protocol. Absorption was measured by the MULTISKAN FC spectrometer (Thermo Fisher Scientific).

3.5.2 Western Blot

Protein samples were prepared by adding 1xSDS and heated to 98°C for 2 min followed by adding benzonase (1:200). Samples were separated by SDS polyacrylamide gels at 100 – 120 V at RT in cold MOPS buffer using the NuPAGE 4-12% Bis-Tris gels (Invitrogen). Afterwards, proteins were transferred by wet blotting onto a nitrocellulose membrane overnight at 75mA in transfer buffer using the Mini-PROTEAN Tetra System (Bio-Rad). Next day, total protein was measured by Revert-700 total protein stain (LI-COR) and imaged, using the ODYSSEY CLx Imaging System (LI-COR). After reversion of the total protein stain by reversal buffer for 5 min, the membrane was blocked in 2% BSA in PBS-T for at least one hour at RT. Primary antibodies diluted in 2% BSA PBS-T were added to the membrane and incubated overnight at 4°C on a shaker. Next day, the membrane was washed three times 10 min with PBS-T and incubated with secondary antibody diluted 1:10.000 in 2% BSA in PBS-T for 1 hour at RT on a gentle shaker. Prior to imaging with the ODYSSEY CLx Imaging System (LI-COR), membrane was again washed three times 10 min with PBS-T. Protein was quantified by the Image Studio Lite Software (LI-COR) and normalized to total protein stain or housekeeping protein Actin.

3.6 Animal models and experiments

All genetically modified mice, that I bred for the experiments (Table 11) have a BL/6 background. Mice were housed in standard housing conditions in the central animal facility of the German Cancer Research Center following the regulations of the German Animal Welfare Act. The mice were housed in a 12h light/dark cycle with food and water *ad libitum*. All animal experiments were performed according to the protocols approved by the regional council (Regierungspräsidium Karlsruhe).

3.6.1 Animal experiment 1: Tracing lineage specific Cre-expression and gene modification in neural stem cells and postmitotic cells

In order to check for sufficient cre recombination and specific gene deletion, mouse cre lines (CamK2aCreER^{T2} and NestinCreER^{T2}; Table 11) were breed with mT/mG reporter mice. The obtained mice were injected with tamoxifen (2 mg/100 µl i.p.) or corn oil as a vehicle control on four consecutive days at the age of 4 weeks and harvested either 2 weeks after injection or 2 months after injection. Four hours prior to the perfusion, mice were injected with BrdU (300 mg/kg i.p.). Perfused brains were incubated in 4% PFA for 24 hours and transferred into 10% sucrose solution overnight and stored in 20% sucrose until cryosectioning.

3.6.2 Animal experiment 2: Effect of MYT1L deletion in neural stem cells and postmitotic cells on differentiation and glioma formation

Genetically modified mouse lines were obtained by breeding mouse lines MYT1L^{flox}, Pten^{flox}p53^{flox} and Pten^{flox}p53^{flox}Myt1l^{flox} mice (Table 11; No. 5-7) with CamK2aCreE^{T2} and NestinCreER^{T2} mice. These mice were injected with tamoxifen (2 mg/100 µl i.p.) or corn oil as a vehicle control on four consecutive days at the age of 4 weeks. Four months after injections, mice were subjected to regular MRI examinations. The experiment duration is set by a maximum of 24 month. If termination criteria (weight loss of maximum 20%, lethargy or neurological symptoms) were met, mice were immediately harvested. Four hours prior to the perfusion, mice were injected with BrdU (300 mg/kg i.p.). Perfused brains were incubated in 4% PFA for 24 hours and transferred into 10% sucrose solution overnight and stored in 20% sucrose until cryosectioning.

3.6.3 Animal experiment 3: Intracranial injection of AAV-Virus and analysis of glioma formation in dependence of MYT1L

AAV-Virus (Syn Cre and SynΔCre) was injected intracranial into mouse lines number 5-7 (Table 11). Injections were performed using stereotactic equipment (Bilaney Consultants GmbH) and a Nanoliter injector (WPI). Mice were injected with 500 nl AAV virus solution at the age of 3 or 6 weeks into the left cortex (coordinates y: -2.3; x: 1.5; z: -1.3). Four months after injections, mice were subjected to regular MRI examinations. The experiment duration is set by a maximum of 24 month. If termination criteria (weight loss of maximum 20%, lethargy or neurological symptoms) were met, mice were immediately harvested. Four hours prior to the perfusion, mice were injected with BrdU (300 mg/kg i.p.). Perfused brains were incubated in 4% PFA for 24 hours and transferred into 10% sucrose solution overnight and stored in 20% sucrose until cryosectioning.

3.6.4 Nuclei isolation and flow cytometry of GFP positive brain tissue

AAV injected animals were harvested 3 weeks after injection and brains were harvested and slices of 2 mm thickness were obtained. Brain slices were transferred to a 6 cm dish containing HBSS medium. Under the dissection microscope, protected from light and with the help of a laser lamp, GPF positive tissue was dissected from the brain tissue slices and transferred to a 1.5 ml Eppi. Tissue pieces were snap frozen in liquid nitrogen and stored at -80°C.

For nuclei isolation, frozen tissue was transferred in 350 µl TST buffer in a petri dish and homogenized quickly on ice with a scalpel. The suspension was transfer to a 1.5 ml Eppi and further homogenized with little plastic pestle. The solution was filtered through a 30 µm strainer and the filter was washed with additional 350 µl TST buffer. After centrifugation for 5 min at 500xg at 4°C, supernatant was removed and the pellet was resuspended in 200 µl NSB buffer and filtered through the 20 µm strainer of the FACS tube cup. FACS was performed with the BD FACS Aria III at the open sequencing lab (DKFZ Heidelberg). Samples were gated for AlexaFlour-488A positive cells and directly sorted into a 96 well plate containing lysis buffer. Flow-cytometry was performed using a 70µm nozzle.

3.6.5 Implantation of modified PDGCs and two photon microscopy

Implantation of patient-derived glioma cells lines (PDGCs) and two photon microscopy was performed by Dr. Erik Jung (University clinic Heidelberg). First, chronic cranial windows were implanted in MRI nude mice (Charles River). Two weeks after window implantation 30,000 fluorescently labeled PDGCs suspended in PBS were intracranially implanted in a depth of 500 µm. Intravital two photon microscopy was performed with a Zeiss 7MP microscope (Zeiss) equipped with a Coherent Chameleon Ultra II laser (Coherent) on anesthetized mice (4% isoflurane for initiation, 0.5–2% for maintenance of anesthesia).

3.6.6 MRI examinations

MRI examinations were performed by the “Small Animal Imaging Center” at the DKFZ. Animals were measured at the 9.4 Tesla small animal tomograph (BioSpec 3T, BioSpec 9.4T, 23 Bruker, Germany). First, T2-weighted images were taken for morphological analysis. In case of abnormalities and lesions, T1-weighted imaging was performed after injection of contrast media (80 µl ProHance, 0,5 mmol/kg bodyweight, Bracco). During MRI examinations, animals received narcosis (3 - 3,5 Vol. % sevoflurane with 0,5 l/min air).

3.7 GBM organoid tumorigenesis model

3.7.1 Generation of cortical organoids

Forebrain organoids were generated using a protocol adapted from Krefft et al. (2018). In order to form embryoid bodies (EBs), H1 hESCs or C6 iPSCs were seeded by incubating one well with 80% confluently of a 6-well plate with 500 µL TrypLE Express at 37°C for 7 min. The reaction was quenched by adding 2 mL DMEM-F12 to the well. Cell suspension was transferred to another 8 ml DMEM-F12 and cells were counted, using the cell counter (Countess II FL; Invitrogen). Resuspended cells were added to the required amount of mTeSR media with ROCK inhibitor (Y-27632, 50 µM) in order to seed 9.000 cells per well in 150 µL media in low-attachment round-bottom 96-well plates. After seeding cells were spined down at 300g for 5 min in each direction. The EBs were monitored daily for changes in morphology and to check that they formed clear borders. Every day, the mTeSR media was changed by gently aspirating 100 µL media and adding 100 µL fresh media per well. Four to six days after seeding, the EBs approached a diameter of 500-600 µm and mTeSR medium was removed and changed to cortical induction medium (Table 3). Spheroids were monitored for the formation of neuroectoderm as evidenced by brightening near the edges, which usually occurred within 4-5 days of cortical induction medium. Then, EBs were pooled into a 6 cm dish containing fresh cortical induction medium and the next day they were embedded. Embedding was performed by transferring EBs to ethanol- and UV-treated parafilm molds, aspirating remaining media, and incubating in 10 µL Geltrex for 20 m at 37°C. Afterwards, EBs were transferred back to a 6 cm dish with cortical induction medium. Next day, EBs were transferred to the orbital shaker (16 movements per min) and the following day, media was changed to differentiation media (Table). Differentiation media was changed every 3 to 4 days.

3.7.2 GBM organoid tumorigenesis model

Cortical organoids were utilized to generate a model of GBM tumorigenesis by introducing tumorigenic events by CRISPR/Cas9. Forebrain cortical organoids were generated as described before. On day after pooling the organoids into a 6 cm dish with cortical induction medium, EBs were electroporated by the 4D Nucleofector (Lonza) to introduce different combinations of CRISPR/Cas9 sgRNAs against NF1, PTEN, and TP53 and a negative, scrambled control. Additionally, I introduced shRNA against MYT1L or control shRNA (sh0). All conditions and plasmid combinations can be seen in Table 16 and all conditions were co-electroporated with a Piggybac plasmid, containing mNeonGreen and a Transposase plasmid. Plasmids were added to P3 solution (Lonza) with a total concentration of 100 ng for each plasmid, incubated for 10 min at RT and loaded onto a Lonza Nucleocuvette strip. For electroporation of the EBs, Nucleofector program CB115 was chosen. After nucleofection, EBs had to rest for another 15 min in the cuvette at RT and were then

transferred into a 24 well low attachment plate containing cortical induction medium. One day after electroporation, EBs were cleaned from debris, transferred to a low-attachment round-bottom 96-well plates, and “day1” fluorescent images of the mNeonGreen signal were taken on three different z-planes for later analysis (Leica DMIL LED). On day 2 after electroporation, the EBs were embedded and gently transferred back to cortical induction media. The following day, they were transferred to the orbital shaker. On day 4, neuroepithelial loop structures began to form and the EBs were switched to cortical differentiation media, which was changed every 3-4 days. On day 28 fluorescent intensity of mNeonGreen was acquired from three different z-planes. Prior to imaging, organoids were applied to FACS or fixed for histological analysis.

Table 16: Experimental design for cerebral tumor organoid model including MYT1L sh-mediated KD
Concentrations for one nucleofection mix (20 µl) containing 8 EBs.

Condition	**lentiCRISPRv2 Construct**	**shRNA**	**Piggybac-mNeonGreen + Transposase**
Control	200ng CRISPR ctrl.	200ng *sh0*	100ng PB-mNG 100ng Transposase
NF1/PTEN/TP53	66.6ng *NF1* 66.6ng *PTEN* 66.6ng *TP53*	200ng *sh0*	100ng PB-mNG 100ng Transposase
PTEN/TP53	66.6ng *PTEN* 6.66ng *TP53* 66.6ng CRISPR ctrl.	200ng *sh0*	100ng PB-mNG 100ng Transposase
PTEN/TP53/shMYT1L	66.6ng *PTEN* 66.6ng *TP53* 66.6ng CRISPR ctrl.	200ng *shMYT1L*	100ng PB-mNG 100ng Transposase
shMYT1L	200ng CRISPR ctrl.	200ng *shMYT1L*	100ng PB-mNG 100ng Transposase

3.8 Histology and Immunohistochemistry

Tissue sections of harvested mouse brains, cortical organoids and fixated cells were subjected to histological analysis.

3.8.1 Histology of cortical organoids

For fixation, organoids were transferred to 24 well plates and washed once with PBS before 500 µL of 4% paraformaldehyde (PFA) for 15 min at 4°C. After three 10 min PBS washes at RT under gentle shaking, 30% sucrose in PBS was added and organoids were stored at 4°C prior to embedding for cryosectioning.

For embedding, the organoids were transferred to a 2 mL tube and sucrose solution was exchanged with a homemade embedding solution (Table 5). The organoids were moved to embedding molds sitting on ice and solidified slowly for around 20 min. The samples were then frozen in pure ethanol mixed with dry ice and stored at -80°C. Cryo-sectioning was performed at a Leica CM 3050S cryostat at a chamber temperature of -20°C and an object temperature of -20°C. Samples were frozen onto the object plate with TissueTek® O.C.T. compound before 16 µm thick slices were collected on SuperFrost Microscope slides. Slides were stored at -80°C.

Cover slides containing the cryosections were thawed at RT until they were dry and circled with ROTI®Liquid Barrier Marker. For immunofluorescence staining (IF), the respective sections were blocked with 3% BSA + 0.5% Triton in PBS for 1 h at RT and incubated with primary antibody solutions (Table 7), diluted in 3% BSA + 0.2% Triton in PBS, at 4°C overnight. The following day, slides were washed three times with 0.2% Triton in PBS for 10 min at RT and then once with 3% BSA + 0.2% Triton in PBS for 10 min at RT before they were incubated with secondary antibody solutions (Table 8), diluted 1:500 in 3% BSA + 0.2% Triton in PBS, for 2 h at RT protected from light. Slides were washed two more times with 0.2% Triton in PBS for 10 min and incubated with DAPI (1:10,000 in PBS) for 10 min. Finally, the samples were washed once with PBS and rinsed with water before air drying, away from light, at RT and being mounted.

3.8.2 Histology of mouse brain sections

Cryosections of PFA-fixated adult mouse brains, as well as hematoxylin and eosin (H&E) staining, were prepared by the light microscopy facility with a thickness of 7-10 µm. IF Staining was performed as described in 3.8.1 with appropriate primary and secondary antibodies (Table 7,8).

3.8.3 Histology of fixated cells

For IF staining, cells were first washed with PBS to remove cell debris and then fixed with 4% PFA for 15 min at 4°C. Cells were washed three times with PBS and either stored at 4°C or directly processed for staining. Permeabilization was performed with 0.5% Triton X-100 in PBS for 5 min at RT, followed by blocking with 2% BSA in PBS for 2h at RT. Primary antibodies were diluted in blocking buffer and incubated overnight at 4°C. The next day, cells were washed three times for 15 min in blocking buffer, incubated in secondary antibody diluted in blocking buffer (1:500) for 1 h at RT protected from light, washed three times for 15 min in blocking buffer and incubated for 5 min in detergent (0.1% (w/v) Triton X-100, 0.02% (w/v) SDS in PBS). For post-fixation, cells were incubated for 5 min in 4% PFA containing DAPI (1:10,000). Cells were flushed with PBS and kept in PBS at 4 °C.

3.9 Imaging

Brightfield images (BF) and fluorescence images of whole organoids were taken on a DM IL LED fluorescence microscope (Leica) and the LAX software (Leica) with 4x, 10x magnification. IF stainings of organoid cryosections as well as brain cryosections were imaged either using the Zeiss Cell Observer® with a 10x objective, the Slidescanner (Zeiss) microscope, or the Zeiss LSM 700 confocal microscope. Image processing was performed using ImageJ.

3.10 Experimental assays

3.10.1 Spheroid invasion assay

In order to investigate the invasion capacity of GBM patient derived cell lines, 3D spheroid invasion assay was performed. In preparation, 48-well plates were set up with 190 µL Matrigel or Geltrex per well on ice with the outermost wells filled with PBS. Single spheroids of the GBM cell line were washed in DMEM-F12 and then transferred to the center of the well and incubated at 37°C for 1 h. After the gel matrix solidified, 500 µL media was added per well. In the case of spheroids previous transduced with inducible plasmids, half of the spheroids per condition were induced with doxycycline (2 µg/mL). Spheroids were imaged with 4x BF on days 0, 3, 5, and 7. Additionally, fluorescent images of the tdTomato signal were acquired. After imaging on days 3 and 5, 200 µL more media was added to ensure continuous dox-induction and fresh growth factors. In parallel to the invasion assays, protein and RNA were harvested from flasks of the same cells grown in suspension. Invasion in BF images was quantified by averaging 20 manually drawn measurements from the center of the spheroid core to the outermost invading cells. Total invasion length was defined as the average of the lines from spheroid core to outside invading cells and net invasion length was defined as the average total invasion length minus the radius from spheroid center to border of the core. All invasion length quantifications at day 3, 5, and 7 are normalized to same spheroid's radius at day 0.

Additionally, with a designed macro (Heather Schloo), parameters of the whole spheroid area and in invasion density were analyzed based on the tdTomato fluorescence. Each image was binarized at a first threshold to define the core region of interest (ROI), and record the area, the mean grey intensity (average pixel intensity), and the raw integrated density (sum of pixel intensities) for the spheroid core. Then a second lower threshold was used to binarize the image to capture the invading cells as well. At this threshold, the whole spheroid is quantified in pixel amount, and the invasion zone density is also calculated by subtracting the core area. For all fluorescent quantifications, each spheroid has been normalized to its own area at day 0 prior to any other comparisons or analyses.

3.10.2 Alamar blue assay

Cell viability and proliferation of patient derived GBM cells were measured using the AlamarBlue assay (Invitrogen) at days 0, 3, 5, and 7. In preparation, a single cell suspension was obtained after centrifugation of spheroids (300g for 4 min) and incubation in 250-400 µL Accutase for 4 min at RT with gently pipetting midway. The suspension was quenched with 4 ml cold DMEM-F12, recentrifuged at 300 g for 4 m, resuspended in GBM media, and then seeded in 96-well plates (Greiner) in 100 µL GBM media at a density of 500 cells per well. To prevent drying out, the outermost wells were filled with PBS. On days 2, 4, and 6, an additional 20 µL of medium was added to each well to ensure the continual presence of the required growth factors and, if required, the maintenance of dox-induction. On the day of measurement, 10 µL of AlamarBlue reagent was added to each well and incubated for 2.5 h at 37°C and 5% CO2. The active compound in AlamarBlue dye is resazurin (IUPAC name: 7-hydroxy-10- oxidophenoxazin-10-ium-3-one), a non-toxic redox indicator dye that permeates cell membranes (Rampersad, 2012). Within viable cells, resazurin is metabolically reduced from its non-fluorescent, oxidized state, to resorufin, its fluorescent, reduced state. The fluorescence intensity was measured using a Tecan infinite M1000Pro microplate reader with an excitation wavelength of 535 nm and an emission wavelength of 590 nm.

3.10.3 2D monolayer assay

The capability of patient derived GBM cells to form connected networks with each other by tumor microtubes (TM) formation was investigated by using an *in vitro* 2D monolayer assay. This assay was performed in collaboration with Dirk Hoffmann (DKFZ Heidelberg). S24tdTom cells with constitutive MYT1L overexpression, BG5 tdTom cells with MYT1L knockdown and their associated controls were cultured on Matrigel® in GBM medium under serum-free stem-like conditions. These conditions preserve both gene expression and typical biological GBM features, such as the diffuse growth and network formation. Before seeding, a 96-well plate was coated with Matrigel® diluted 1:50 in DMEM-F12 medium and allowed to solidify at 37°C for 1 h. Cells were singularized using Accutase, washed with PBS and resuspended in GBM medium and 7,000 (for S24) to 10,000 (BG5) cells were seeded per well. After 3 days of incubation at 37°C and 5% CO2, Hoechst33342 was added to a final concentration of 1ug/ml final concentration and incubated for 30 min at 37°C. Imaging was performed using the LSM 780 confocal microscopy and a heat-controlled chamber with 37°C and 5% CO2. Images were acquired at 405 nm excitation (Hoechst33342) and 555 nm excitation (tdTom) with 20x dry objective. At least 12 ROIs per condition. For image processing, Fiji 2.0.0 for channel splitting and generating of orthogonal projections was used. Next, machine-learning based semi-automatic image analysis of TM lengths and nuclei numbers was performed with the open-source software Ilastik. TMs per cell were calculated based on the sum of all objects lengths per ROI

divided by the number of cells per ROI. The total number of nuclei per ROI were quantified manually using Fiji 2.0.0. Only ROIs with a comparable number of cells were selected for analysis.

3.11 Sequencing

3.11.1 Bulk RNA sequencing

The overexpression of MYT1L by the pLVX MYT1L plasmid was tested in 3D suspension culture in different patient derived GBM cell lines (S24tdTomato, p3xx) and bulk RNA sequenced. Three biological replicates of each cell line and their respective controls (pLVX puro) were harvested, and the RNA was isolated as described previously (see 3.4.3) and sent to the DKFZ NGS Core Facility for library preparation and bulk RNA sequencing. Paired-end sequencing reads (100bp) were generated on NovaSeq 6000 S4 platforms (Illumina).

Bulk-RNA-sequencing of RNA isolated of prefrontal cortices from mice of animal experiment 2 (3.6.2) was sent to the DKFZ NGS Core Facility for library preparation and bulk RNA sequencing. Paired-end sequencing reads (100bp) were generated on NovaSeq 6000 S4 platforms (Illumina).

For Ultra Low RNA sequencing of AAV injected mice (3.6.3), RNA isolated from FACS sorted nuclei (animal experiment 3; 3.6.4) and libraries (prepared by the Open Sequencing Lab, DKFZ Heidelberg) was sent to the DKFZ NGS Core Facility. Paired-end sequencing reads (100bp) were generated on NovaSeq 6000 S1 platforms (Illumina).

Bioinformatic analyses were supported by Bryce Lim and Laura Rueda Gensini (Mall lab, DKFZ Heidelberg) and Hai Ling (Wick lab, DKFZ Heidelberg). Using STAR, raw reads were mapped to the hg38 reference genome (Dobin et al. 2013) and the differential expression was ascertained with DESeq2 (Love et al. 2014) (R package version 1.28.1) with size factor normalization and Wald significance tests. GO analyses were performed using Enrichr (Kuleshov et al. 2016) and pathway analysis was performed by Ingenuity Pathway Analysis Software (QIAGEN Inc., https://www.qiagenbioinformatics.com/products/ingenuity- pathway-analysis). Differentially expressed genes with p-adjusted values of less than 0.01 were considered significant.

3.12 Data processing and statistical analyses

All statistical analyses were performed with GraphPad Prism 8. Results were expressed as the mean ± standard error of the mean (SEM) or mean ± standard derivation (SD).

For comparison of control vs. mutant samples, ordinary one-way ANOVA was performed with correcting for multiple comparisons using Dunnett's test. Normalized replicate values (e.g. protein or RNA expression of mutants normalized to the reference sample) were tested using the non-parametric statistical Friedman test, and correcting for multiple comparisons using the Dunn's test. For comparison of survival low-rank (Mantel-Cox) test was performed.

For all statistical tests, p-values of less than 0.05 were considered significant (*p < 0.05, ** p < 0.01, *** p < 0.001, **** p < 0.0001).

MYT1L gene expression comparison was generated using Gene Expression Profiling Interactive Analysis (GEPIA) with data from TCGA and Genotype-Tissue Expression (GTex; (https://www.gtexportal.org/home/) (Tang et al., 2017).

Organoid, spheroid, and mouse brain images were processed and analysed using Zen Lite 3.4, Fiji ImageJ (2.3.0/1.53p) / Java 1.8.0 172), and Leica Application Suite X (version 3.7.1.21655).

Protein levels were quantified using Image Studio Lite v.5.2, and qPCR experiments were designed in Design and Analysis software (QuantStudio (version 2.5.1).

For a complete listing, see Table 2.14. qPCR data was normalized to GAPDH and Kolmogorov-Smirnov tests were run to check for normal distribution, then paired two-sided t-tests were used to test for significance. Unpaired two-sided t-tests were performed for all spheroid invasion assay analyses, AlamarBlue assays, and connectivity scores.

4 RESULTS

INVESTIGATING THE ROLE OF MYT1L IN GLIOMA PATIENTS

DEDIFFERENTIATED MATURE NEURONS AS ORIGIN OF GBM

Spatially-restricted depletion of MYT1L in neurons

Spatially-restricted MYT1L depletion in neurons induced tumor formation

Generation and validation of genetic tumor mouse model

Destabilization of neuronal cell fate upon MYT1L depletion

Depletion of MYT1L in progenitor cells

MYT1L - A POTENTIAL TUMOR SUPPRESSOR

Establishing a cortical organoid protocol

MYT1L loss promoted proliferation in cerebral organoid tumor model

MYT1L inhibited tumor cell proliferation in PDGCs

MYT1L decreased invasion of PDGCs

MYT1L affected invasion and proliferation by transcriptional repression

MYT1L reduced tumor microtube formation of PDGCs

MYT1L inhibited tumor cell invasion and proliferation *in vivo*

MYT1L expression upregulated neuronal gene programs

REGULATION OF GBM SUBTYPE IDENTITY BY MYT1L

4. RESULTS

4.1 Investigating the role of MYT1L in glioma patients

Previous studies have indicated a connection between the transcription factor MYT1L and gliomas. Therefore, I investigated the correlation of MYT1L expression and survival in glioma patients. The following analysis was performed together with a supervised student, Felix Schüssler. By using GEPIA, a tool that compares GTEx data with expression data from the TCGA dataset, I found significant changes in MYT1L expression in various cancers, compared to normal control tissue (Fig. 5A). MYT1L expression was significantly decreased in GBM, low grade-glioma (LGG), and in testicular germ cell tumors (TGCT) compared to respective non-malignant controls. Testicles represent the only non-neuronal tissue in which MYT1L expression can be detected. In contrast, MYT1L was significantly upregulated in tumors of the autonomic nervous system, in so-called pheochromocytomas/paragangliomas (PCPG).

Focusing on brain cancer specifically, MYT1L expression levels were further investigated in collaboration with Marcel Kool (DKFZ Heidelberg) by utilizing DKFZ patient RNA-sequencing datasets. Here, MYT1L appeared to be most highly expressed in glioma, GBM, and medulloblastomas (MB) (Supp. Fig.1A). Within GBM, the highest level of MYT1L expression was found within the proneural (PN) subgroup (according to the Verhaak classification) while the lowest MYT1L expression was observed in the mesenchymal (MES) subgroup (Fig. 5B). To explore whether MYT1L can be linked to specific cellular states of GBM, single cell RNA-sequencing data from Neftel et al. (2019) was analyzed by Bryce Lim (DKFZ, Heidelberg). MYT1L specifically and exclusively marked neural progenitor cell-like 2 (NPC-2 like) GBM cells, suggesting that MYT1L is a marker and potentially even a regulator of this GBM subtype (Fig. 5C). Interestingly, the proneural/NPC-like subtype of GBM has the most favorable outcome for patients (Patel et al. 2014), while mesenchymal/MES-like has the worst prognosis (Klughammer et al. 2018). Consequently, we investigated the correlation of MYT1L expression level with GBM patient survival. In an attempt to recreate published survival data of Melhuish et al. (2018) using the same database (Betastasis) and settings as stated, the striking difference between MYT1L low/high expressing groups could only be reproduced in parts. There was a tendency towards better survival for high MYT1L expression, but to a smaller and statistically non-significant extent than reported (Fig. 5D).

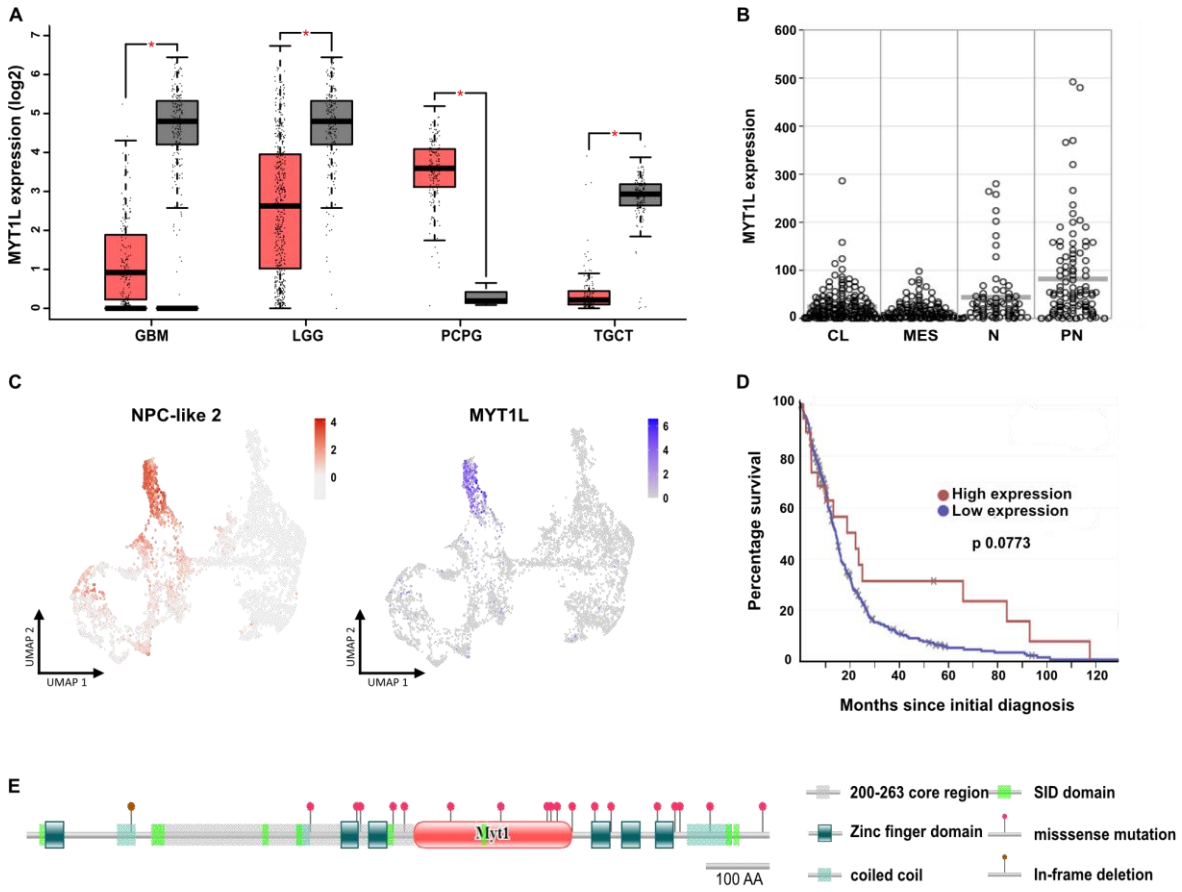

Figure 5: Association of MYT1L with GBM and GBM subtypes

(A) Expression of MYT1L versus normal tissue across cancer. MYT1L expression was significantly decreased in GBM, Low-grade gliomas (LGG) and testicular germ cell tumor (TGCT), while it was significantly increased in Pheochromocytoma and paraganglioma (PCPG). GBM: n(tumors)=163; n(normal)=207; LGG: n(tumors)=518; n(normal)=207; PCPG: n(tumors)=182; n(normal)=3; TGCT: n(tumors)=137; n(normal)=165; Analyses and images from GEPIA. *p>0.001. (B) Expression of MYT1L in Verhaak subgroups. MYT1L is expressed the highest in the proneural (PN) subgroup, compared to classical (CL), mesenchymal (MES), neural (N). Difference not significant (two-sided t-test; p=0.0773). Analysis performed by Marcel Kool (DKFZ Heidelberg). (C) MYT1L expression is enriched in neural progenitor cell 2-like (NPC2)-like cell state. Uniform Manifold Approximation and Projection (UMAP) analysis of single cell gene expression shows exclusive expression of MYT1L (blue) in NPC2-like cell populations (red). Data from Neftel et al. (2019), analysed by Bryce Lim. (D) Survival benefits for MYT1L high (red) over low (blue) expressing tumors. Patients with high MYT1L expression showed tendency to better survival, however changes were not significant. Low-rank (Mantel-Cox) test. Analysis performed with the online tool BETASTASIS. (E) Mutations in MYT1L found in brain cancers listed in ICGC, GDC, cBioPortal and COSMIC databases. SID = Sin3 - interaction domain; aa200-623 core region of MYT1L required for its proneuronal function during reprogramming (Mall et al., 2017). Analysis and figure courtesy of Felix Schüssler.

Based on the potential tumor-suppressor function of MYT1L, I investigated whether accumulation of *MYT1L* mutations occurred in brain cancer patients. Only few MYT1L mutations could be found in the ICGC dataset. The highest frequencies of mutations could be observed in pediatric brain tumors, while only a fraction of GBM and LGG samples showed MYT1L mutations. By using the

online tool TumorPortal, MYT1L could not be identified as significantly mutated in gliomas or any other cancer (Lawrence et al. 2014) (Supp. Fig. 1B). Next, I analyzed whether specific mutations might still be relevant for the role of MYT1L in glioma patients. All protein coding mutations in brain cancer found in the databases were mapped to the corresponding protein sequence of MYT1L (Fig. 5E). No striking accumulation around previously-described functional Zinc finger domains or other specific region of the protein could be observed, and no frameshift mutation of MYT1L could be observed.

4.2 Dedifferentiated mature neurons as potential origin of GBM

While the hypothesis that neural stem cells of the SVZ are the cell-of-origin of GBM is currently the most accepted one (Alcantara Llaguno et al. 2019; Friedmann-Morvinski et al. 2012), the hypothesis that GBM might arise from mature cells, such as neurons, is highly controversial (Friedmann-Morvinski et al. 2012). The concerns about this hypothesis are mainly based on technically insufficient studies, which are missing proof that post-mitotic cells can induce tumor formation. To date, it remains debatable whether mature neurons can be the origin of GBM. Therefore, I aimed to answer the question if loss of MYT1L *in vivo,* alongside with tumor suppressor mutations, results in loss of lineage commitment of fully-differentiated neurons, reacquisition of stem cell features, and potentially tumor formation.

4.2.1 Spatially-restricted depletion of MYT1L in neurons

Initially, an experimental setup was used to examine tumor formation depending on MYT1L, as well as depletion of the tumor suppressor PTEN and TP53, in distinct local cell populations *in vivo*. The modification of these genes in the mouse brain was attained in a spatial- and temporal-specific manner by targeted injection of an adeno-associated virus (AAV) encoding a green fluorescent protein-Cre recombinase (GFP-Cre) fusion protein.

First, I tested whether PTEN, TP53 and MYT1L could be successfully deleted upon AAV-mediated Cre-recombination. Therefore, I generated primary hippocampal cultures from *Myt1l*^{flox} and *Pten*^{flox}*Tp53*^{flox} pups (postnatal day 0; P0) and transduced them with AAV-CAG-GFP-Cre or the corresponding control AAV-CAG-GFP-ΔCre, with a mutated, non-functional Cre-sequence ΔCre, under control of the ubiquitous promoter CAG. To test MYT1L deletion, I performed immunofluorescence stainings in *Myt1l*^{flox} primary cultures transduced with AAV-CAG-Cre-GFP and AAV-CAG-GFP-ΔCre. MYT1L was still present in neurons of the ΔCre condition, but successfully depleted upon Cre-recombination (Fig. 6A). Depletion of PTEN was also confirmed by immunofluorescence staining of primary hippocampal cultures generated as described above. The ΔCre-transduced condition clearly showed PTEN-positive cells, whereas in the Cre-transduced

condition almost no PTEN signal was detectable. (Fig. 6B). Depletion of *Tp53* was confirmed by genotyping PCR of extracted genomic DNA derived from AAV-CAG-GFP-Cre/ΔCre-transduced hippocampal cultures. In the Cre-condition, a PCR product specific for the recombined allele was present at a height of 612bp (Δflox), while it was absent in the ΔCre condition (Fig. 6C). Taken together, all targeted genes could be successfully depleted in a conditional manner *in vitro* using the AAV-mediated Cre-recombination.

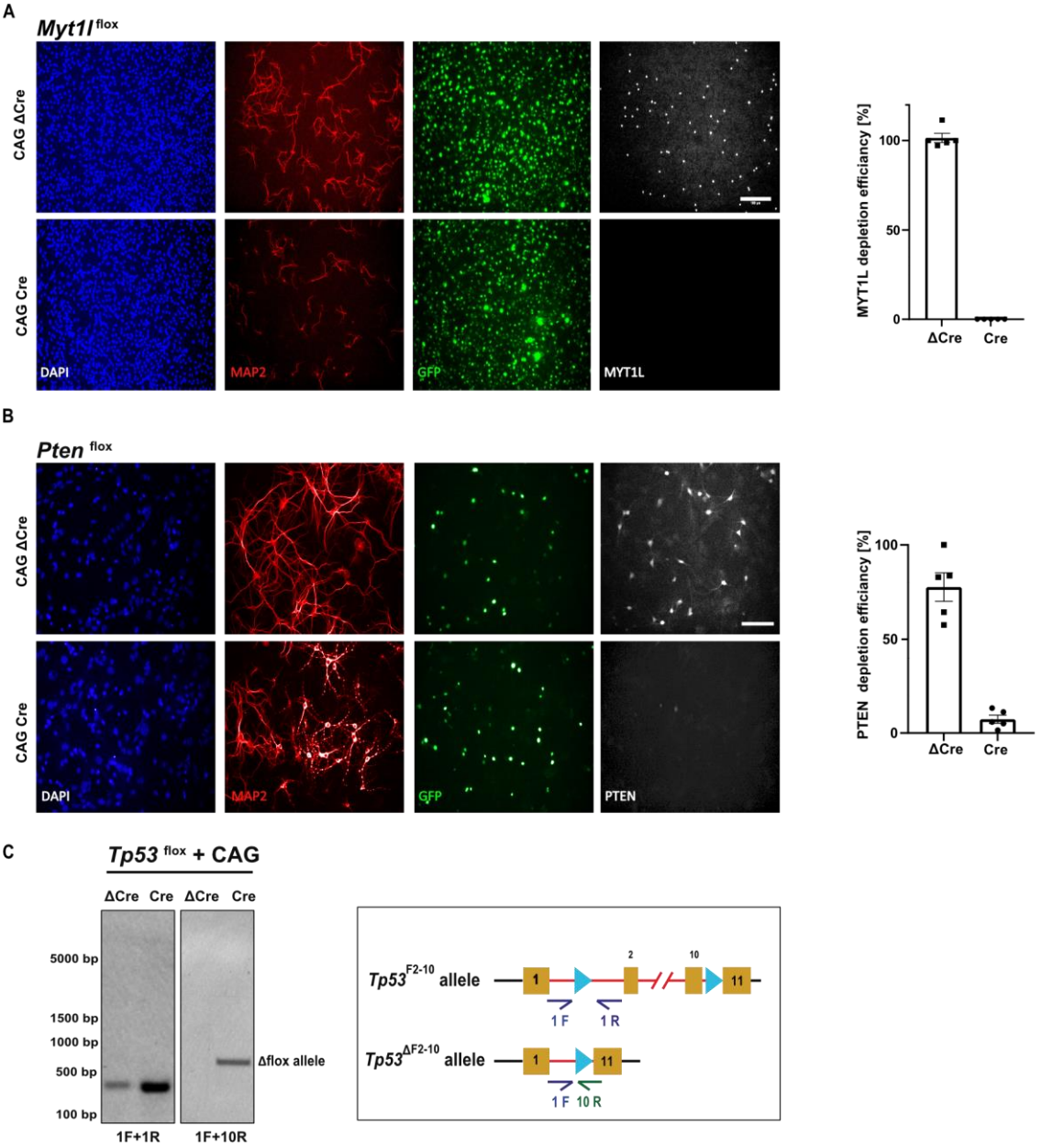

Figure 6: *In vitro* validation of the depletion of MYT1L, PTEN and TP53

(A) Primary hippocampal culture obtained from conditional *Myt1l*^{flox} mice, in which exons 11 and 12 are flanked with loxP sites, was infected at day 3 with AAV-CAG-GFP-Cre or AAV-CAG-GFP-ΔCre. Left: IF staining of fixed cells at day 7 after infection showed successful MYT1L depletion upon transduction with AAV-CAG-Cre. Scale bar 100µm. Right: Quantification of MYT1L deletion efficiency by AAV-Cre/ΔCre treatment; normalized to AAV transduction efficiency (no. of GFP+ cell vs Dapi+ cells); Quantification of 5 ROIs. Bar graph represents mean values, error bars = SD. (B) Confirmation of reduction of PTEN protein expression levels in primary hippocampal cultures obtained from *Pten*^{flox} *Tp53*^{flox} mice after treatment with AAV-CAG-GFP-Cre. Left: IF showed PTEN depletion upon transduction with AAV-CAG-Cre. Right: Quantification of PTEN deletion efficiency; normalized to AAV transduction efficiency (no. of GFP+ cell vs Dapi+ cells); Quantification of 5 ROIs. Bar graph represents mean values, error bars = SD. Scale bar 40 µm. (C) Primary hippocampal cultures of *Pten*^{flox} *Tp53*^{flox} mice treated as in (A) and (B) Genotyping PCR of isolated genomic DNA. Schematic outline shows PCR strategy: Primer pair 1F/1R target 5' loxP site (blue triangle) resulting in a PCR product at a height of 370 bp in both ΔCre and Cre treated cells. Primer pair 1F/10R creates PCR product of 612 bp upon depletion of exons 2-10 (orange boxes). Successful recombination and depletion of Tp53 treated with AAV-CAG-Cre was confirmed by the Δflox band at a height of 612 bp.

Next, direct intracranial injection of AAV-GFP-Cre/ΔCre was performed in *Myt1l*^{flox} (*M*), *Pten*^{flox}*Tp53*^{flox} (*PP*) and *Pten*^{flox}*Tp53*^{flox} *Myt1l*^{flox} (*PPM*) mice (Fig. 7A). To deliver the Cre recombinase in a cell type specific manner, under control of the neuron-specific synapsin (Syn) promoter, using AAV-Syn-GFP-Cre/ΔCre. I performed injections into 1 month old mice successfully targeting either the sub ventricular zone (SVZ) or the cortex region (Fig. 7B,C).

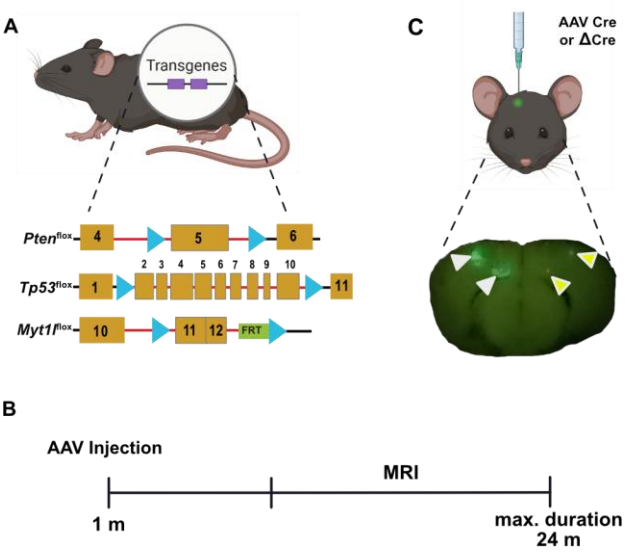

Figure 7: Schematic overview and outline of AAV intracranial injection
(A) Cartoon of targeted mouse transgene alleles *Pten*, *Tp53* and *Myt1l*. Exons (orange boxes); loxP sites (blue triangles) and FRT sequence element (green) are shown. For the *Pten* allele exon 5 is flanked by loxP sites; for *Tp53* allele, exons 2-10 are flanked by loxP sites. For *Myt1l* exons 11 and 12 are flanked by loxP sites. (B) Timeline of intracranial adeno-associated virus (AAV) Cre/ AAV ΔCre injection and analyses. (C) Injection of GFP-labelled AAV into the cortex or subventricular zone (SVZ) of mice. Brain slice was prepared 2 weeks after injection. Left side: 500 nl AAV injection into cortex and SVZ (indicated by white arrows). Right side: 100 nl AAV injection into cortex and SVZ (indicated by yellow arrows).

4.2.2 Spatially-restricted depletion of MYT1L in mature neurons induced tumor formation

To determine whether temporal and spatial MYT1L depletion in mature neurons could induce brain cancer formation, I performed intercranial AAV-Syn-GFP-Cre/ΔCre injection in *Myt1l*^{flox} (*M*), *Pten*^{flox}*Tp53*^{flox} (*PP*), and *Pten*^{flox}*Tp53*^{flox} *Myt1l*^{flox} (*PPM*) mice. Targeting the synapsin promoter allowed me to deplete genes specifically in mature neurons.

AAV injection into the cortex of *M* mice did not show an effect on survival and did not result in tumor formation (Fig. 8A). Remarkably, AAV-Syn-GFP-Cre injection in *PP* and *PPM* mice affected the survival of the animals. The median survival of *PP* mice was 440 days, while the median survival of *PPM* mice was reduced by over 100 days (median survival 335 days) (Fig. 8A). In both groups, the majority of mice had to be released from the experiment due to tumor development. Tumors could be detected in 61.1% of all AAV-Syn-GFP-Cre injected *PP* mice. AAV-Syn-GFP-Cre injection in *PPM* mice also resulted in tumor formation detected in 66.7% of the animals (Fig. 8B). MRI brain scans of *PP* and *PPM* mice were performed regularly, and tumors could be detected at the local injection site in the cortex region (Fig. 8C). In contrast, the survival of the three respective control groups,

injected with the ΔAAV-Syn-GFP-ΔCre, was not affected and I detected no tumors in these groups (Fig. 8A).

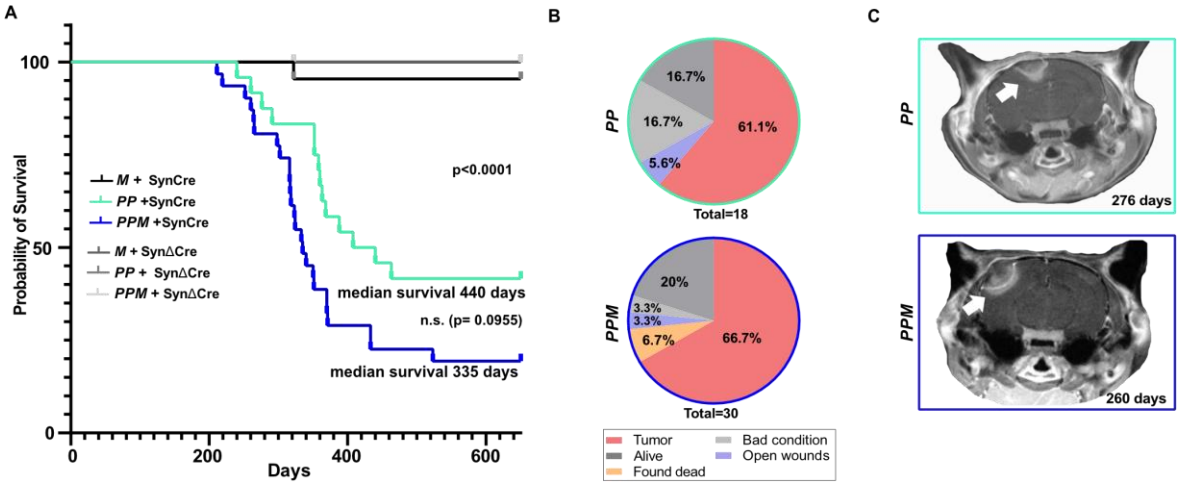

Figure 8: AAV-mediated local destabilization of neuronal fate in neurons of the mouse cortex.
(A) Kaplan-Meier survival curves of AAV-Syn-GFP-Cre (SynCre) and AAV-Syn-GFP-ΔCre (SynΔCre) injected mouse lines *Myt1l* flox (*M*), *Pten Tp53* flox (*PP*) and *Pten Tp53 Myt1l* flox (*PPM*). Median survival in *PPM* mice was shorter (335 days) compared to *PP* mice (440 days). Survival differences between *M* and *PP/PPM* significant (****p<0.0001) but not significant between *PP* and *PPM* (p=0.0955); low-rank (Mantel-Cox) tests. (B) Pie charts showing causes of death (as a percentage of AAV Syn Cre treated animals) in *PP* and *PPM* mice. In both groups, the majority of mice had to be released from the experiment due to tumor development, with 61.1% and 66.7%, respectively. (C) Two representative MRI scans of *PP* and *PPM* mice. MRI scans show tumor formation (indicated by white arrow) detected after 276 days and 260 days.

In order to investigate the effects of the neuron-specific local depletions of MYT1L, PTEN and TP53 on gene expression, I isolated nuclei from infected, GFP-positive cells, from mouse brain tissue 8 weeks after AAV injection. GFP-positive nuclei were sorted by Fluorescence Activated Cell Sorting (FACS) and bulk RNA sequencing was performed (Fig. 9A).

In nuclei isolated from *M* mice injected with AAV-Syn-GFP-Cre, *Myt1l* expression was significantly decreased in infected cells. In the nuclei isolated from cortices of the *PP* mice, normalized RNA counts for the targeted tumor suppressor *Pten* were decreased compared to ΔCre control while there was no significant change in *Tp53* counts. RNA-bulk data from isolated nuclei of infected cortices of *PPM* mice showed a tendency towards decreased counts for *Myt1l,* but *Pten* and *Tp53* appeared not to be altered compared to control (Supp. Fig. 2).

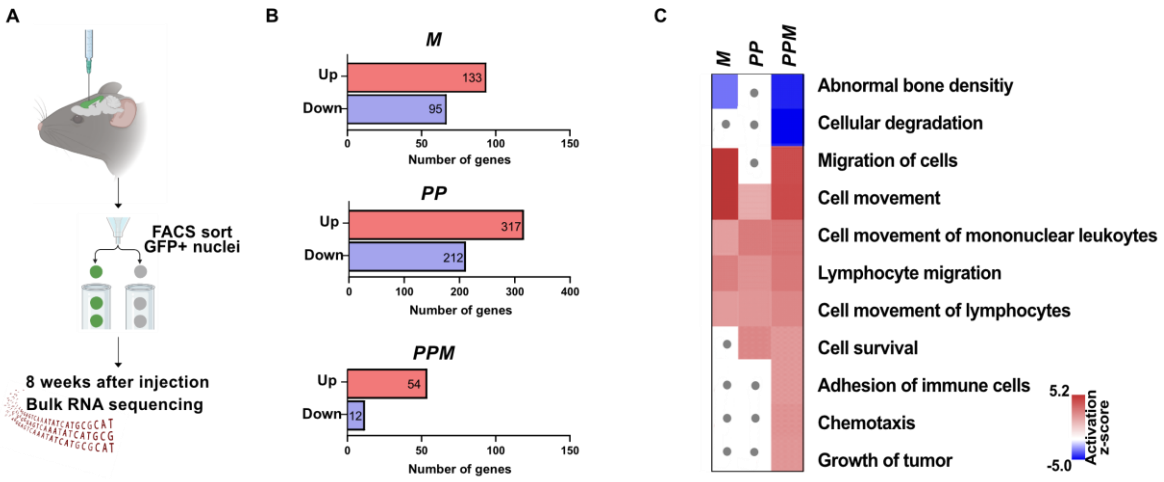

Figure 9: Gene expression changes after AAV-mediated local destabilization of neuronal fate in neurons of the mouse cortex

(A) Cartoon of intracranial injection of GFP-labelled AAV Syn Cre and ΔCre. 8 weeks after injection, GFP positive tissue was dissected, nuclei were isolated and bulk RNA-sequencing was performed of FACS-sorted GFP-positive nuclei. (B) Number of differentially expressed (DE) genes upregulated (Up) and downregulated (Down) in *Myt1l* flox (*M*), *Pten Tp53* flox (*PP*) and *Pten Tp53 Myt1l* flox (*PPM*) mice treated with AAV Syn Cre. In all three models more DE genes appeared to be upregulated upon depletion of indicated genes. (Exact numbers indicted in the bars) (C) Ingenuity Pathway Analysis (IPA) comparison of canonical pathways up- and downregulated in the three models. Most overlaps could be observed between the *M* and *PPM* mice. Blue: downregulated pathways, red: upregulated pathways; z-score scale ranges from -5.0 to 5.2. n(M+SynCre)=2; n(M+SynΔCre)=2; n(PP+SynCre)=3; n(PP+SynΔCre)=3; n(PPM+SynCre)=4; n(PPM+SynΔCre)=2.

Overall, in all three groups, more differentially expressed (DE) genes were upregulated than downregulated (Fig. 9B). Comparison of IPA canonical pathways between the three groups showed pathways related to cell movement and immune cell migration upregulated (Fig. 9C). Interestingly, in *PPM* mice, the pathway related to tumor growth was upregulated, suggesting that this model had the strongest correlation with tumor formation and progression. The largest overlap in IPA pathways could be observed between the *M* and the *PPM* mice.

Together, these results show the intracranial AAV-Syn-Cre injection resulted in tumor formation in *PP* and *PPM* mice, while the additional depletion of MYT1L in the latter mice accelerated tumor formation. In addition, gene expression analysis of isolated GFP-positive nuclei revealed upregulation of tumor growth related pathways in *PPM* mice.

4.2.3 Generation and validation of genetic mouse tumor model for lineage-restricted gene deletion

Given the observed tumor development in *PP* and *PPM* mice upon temporal and spatial neuron-restricted AAV-based gene depletion, I next decided to utilize a genetically-engineered mouse model to further consolidate this finding. I generated mouse models with lineage-restricted *Myt1l*

and tumor suppressor *Pten* and *Tp53* genetic deletions. For this, I used lineage-specific, tamoxifen-inducible Cre-lines to either target neural progenitors (Nestin-creER^{T2}) or post-mitotic neurons (CamK2a-creER^{T2}). Published data has shown that premalignant neural progenitor cells derived from *Tp53*$^{-/-}$ *Pten*$^{+/-}$ GFAP-Cre mice induced tumor formation (Hu et al. 2013). Therefore, I predicted that deletion of *Pten* and *Tp53* in neuronal progenitors would generate a high-grade malignant glioma that might be even more aggressive in combination with MYT1L loss.
Based on previous work, homozygous deletion of *Tp53* and *Nf1* in combination with heterozygous depletion of *Pten* in post-mitotic neurons did not result in tumor formation (Alcantara Llaguno et al. 2019). By performing homozygous deletion of *Pten* and *Tp53* in the post-mitotic CamK2a-creER^{T2} mouse model, I aimed to investigate whether these previous findings hold true. Moreover, I examined if additional co-depletion of *Myt1l* is sufficient to destabilize neuronal cell fate to trigger tumor formation.

In order to test Cre-mediated recombination in the Nestin-creER^{T2} driven and CamK2a-creER^{T2} driven models, I crossed mice with mT/mG double-fluorescent Cre reporter mice. The mT/mG mice express membrane-targeted tdTomato (mT). After Cre-mediated excision, membrane-targeted green fluorescent protein (mG) is expressed instead of mT (Supp. Fig. 4A). I injected one month old Nestin-CreER^{T2} mT/mG and CamK2a-CreER^{T2} mT/mG mice four days in a row with Tamoxifen (Tam) or Vehicle as a control. The injected mice were harvested two months after injection (Supp. Fig. 4B). Immunofluorescence staining of CamK2a-CreER^{T2} mT/mG (iCK mT/mG) brain sections confirmed successful Cre-mediated recombination. The Tam-injected iCK mT/mG mice expressed GFP in the NeuN-positive cortex region, where CamK2a is expressed in excitatory neurons. Vehicle-injected control mice did not show GFP expression in the cortex (Supp. Fig. 4C). Next, I analyzed brain sections of Nestin-CreER^{T2} mT/mG reporter mice. In adult mouse brain, generation of neurons is limited to only a few areas such as the lateral wall of the lateral ventricle, the rostral migratory stream, dentate gyrus and the olfactory bulbs (Mignone et al. 2004). I could not detect GFP-positive cells in the described brain regions of induced Nestin-driven reporter mice. Hence Cre-recombination in neural progenitor cells could not be verified using the Nestin-CreER^{T2} mT/mG reporter mouse line.

Following successful Cre-recombination in the cortices of iCK mice, I investigated the deletion of tumor suppressors *Pten* and *Tp53*, as well as *Myt1l,* in the generated iCK driven mouse models (Fig. 10A). Therefore, I micro-dissected PFA-fixated tissue of mutants and controls and isolated the genomic DNA. PCR genotyping was performed with primers for *Myt1l*, *Pten* and *Tp53*. I confirmed successful recombination of *Myt1l* and *Tp53*. (Fig. 10B,C; supp. Fig. 3). In iCK *M* mice exons 11 and

12 are flanked by loxP sites. The primers used (M1 and M3) result in a PCR product of 350 bp (Δflox) upon binding DNA sequence in which exons 11 and 12 were excised. Only mice with the Tam-induced excision of exons 11 and 12 showed this product (Fig. 10B). For Vehicle-treated iCK *M* mice, this band was absent. In both, the Tam treated, as well as in the control, I saw an unexpected band at a height of 200 bp.

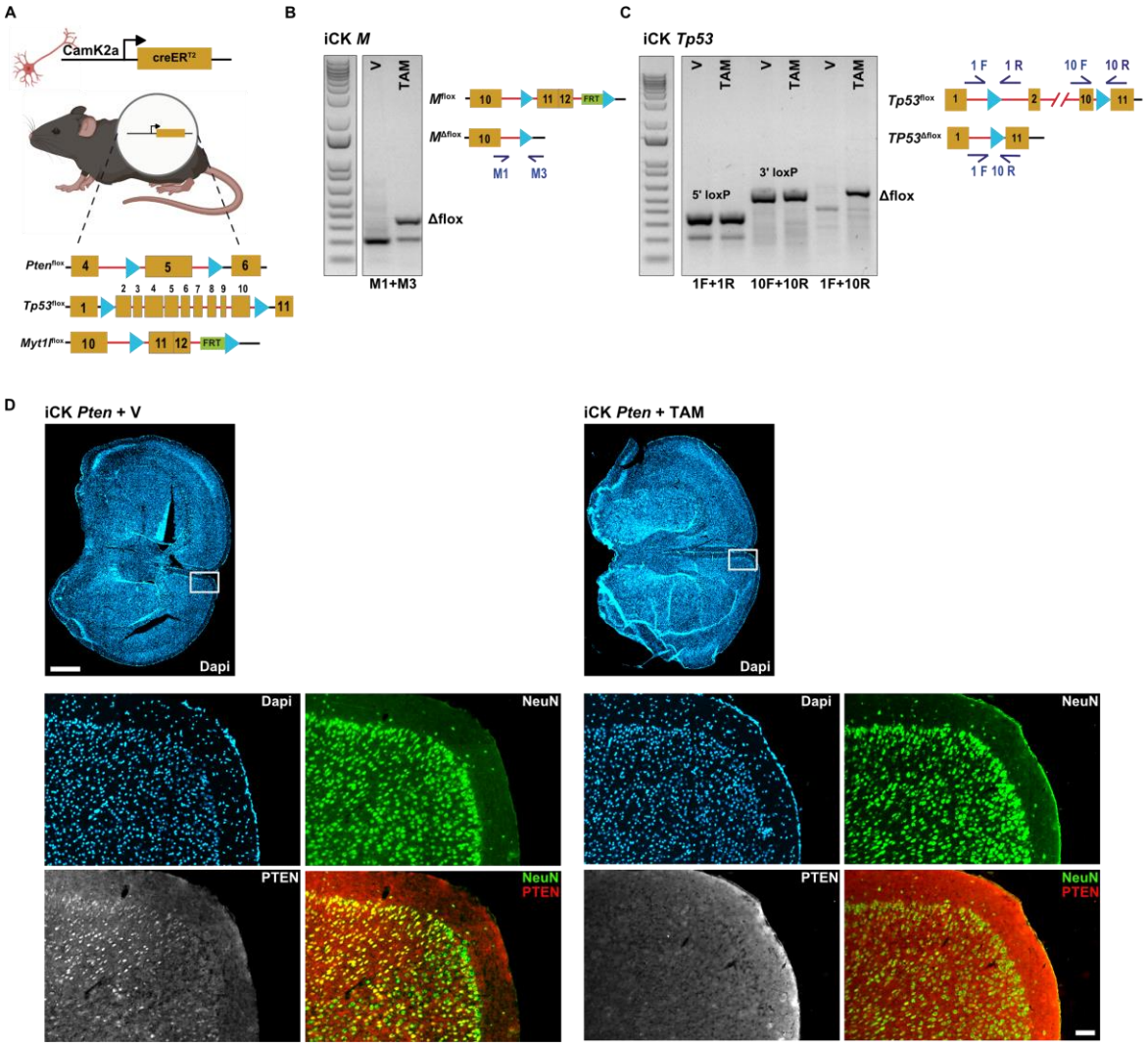

Figure 10: Validation of Camk2a-driven mouse models
(A) Cartoon of Camk2a-creER^{T2} (iCK) and model and targeted mouse transgene alleles *Pten*, *Tp53* and *Myt1l*. Exons (orange boxes; loxP sites (blue triangles) and FRT sequence element (green) are shown. For the *Pten* allele exon 5 is flanked by loxP sites; for *Tp53* allele exons 2-10 are flanked by loxP sites. For *Myt1l* exon 11 and 12 are flanked by loxP site. (B and C) Genotyping PCRs for recombined alleles on genomic DNA isolated from microdissected cortex regions of iCK *Myt1l* flox *(M)* and iCK *Tp53* flox mice. (B) Genotyping PCR for recombined (Δflox) alleles of iCK M mice. Schematic outline shows PCR strategy: Primer pair M1/M3 results in a PCR product of 350 bp upon successful recombination and excision of exons 11 and 12 (orange boxes). For Vehicle (V) treated iCK M mice this band was absent, while it was present in Tamoxifen (TAM) injected animals. (C) Genotyping PCR for recombined (Δflox) alleles as well as detection of 5' and 3' loxP sites (blue triangle) of iCK *Tp53* flox mice. Schematic outline shows PCR strategy: Primer pair 1F/1R targets 5' loxP site resulting in a PCR product at a height of 370 bp. Primer pair 10F/10R targets 3' loxP site resulting in a PCR product at a height of 514 bp. In both V and TAM injected animals these bands were present. Primer pair 1F/10R only binds after successful excision of exons 2-10 (orange boxes). Successful excision was confirmed by the Δflox band at a height of 612 bp (Δflox) only present in TAM injected mice. (D) Immunofluorescence staining brain sections of iCK *Pten Tp53* flox mice injected with Vehicle (V; left) or Tamoxifen (TAM; right) harvested 4 weeks after injection. PTEN signal was present in control animals and deleted of TAM treated animals. Scale bar 1000 µm and 200 µm.

In mice with floxed *Tp53* allele, the deletion of exons 2-10 was confirmed by a PCR product that appeared at 612 bp (Δflox). The loxP sites at the 5'end and the 3'end could be detected in both untreated and treated mice at a height of 370bp and 514 bp, respectively (Fig. 10C). For the *Pten* allele, exon 5 is flanked by loxP sites and induction with Tam should lead to excision of exon 5 resulting in a band that should appear at a height of 300 bp. However, this PCR product could not be detected despite several attempts of primer optimization and PCR conditions. Hence, I performed immunofluorescence staining of PTEN in brain sections of those mice. Here, I observed a successful depletion of PTEN in the mouse cortex upon Tam injection (Fig. 10D). Taken together, I showed that all three targeted genes could be successfully depleted *in vivo* in the genetically engineered mouse model.

4.2.4 Destabilization of neuronal cell fate upon MYT1L depletion in mature neurons

After validation of the generated of CamK2a-creER^{T2} (iCK) driven mice for *Myt1l (M)* and tumor suppressor (*Pten* and *Tp53, (PP)*) deletions, I aimed to determine whether targeting mature neurons could potentially induce tumor formation. Moreover, this experiment was intended to show whether the additional MYT1L loss could destabilize neuronal fate and potentially enhance tumor formation originating from postmitotic excitatory neurons (Fig. 11A). For this experiment, mice were injected with Tam or vehicle at the age of 4 weeks (Fig. 11B). The survival of mice with depletion of only MYT1L was not affected (Fig. 11C). Homozygous depletion of *Pten* and *Tp53* in one month-old mice led to an unexpected, early death with an overall median survival of 107.5 days (Fig. 11C). Control cohorts injected with vehicle did not show any phenotype. Surprisingly, 20% of the induced iCK *PP* mice developed brain tumors which I detected by MRI measurement (Fig. 11D). The earliest tumor was detected at 178 days, and the latest tumor at 405 days, after Tam injection.

Remarkably, additional co-depletion of *Myt1l* in the iCK *PPM* model resulted in significantly enhanced lethality, with a median survival of only 44.5 days (Fig. 11C). A large proportion of the mice died suddenly without any prior signs and abnormalities or detectable tumor formation (Fig. 11D).

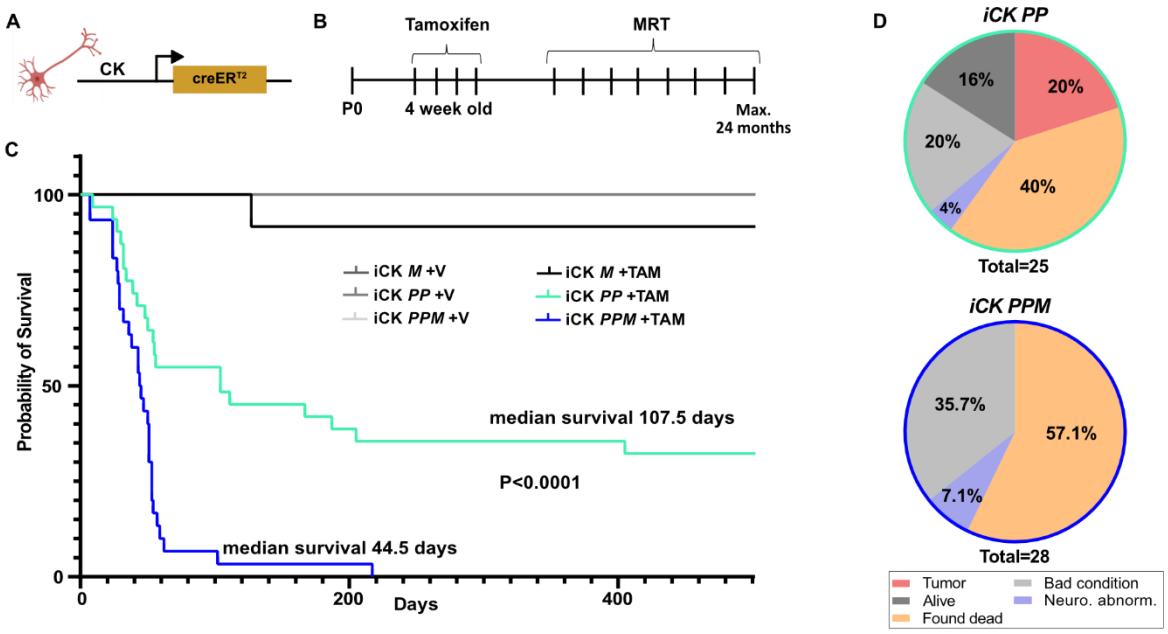

Figure 11: Destabilization of neuronal fate in post-mitotic neurons resulted in high lethality of mice
(A) Cartoon of Camk2a-creER^{T2} (CK) driven mouse model. (B) Timeline of Tamoxifen (TAM)/Vehicle (V) injection and analyses. (C) Kaplan-Meier curves for TAM and V treated in CamK2aCreER^{T2} *Myt1l* flox (iCK *M*), *Pten Tp53 flox* (iCK *PP*) and *Pten Tp53 Myt1l* flox (iCK *PPM*) mice. TAM treated iCK *PP* mice had a median survival of 107.5 days and TAM treated iCK *PPM* mice had a median survival of 44.5 days. P<0.0001; low-rank (Mantel-Cox) test. (D) Pie charts showing causes of death (in percent of all TAM treated animals) in iCK *PP* and iCK *PPM* mice. In iCK PP model, 20% of the mice developed tumors. In the iCK *PPM* model, 57.1% of the treated mice were found dead.

I further characterized two out of the five observed tumors of the iCK *PP* model by immunohistology together with Maria-Luisa Wiesinger (supervised master student, DKFZ Heidelberg).

One of the detected brain tumors showed sharp tumor borders in the MRI scan at day 205 after injection of Tam. Brain sections were obtained from the harvested and fixed tumor bearing mouse. Nissl staining clearly identified the apparent tumor characterized by high cell density, pleomorphic cells, and apparent mitotic figures (Fig. 12). The tumor was highly Nestin-, OLIG2-, and GFAP-positive with a sharp tumor border. Based on positive staining for Ki67 and BrdU, the tumor showed a high proliferative capacity. Ionized calcium-binding adapter molecule 1 (IBA1), which marks activated microglia, could also be detected within the tumor. Additionally, NeuN was completely absent within the tumor and was only expressed in the surrounding, normal tissue.

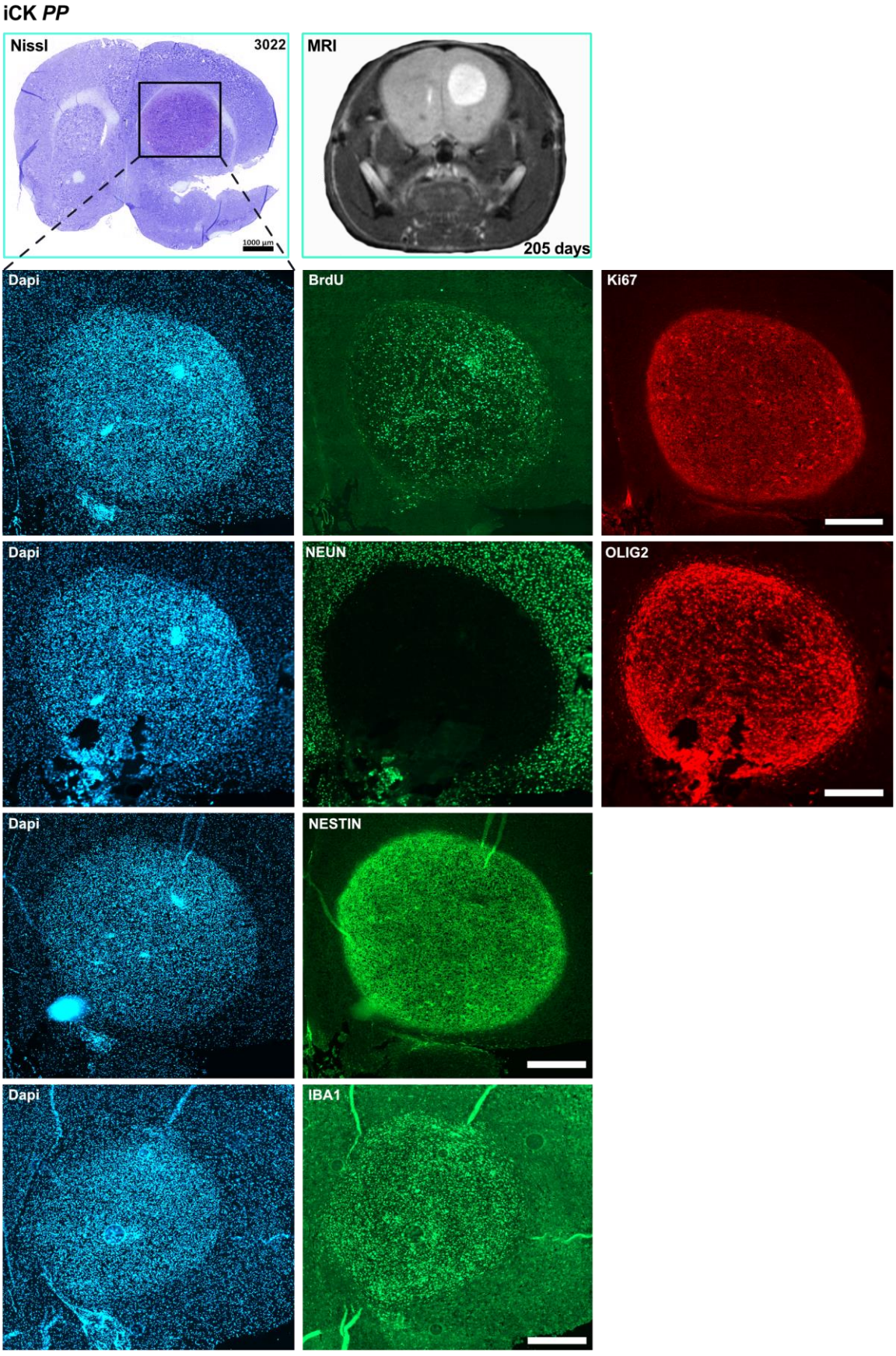
iCK *PP*
Nissl
3022
1000 µm
MRI
205 days
Dapi
BrdU
Ki67
Dapi
NEUN
OLIG2
Dapi
NESTIN
Dapi
IBA1

Figure 12: Tumor suppressor loss in iCK mice resulted in tumor formation (1)
(A) Tamoxifen treated Camk2a-creER^{T2} *Pten Tp53* flox mice (iCK *PP*) showed tumor formation. Shown are brain sections of a tumor from mouse 3022. Tumor formation was detected by MRI scan at day 205. Nissl staining of brain section showed distinct tumor with high cell density (indicated by black box). Immunofluorescent staining for several markers was performed for the tumor area. Scale bars 1000 µm and 500 µm.

A second detected tumor showed more infiltrative capacity (Fig. 13). OLIG2- and GFAP-positive cells were most abundant at the tumor border and the infiltrated surrounding tissue up to the opposite hemisphere. The tumor showed a high proliferative capacity based on positive staining for Ki67. The inner tumor region was mostly phosho-S6 (pS6)-negative, while in the outer region and the close surrounding tissue, pS6-positive cells were present. pS6 is a downstream target of the PI3 kinase and mammalian target of rapamycin (mTOR) pathway and is an indicator for mTOR activation (Chiang and Abraham 2007).

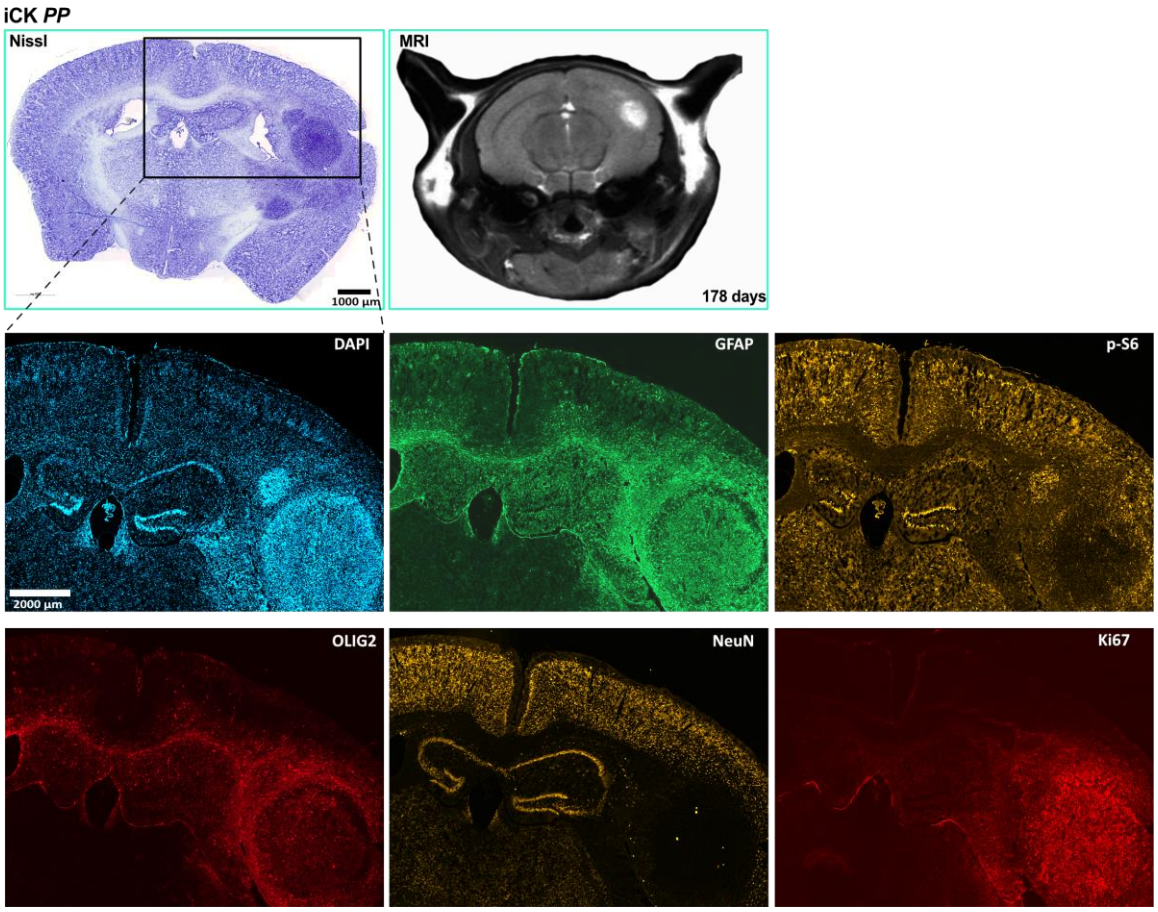

Figure 13: Tumor suppressor loss in iCK mice resulted in tumor formation (2)
(A) Tamoxifen treated Camk2a-creER^{T2} *Pten Tp53* flox mice (iCK *PP*) showed tumor formation. Shown are brain sections of depicted tumor mouse 3038. Tumor formation was detected by MRI scan at day 178. Nissl staining of brain section showed tumor with infiltrative tumor area (indicated by black box). Immunofluorescent staining for several markers was performed for the tumor core including tumor surroundings and parts of the opposite hemisphere. Scale bars 1000 µm and 2000 µm.

Based on the tumor formation in the iCK *PP* model and the striking effects of MYT1L loss in combination with the loss of the tumor suppressors PTEN and TP53 on mouse survival, I further examined whether I could observe gene expression changes that might explain this mechanistically. Therefore, I harvested mice one month after administration of Tam or Vehicle. Bulk RNA sequencing of the prefrontal cortices was performed (Fig. 14A).

In the iCK *M* mice, *Myt1l* expression was significantly decreased in the mouse cortex (Supp. Fig. 5). In the cortices of iCK *PP* mice, the normalized counts for the targeted tumor suppressor *Pten* tended to be reduced while there was no significant change in *Tp53* counts. RNA-bulk data from cortices of CamK2aCreER^{T2}*Pten*$^{-/-}$*Tp53*$^{-/-}$*Myt1l*$^{-/-}$ mice did not show changes in normalized counts for *Pten* or *Tp53*, but a significant downregulation was observed for *Myt1l* counts.

In the iCK *M* model, more DE genes appeared to be upregulated than downregulated (Fig. 14B). By performing Ingenuity Pathway Analysis (IPA), I found pathways related to transcriptional regulation and pathways related to cellular stress, diseases, and cancer downregulated and upregulated, respectively. Further Gene Ontology (GO) analysis revealed the upregulation of non-neuronal biological processes such as blood vessel development, heart development, and cardiac muscle cell contraction. As expected, GO terms related to neuronal development, organization, and differentiation were downregulated upon the loss of MYT1L (Supp. Fig. 6A) These results demonstrated the important role of MYT1L in the regulation of neuronal differentiation and indicated that neuronal fate is destabilized upon loss of MYT1L.

The iCK-driven depletion of *PP* mice resulted in more downregulated than upregulated DE genes (Fig. 14C). Consequently, IPA analysis revealed that most of the canonical pathways were downregulated, such as neurotransmitter signaling, growth factor signaling and organismal growth and development. GO analysis showed the downregulation of important regulatory processes, such as metabolic, biosynthetic, and cellular processes. (Supp. Fig. 6B). In those mice with homozygous depletion of *Pten* and *Tp53* in post-mitotic neurons, I found *Gfap* and *Akt-1* under the top upregulated DE genes, while *PI3K* was among the top downregulated DE genes (Supp. Fig. 6E).

As in the iCK *M* model, more DE genes were upregulated than downregulated for the iCK *PPM* model (Fig. 14D). More similarities between the two models could also be found with IPA canonical pathway analysis. Here, pathways related to transcriptional regulation were downregulated, while pathways connected to cardiovascular signaling, disease-specific pathways, cellular stress, cellular immune response, and cancer were upregulated. Further GO analysis showed the downregulation of biological processes linked to neuronal development and differentiation, such as development of the central nervous system, neuron differentiation, and generation of neurons. Interestingly, cell

death was found among the top upregulated GO terms (Supp. Fig. 6C). In mice with depletion of tumor suppressors and MYT1L, as well as with MYT1L depletion alone, the gene *Tead2*, a marker for dedifferentiation, was one of the most strongly upregulated DE genes (Caldwell et al.) (Supp. Fig. 6D,F). In general, most overlapping DE genes could be detected between iCK *M* mice and iCK *PPM* mice (Fig.14 E,F). This is in line with the similarity between these two groups in IPA and GO term analysis.

Together, these findings show that depletion of the tumor suppressors PTEN and TP53 in iCK promoter-driven mice can induce tumor formation and PTEN and the additional depletion in combination with these tumor suppressor deletions, resulted in sudden death of mice. Loss of MYT1L in iCK *M* mice led to downregulated expression of neuronal genes and cancer related pathways were highly upregulated in iCK *PPM* mice.

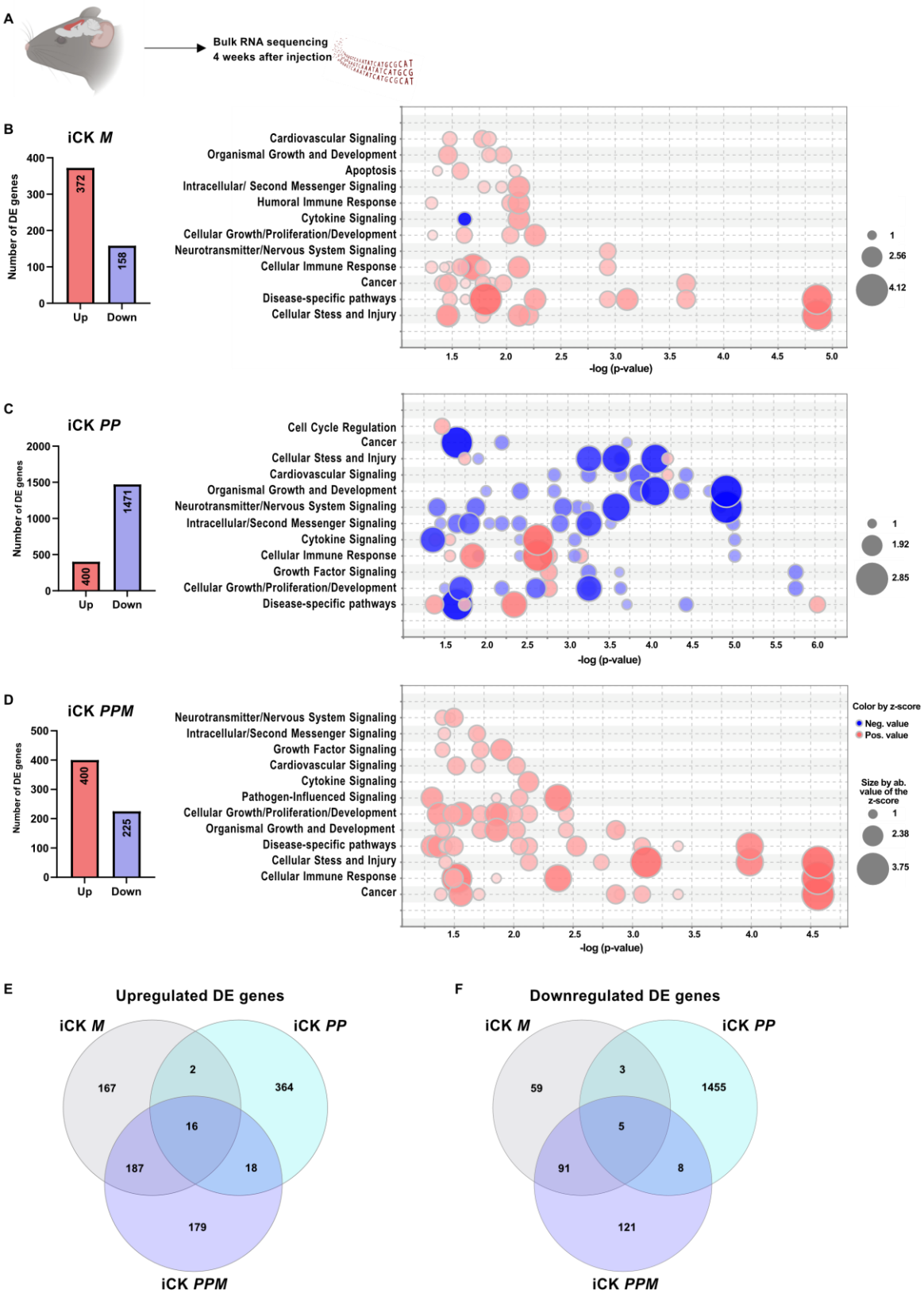
A
Bulk RNA sequencing
4 weeks after injection
B
iCK M
Number of DE genes
372
158
Up
Down
Cardiovascular Signaling
Organismal Growth and Development
Apoptosis
Intracellular/ Second Messenger Signaling
Humoral Immune Response
Cytokine Signaling
Cellular Growth/Proliferation/Development
Neurotransmitter/Nervous System Signaling
Cellular Immune Response
Cancer
Disease-specific pathways
Cellular Stess and Injury
-log (p-value)
C
iCK PP
400
1471
Cell Cycle Regulation
Cancer
Cellular Stess and Injury
Cardiovascular Signaling
Organismal Growth and Development
Neurotransmitter/Nervous System Signaling
Intracellular/Second Messenger Signaling
Cytokine Signaling
Cellular Immune Response
Growth Factor Signaling
Cellular Growth/Proliferation/Development
Disease-specific pathways
D
iCK PPM
400
225
Neurotransmitter/Nervous System Signaling
Intracellular/Second Messenger Signaling
Growth Factor Signaling
Cardiovascular Signaling
Cytokine Signaling
Pathogen-Influenced Signaling
Cellular Growth/Proliferation/Development
Organismal Growth and Development
Disease-specific pathways
Cellular Stess and Injury
Cellular Immune Response
Cancer
Color by z-score
Neg. value
Pos. value
Size by ab. value of the z-score
E
Upregulated DE genes
iCK M
iCK PP
iCK PPM
167
2
364
16
187
18
179
F
Downregulated DE genes
iCK M
iCK PP
iCK PPM
59
3
1455
5
91
8
121

Figure 14: Gene expression analysis of iCK mouse model
(A) Bulk RNA-sequencing was performed on cells isolated from the prefrontal cortex 4 weeks after injection of CamK2aCreER^{T2} *Myt1l* flox (iCK *M*), *Pten Tp53 flox* (iCK *PP*), and *Pten Tp53 Myt1l* flox (iCK *PPM*) mice. (B-D) Left: Number of differentially expressed (DE) genes upregulated (Up) and downregulated (Down) in Tamoxifen induced iCK *M*, iCK *PP* and iCK *PPM* mice. While in iCK *M* and iCK *PPM* mice, more genes were upregulated than downregulated, the opposite was observed in the iCK *PP* model. Right: Ingenuity Pathway Analysis (IPA) of canonical pathways for each mouse model plotted as pathway name vs. p-value(-log). Colors indicate z-score. (E+F) Overlapping upregulated and downregulated DE genes between the three models. n(iCK *M* + TAM)= 4; n(iCK *M* + V)= 3 ; n(iCK *PP* +TAM)=2; n(iCK *PP* +V)=3; n(*PPM* +TAM)=3; n(*PPM* +V)=3.

4.2.5 Depletion of MYT1L in progenitor cells

Based on previous publications, mice of the Nestin-CreER^{T2} model, targeting progenitor cells and inducing tumor suppressor inactivation of *Pten, Tp53,* and *Nf1* should generate high-grade malignant glioma phenotypes with notable clinical pathological and molecular resemblance to primary GBM in humans (Alcantara Llaguno et al. 2019; Zhu et al. 2014). Therefore, I expected similar results in the generated Nestin-CreER^{T2}*Pten*^{flox} *Tp53*^{flox} mouse model (Supp. Fig. 7A). However, no phenotype related to gliomagenesis could be observed. No abnormalities were found on the MRI and in the overall survival up to the timepoint of 600 days after Tam injection (Supp. Fig. 7C). In all three Tam induced groups, as well as in the control groups, dying of mice began to increase with higher age between 400 and 600 days. Causes of death were related to bad general health conditions, open wounds, and other reasons such as dental problems or eye problems. These causes of death could not be linked to neurological phenotypes or brain tumor formation. It must be noted that the successful Cre-recombination in the Nestin-driven mouse model could not be shown in mT/mG reporter mice. This may explain the absence of expected tumor formation upon targeting progenitor cells.

4.3 MYT1L – a potential tumor suppressor

Alongside with dedifferentiation, blocked differentiation represents another process of the cancer hallmark *Unlocking Phenotypic Plasticity*. In this case, progenitor cells are blocked from differentiation into a non-proliferative, mature state. Previously, MYT1L has been shown to enhance neuronal differentiation by repressing non-neuronal gene programs and inhibiting developmental tumor-promoting pathways, including Wnt, Notch, and Hedgehog signaling (Mall et al., 2017). In the following chapters, I examined whether the loss of MYT1L in an early developmental state could block differentiation and potentially promote tumor formation using a humanized brain tumor organoid model. Considering previous findings, where loss of MYT1L in NSCs resulted in tumor formation *in vivo* (Hu et al. 2013), I also aimed to address the question whether MYT1L could function as a tumor suppressor. For these purposes patient-derived glioma cell lines (PDGCs) were utilized.

4.3.1 Establishing a cerebral organoid protocol

Human cortical organoids have been found to recapitulate key steps of brain development and represent aspects of human brain histology and physiology (Lancaster et al. 2013). Therefore, they provide unique opportunities for the study of brain related diseases and complement animal models as well as 2D cell culture models (Kim et al. 2020). For that reason, I established a robust protocol for the generation of cerebral organoids from iPSCs and ES cells based on published organoid protocols (Fig. 15A) (Krefft et al. 2018; Lancaster and Knoblich 2014). These organoids were later utilized to generate a 3D *in vitro* brain tumor model. Therefore, the most important requirements were a high grade of reproducibility and homogeneity, as well as a faithful recapitulation of the forebrain region, where glioma driving GSCs have been found originate from (Marques-Torrejon et al. 2018). I tested whether generated organoids based on the two protocols from Krefft et al. and Lancester/Knoblich meet these criteria.

The cerebral organoids were generated from hESCs (H1) or iPSCs (C6). Due to the self-organizing capacity of pluripotent stem cells, they formed embryoid bodies (EBs) the day after seeding (Fig. 15B). As soon as they reached a diameter of around 500 µm, cortical induction medium was added for the induction of neuroectoderm. The cortical induction medium was supplemented with WNT inhibitor and dual SMAD inhibitor which both are essential to promote the forebrain/cortical identity and the typical cyto-architecture with outer sub-ventricular-like regions containing radially-organized, apical cortical rosettes (Rosebrock et al. 2022). At an early stage, around 8 days after seeding, rosette formations in the outer layer could be observed (Fig. 15 B). Rosette formation and structural organization increased during cultivation and after switching to differentiation medium. To compare the two protocols from Krefft et al. and Lancester/Knoblich, I performed a time course

expression analysis of important differentiation and identity markers. I showed that organoids based on the protocol from Krefft had higher expression of both immature (DCX) and mature neurons (MAP2 and MYT1L) after 4 weeks in culture, compared to the differentiation based on Lancester and Knoblich (Fig. 15C). Additionally, the expression of the forebrain identity marker FOXG1 was found to be higher in organoids that were generated with the Krefft protocol (Fig. 15C). Immunohistochemical analysis of organoids derived using the Krefft protocol confirmed the presence of distinct neural tissue with SOX2-postitive neural progenitor cells organized in rosette-like structures after 30 days of cultivation.

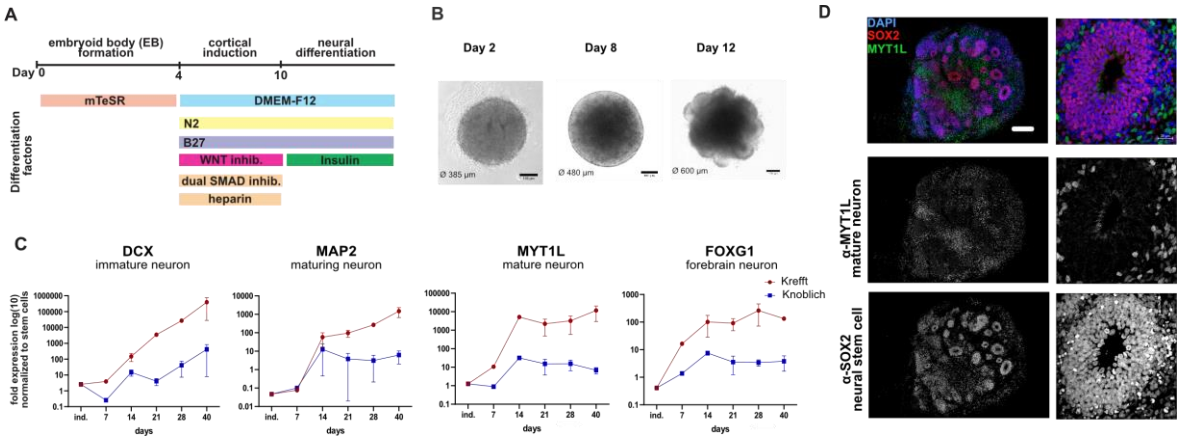

Figure 15: Cerebral organoid protocol validation
(A) Outline of the cerebral organoid protocol used in this project. (B) Brightfield images of cerebral organoids generated based on the protocol of Krefft et al. at indicated days. Scale bar 100 µm. (C) Comparison of two cerebral organoid protocols (Krefft et al. in red and Lancester and Knoblich in blue) by marker gene expression measured by qRT-PCR at indicated time points. (D) Cerebral organoid organization with SOX2+ rosette-like progenitor zones and adjacent MYT1L+ mature neurons at day 30 shown by immunofluorescence. Scale bar 200 µm and 20 µm.

Additionally, mature neurons, marked as MYT1L-positive cells, were present in the organoids after 30 days of cultivation (Fig. 15D). Given these characteristics, the forebrain-type organoids based on the protocol of Krefft et al. fulfilled the required criteria and were further utilized to establish a cerebral organoid model for brain tumor formation and progression.

4.3.2 MYT1L loss promoted proliferation in cerebral organoid brain tumor model

Genetically engineered mouse models (GEMMs) are broadly used for both biological and preclinical investigations in GBM research. Even though mouse models mimic the pathophysiological features of human brain tumors, their application is limited by the time and costs associated with extensive intercrossing of mouse lines (Bian et al. 2018). On the other hand, *in vitro* modelling of GBM remains a highly-challenging task because it is difficult to model the high degree of intra-tumor heterogeneity and the interaction of tumor cells with other cell types. Thus,

2D cultures of human brain cancer cell lines and cancer stem cells do not recapitulate the 3D brain environment (Azzarelli 2020).

Consequently, we need models that accurately capture the cellular composition and developmental dynamics of the human brain. For this purpose, I generated a cerebral organoid tumor model by introducing tumorigenic events by CRISPR/Cas9-mediated deletion of *NF1*, *PTEN,* and *TP53* in the established cerebral organoids (Fig. 16A) (Bian et al. 2018). I selected *NF1, PTEN,* and *TP53* as ideal genetic targets for mutagenesis since they are the three most frequently mutated genes in the mesenchymal subtype of GBM (Verhaak et al. 2010). In addition, I designed short hairpin RNA (shRNA) for *MYT1L* knockdown to investigate the role of MYT1L depletion in tumor initiation within the tumor organoid model. Two shRNAs (*shMYT1L_1* and *shMYT1L_2*) were tested in induced neurons (iNs). This experiment was performed by the master student Heather Schloo under my supervision. iNs were generated by NGN2 overexpression (Pak et al. 2018), and harvested at day 7 to analyze the protein expression of MYT1L, TUJ1, and MAP2. Both shRNAs significantly decreased MYT1L protein levels, with the *shMYT1L_1* showing stronger downregulation (Fig. 16B). Protein levels of TUJ1 and MAP2 were not significantly changed by *shMYT1L_1* expression, while treatment with *shMYT1L_2* led to significantly reduced TUJ1 protein levels and cell death. This observation suggested that *shMYT1L_2* construct possibly induced unwanted off-target effects. Since *shMYT1L_1* showed efficient knockdown of *MYT1L* without off-target effects, it was selected to investigate the effects of MYT1L loss in the brain tumor organoid model.

Next, I confirmed the CRISPR/Cas9-mediated mutations of *NF1*, *PTEN,* and *TP53* by transfection of hESCs with different single guide RNAs (sgRNAs). The genomic regions targeted by sgRNAs were analyzed by gDNA sequencing. To test the cutting efficiency induced by sgRNAs, the corresponding sequences were analyzed with the Tracking of Indels by DEcomposition (TIDE) software (https://tide.nki.nl/). For all three targeted loci, *NF1*, *PTEN* and *TP53*, mutagenesis could be confirmed using published sgRNAs (Bian et al. 2018). The total editing efficiency was determined with 20.2%, 51.9% and 50.3%, respectively (Fig. 16C; Supp. Fig. 8).

In addition to the validated sgRNAs against *NF1*, *PTEN* and *TP53*, and the shRNA *shMYT1L_1*, I stably transfected the EBs with mNeonGreen (mNG) using a PiggyBac transposon system. All constructs were introduced by nucleofection of EBs.

The quantification of the mNG fluorescence intensity in the organoids served as a readout of the expansion of targeted cells over time. Two days after nucleofection, all EBs showed a similar intensity of labeled cells based on microscopy imaging, but 28 days post-nucleofection, higher fluorescence intensity indicating robust cellular expansion within the organoids was observed in the positive control *NF1*$^{-/-}$*PTEN*$^{-/-}$*TP53*$^{-/-}$ (*N/P/P*) (Fig. 15D). In comparison, loss of only *PTEN* and

TP53 (*P/P*) induced more moderate growth and seemed to represent a milder tumor model. Next, I modified organoids of the *P/P* condition with an additional shRNA against *MYT1L.* Two days after nucleofection, the EBs contained similar amounts of mNG+ cells compared to the other conditions (Fig. 16D). 28 days post-nucleofection mutations of *PTEN* and *TP53* combined with knockdown of MYT1L showed similar effects to the positive control *(N/P/P)* and a strongly increased mNG intensity compared *to P/P.* Knockdown of *MYT1L* alone only led to a slight increase of mNG intensity signal (Fig. 16B).

Additionally, I also tested the impact of genetic *MYT1L* depletion on cellular expansion by using either H1 wildtype (H1 WT) or an H1 cell line with heterozygous *MYT1L* depletion (H1 *MYT1*$^{+/-}$). Heterozygous deletion of MYT1L in combination with the CRISPR-mediated mutations of *PTEN* and *TP53* led to a significant increase of mNG intensity in organoids compared to MYT1L WT (Supp. Fig. 9). This observation confirmed the previous findings with shRNA-mediated knockdown of *MYT1L*. In both models, the loss of MYT1L increased tumor-like outgrowth in an organoid brain tumor model.

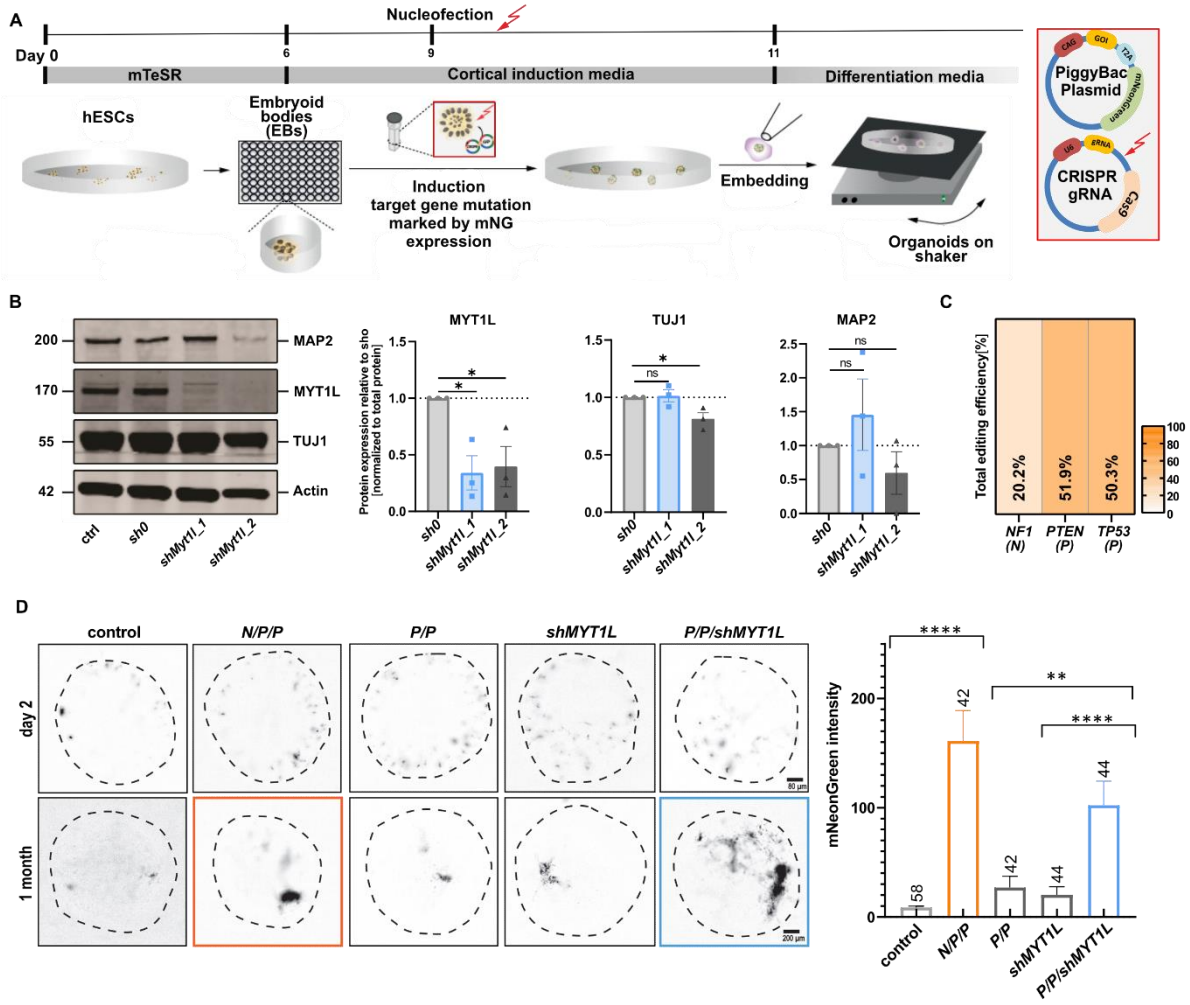

Figure 16: MYT1L depletion promotes cellular expansion in organoids

(A) Schematic illustration for the generation of cerebral organoids from human embryonic stem (hES) cells including the introduction of tumorigenic events by nucleofection. (B) *shMYT1L_1* and *shMYT1L_2* knockdown efficiency in induced neurons. Representative Western blot showing MYT1L, MAP2, TUJ1, and Actin after 7 days of NGN2 expression. Quantification of MYT1L, TUJ1, and MAP2 protein expression relative to control shRNA (*sh0*) after normalizing to total protein (n = 3 biological replicates). Bar graphs represent mean values, error bars = SD, two-sided t-tests, * $p < 0.05$, ns = not significant. (C) Efficiency of sgRNAs against *NF1, PTEN* and *TP53.* Genomic DNA was isolated at day 7 from human embryonic stem cells (hESCs) after lentiviral transfection. Sanger sequencing results were analyzed with Tracking of Indels by decomposition (TIDE) software. Total editing efficiency was determined with 20.2%, 51.9% and 50.3%. n =3 for each sgRNA. (D) Representative fluorescence images (left) and quantification (right) of mNeonGreen (mNG+) intensity in cerebral organoids at day 2 and 28 after tumor suppressor mutagenesis and/or MYT1L knockdown. Increased mNG intensity in tumor organoids upon shRNA-mediated *MYT1L* knockdown was observed. Left to right: control (n=58), *NF1-/-PTEN-/-TP53-/- (N/P/P)* (n=42), *PTEN-/-TP53-/- (P/P)* (n=42), sh*MYT1L* (n=44), *PTEN-/-TP53-/-*sh*MYT1L* (*P/P/*sh*MYT1L)* (n=44); 5 batches. Day 2 scale bar = 80 µm, day 28 scale bar = 200 µm. Bar graphs represent mean values, error bars = SEM, two-sided t-tests. ** $p < 0.01$, **** $p < 0.0001$.

4.3.3 MYT1L inhibited proliferation of PDGCs

Since a reduction in MYT1L levels led to increased cellular expansion within cerebral organoids, I hypothesized that increasing MYT1L expression levels might exert the opposite effect and decrease growth and proliferation. I decided to test this hypothesis in patient-derived glioma cell lines (PDGCs). To assess the effects of MYT1L on the proliferation of PDGCs, I performed an AlamarBlue proliferation and viability assay. Therefore, I generated a P3XX cell line with constitutive MYT1L overexpression and two S24 cell lines with either constitutive or inducible MYT1L overexpression (Fig. 17). Both cell lines share mesenchymal subtype features (Jung et al. 2021), and lack endogenous MYT1L expression. MYT1L overexpression in P3XX and S24 cell lines did not significantly alter steady state metabolic activity/viability (as measured on day 0) compared to control. However, their proliferation (exponential growth phase from day 1 to day 5) was significantly decreased upon MYT1L overexpression in both cell lines (Fig. 17A,B).

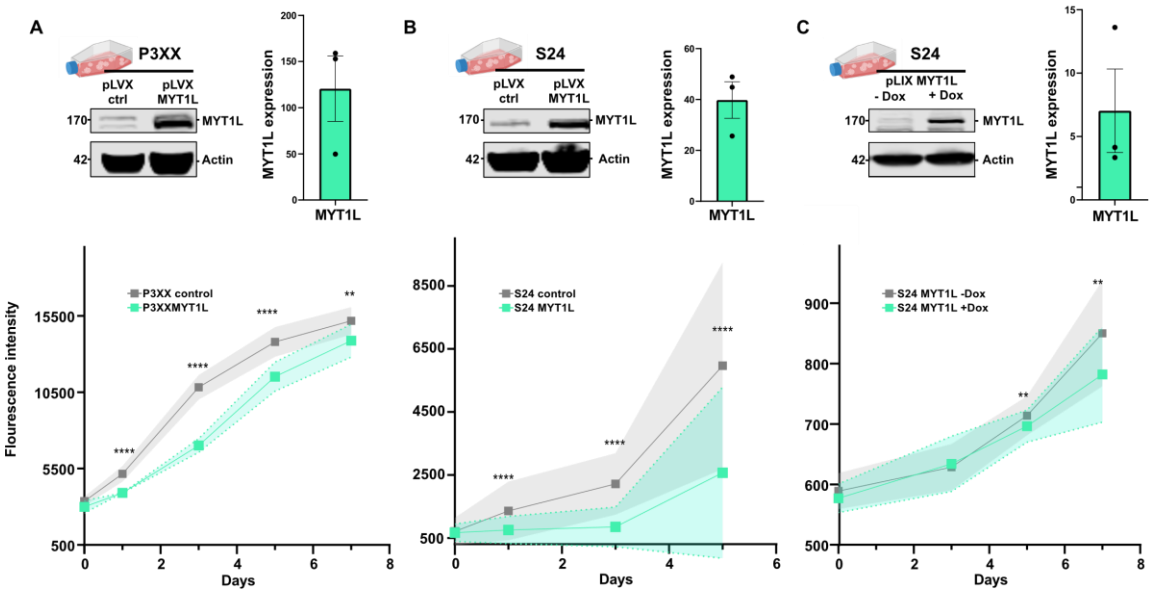

Figure 17: MYT1L reduces cell proliferation and viability in PDGCS
(A-C) Top to bottom panel shows MYT1L protein levels in Western Blot and AlamarBlue cell viability and proliferation assay performed with constitutive MYT1L OE in P3XX and S24 PDGCs as well as in S24 cell lines with inducible MYT1L OE. MYT1L reduced cell proliferation in all cell lines. MYT1L overexpression in the different lines was confirmed by Western Blot. MYT1L protein expression relative to control after normalizing to total protein; bar graphs represent mean values, error bars = SD, two-sided t-tests. Each AlamarBlue experiment was performed with three biological replicates; Statistical analysis was performed using one-way ANOVA test; data presented as mean±SD. * $p < 0.05$, **, $p < 0.01$, ***$p < 0.001$, ****$p < 0.0001$.

The generation of cell lines with constitutive MYT1L overexpression required antibiotic selection and the subsequent expansion of the selected cells lasted 1.5 months. During this period cells might acquire additional changes due to the MYT1L overexpression. To investigate the immediate effects of MYT1L on PDGC proliferation, I generated a S24 cell line with Doxycycline (dox)-inducible overexpression of MYT1L. Inducing overexpression of MYT1L also provided the opportunity to investigate the changes that occur in comparison to an isogenic control, allowing greater confidence that the changes observed are only due to MYT1L modulation. During the AlamarBlue experiment, MYT1L overexpression was induced by adding dox at day 0. The first measurements at day 0 were performed shortly after dox induction and no changes in metabolic activity/viability were observed between the induced and uninduced condition. Like the constitutive MYT1L overexpression, a significant decrease in proliferation was observed after 5-7 days of induced MYT1L overexpression (Fig. 17C).

Taking these findings together, MYT1L had an anti-proliferative effect of PDGCs *in vitro*.

4.3.4 MYT1L decreased cell invasion of PDGCs

MYT1L decreased proliferation in S24 and P3XX cells. Given the interdependence of proliferation and invasion in GBM (Xie et al. 2014), MYT1L might also exert effects on the invasiveness of these cells. I tested this hypothesis with an *in vitro* invasion assay. The invasion distance was quantified at days 3, 5, and 7. MYT1L overexpression in tdTomato labelled S24 (S24tdTom) cell line led to reduced colonization of the gel matrix. The total length of invasion was altered already at day 1 of the assay but significantly decreased starting from day 5 (Fig. 18A).

Additionally, dox-inducible S24tdTom cells were used to overexpress MYT1L at day 0 of the invasion assay. The total length of invasion was significantly reduced upon induced MYT1L overexpression, and the differences were significant starting as early as 3 days after induction (Fig 18B). Furthermore, invasion from the border of the spheroid core to the outermost invading cells was significantly reduced at day 7.

Together these findings showed that MYT1L can reduce invasion and migration of PDGCs *in vitro*.

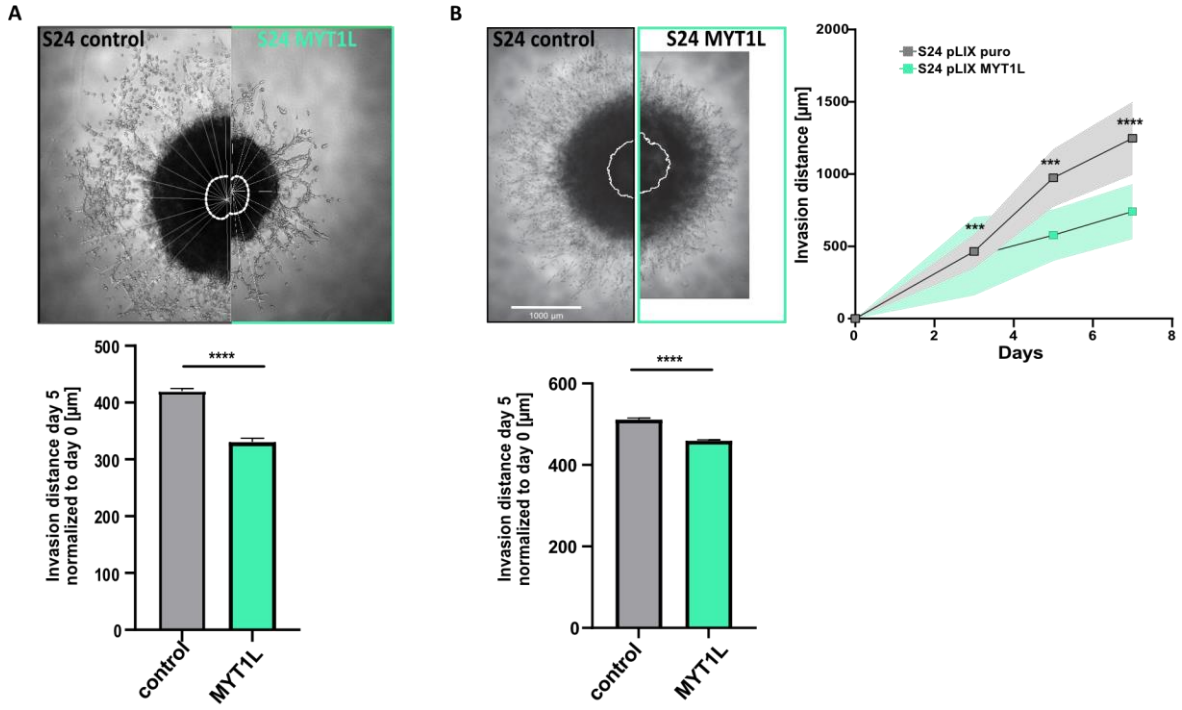

Figure 18: MYT1L reduces cell invasion of PDGCs
In vitro invasion assay showed reduced invasion upon MYT1L overexpression. (A) Invasion was decreased in S24 spheroids with constitutive MYT1L expression. Shown are representative brightfield images of spheroids at day 5 with day 0 area circled in white and quantification of net invasion distance normalized to radius at day 0 from 3 biological replicates. (B) Invasion was also decreased in S24 cell spheroids with inducible MYT1L expression with induction of MYT1L at day 0. Brightfield image of representative spheroid at day 5 with day 0 area circled in white; quantification of invasion distance normalized to radius at day 0 and time course of changes in invasion distance over first 7 days; three biological replicates with minimum n=8 spheroids per condition and replicate. Statistical analysis was performed using one-way ANOVA test. Data presented as mean±SD. Scale bar 1000 µm. ***p < 0.0001; ****p < 0.0001.

4.3.5 MYT1L affected invasion and proliferation by transcriptional repression

The transcriptional function of MYT1L has been investigated in different studies, in which some report that MYT1L acts as a transcriptional repressor (Mall et al., 2017; Manukyan et al., 2018; Melhuish et al., 2018). However, others describe an activating transcriptional role of MYT1L during early brain development (Chen et al., 2021; Kepa et al., 2017).

Together with Heather Schloo (DKFZ Heidelberg), I tested whether MYT1L exerts anti-proliferative and anti-invasive effects in PDGCs by acting as a transcriptional activator or as a transcriptional repressor. This experiment was performed by using a fusion protein approach, where either an activator (VP64) or a repressor (EnR) domain was fused to the C-terminus of a minimal DNA-binding domain (DBD) (Fig. 19A). MYT1L contains six zinc finger domains, of which two in the center have been characterized as a minimal functional DBD (Mall et al., 2017).

The VP64 activator consists of four tandem repeats of the minimal activation domain of VP16 (amino acids 437-447) from herpes simplex virus (Beerli et al., 1998). The engrailed (EnR) repressor domain (amino acids 1-298) from Drosophila melanogaster was selected as repressor (Jaynes and O'Farrell, 1991).

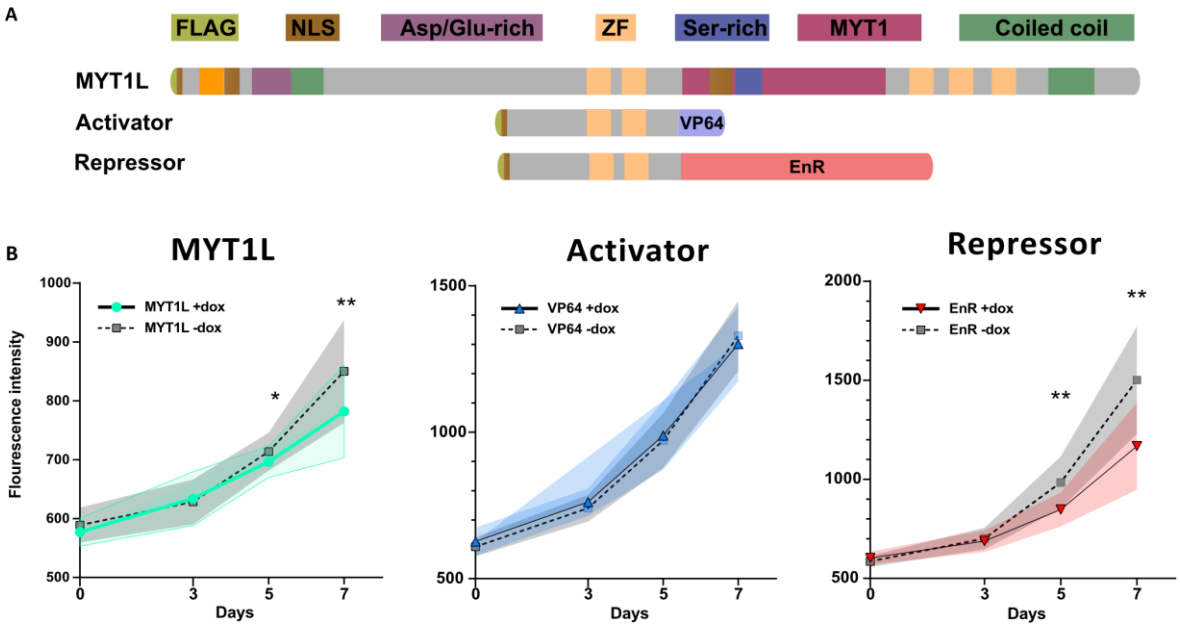

Figure 19: Activator and repressor fusion experiment showed that MYT1L exerts anti-proliferative effects by a repressive function

(A) Schematic of inducible fusion proteins with activator (VP64) or repressor (EnR) fused to C-terminus of MYT1L DNA binding-domain. NLS=Nuclear localization signal; ZF=Zink finger. (B) AlamarBlue cell viability and proliferation assay showed reduced cell proliferation for MYT1L and repressor fusion; three biological replicates with n=10 wells per condition and replicate. Bars represent mean values, error bars = SD, two-sided unpaired t-tests; * $p < 0.05$, **, $p < 0.01$. Analysis together with Heather School.

The effect on the proliferation capacity of the activator and repressor fusion proteins on S24tdTom cells was investigated by the AlamarBlue assay. After 5-7 days of MYT1L expression, a significant decrease in proliferation was observed (Fig. 19B). The EnR-repressor condition induced a striking suppression of proliferation and mimicked the anti-proliferative effect of MYT1L. The VP64-activator fusion did not exert an effect on proliferation.

Next, invasion assays were performed with the modified cell lines. In addition to brightfield analysis, fluorescence images of the tdTom signal were used to quantify the density of invading cells and the whole area of the spheroids. To reduce effects of variability among cell lines, dox-induced spheroids were normalized to uninduced spheroids of the same cell line as an isogenic control. In parallel to the invasion assay, spheroids were cultured and harvested to evaluate RNA levels of the fusion proteins after 7 days of induction (Supp. Fig. 10). The invasion assays confirmed the earlier observation that MYT1L significantly decreased invasion distance (Fig. 20A). Additionally, the fluorescence images revealed a significant decrease in the density of invading cells and the area of the whole spheroid. In the VP64 activator spheroids, I observed no significant difference in the length of invasion distance. Interestingly, the density of invading cells as well as the whole area of the spheroids were significantly increased in the VP64 spheroids upon dox induction (Fig. 20B). The most striking phenotype was observed with the repressor fusion protein, where the invasion distance, invasion zone density as well as the size of the whole organoid were strongly reduced (Fig. 20C).

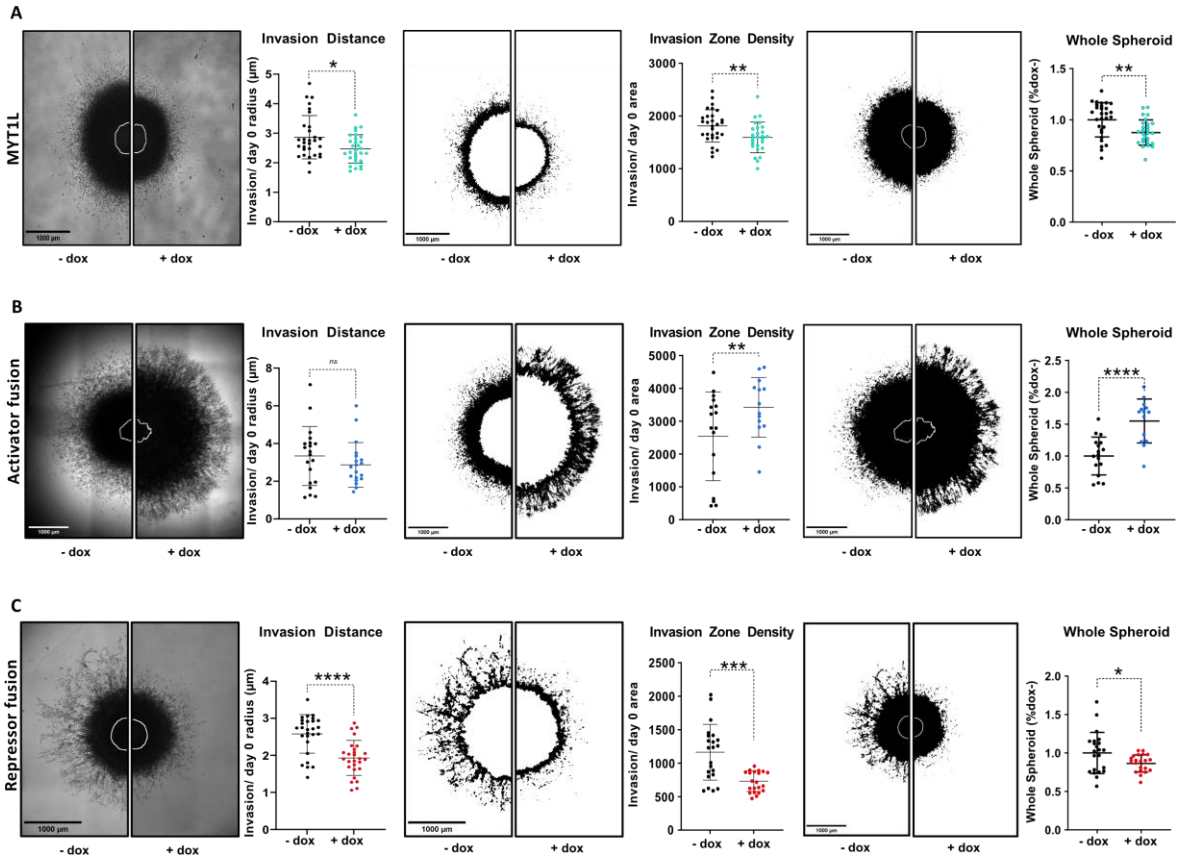

Figure 20: Activator and repressor fusion experiment showed that MYT1L exerts anti-invasive effects by a repressive function
(A-C) Invasion assays comparing MYT1L with activator and repressor proteins fused to the DNA binding domain of MYT1L. From left to right: Brightfield images of representative spheroids at day 7 with day 0 area circled in white; quantification of invasion distance normalized to radius at day 0; invasion zone density at day 7; quantification of invasion zone density normalized to day 0 area; area of whole spheroid at day 7; quantification of area of whole spheroid normalized to day 0 area. (A) Doxycycline induction of full length MYT1L decreased net invasion distance(dox- n=5/30, dox+ n=5/30), invasion zone density (dox n=4/29, dox+ n=4/27) and area of whole spheroid (dox- n=4/29, dox+ n=4/27) (B) Activator fusion did not alter net invasion distance (dox- n=4/20, dox+ n=4/20), but increased invasion zone density (dox- n=3/17, dox+ n=3/14) and area of the whole spheroid (dox- n=3/17, dox+ n=3/14). (C) Repressor fusion decreased net invasion distance (dox- n=4/27, dox+ n=4/27), invasion zone density (dox- n=3/22, dox+ n=3/21) and area of the whole spheroid (dox- n=3/22, dox+ n=3/21). Analysis and figures by Heather Schloo.

These results show that MYT1L has a predominantly repressive function in S24 PDGC spheroids, given that the repressor fusion mimics MYT1L function by reducing invasion and proliferation, and the activator fusion differs from MYT1L by inducing an increase in invasion. This indicates that MYT1L exerts its anti-invasive and anti-proliferative effects by acting as a transcriptional repressor.

4.3.6 MYT1L reduced tumor microtube formation of PDGCs

Previously, a study by Osswald and colleagues, provided the formation of tumor microtubes (TMs) as a mechanism that facilitates the massive invasion and proliferation of GBM cells (Osswald et al. 2015). TMs are defined as and long and highly dynamic membrane protrusions of glioma cells that connect glioma cells with each other and the surrounding tissue (Wang et al. 2022b).

I aimed to test whether MYT1L affects the formation of TMs in PDGCs and thereby performs its anti-proliferative and anti-invasive effect that I found in this study.
Together with Dirk Hoffmann (DKFZ Heidelberg), I investigated tumor microtube (TM) length as a readout for cell connectivity in an *in vitro* 2D monolayer assay. TM length was studied in S24 tdTom cells with constitutive MYT1L overexpression. Additionally, I investigated the effect of loss of MYT1L on TM length. Therefore, I generated a shRNA-mediated *MYT1L* knockdown (KD) line using the BG5 tdTom PDGC line which shares mainly features of the proneural/NPC state (Hoffmann et al., unpublished data), and expresses MYT1L endogenously.
MYT1L overexpression resulted in a significantly decreased length of TMs 8 days after seeding. The observation that the same number of nuclei were present per ROI confirmed similar seeding densities in the overexpression and control condition (Fig. 21A). Reduced connectivity upon MYT1L overexpression was clearly noticeable based on reduced TM length and cells with MYT1L overexpression showed an aggregated morphology (not quantified).
On the other hand, *MYT1L* KD in BG5 tdTom cells resulted in the opposite phenotype. Here, reduction of MYT1L led to a significant increase in TM length (Fig. 21B). Additionally, the

representative images indicated that *MYT1L* knockdown cells developed thicker cell bodies and thicker TMs.

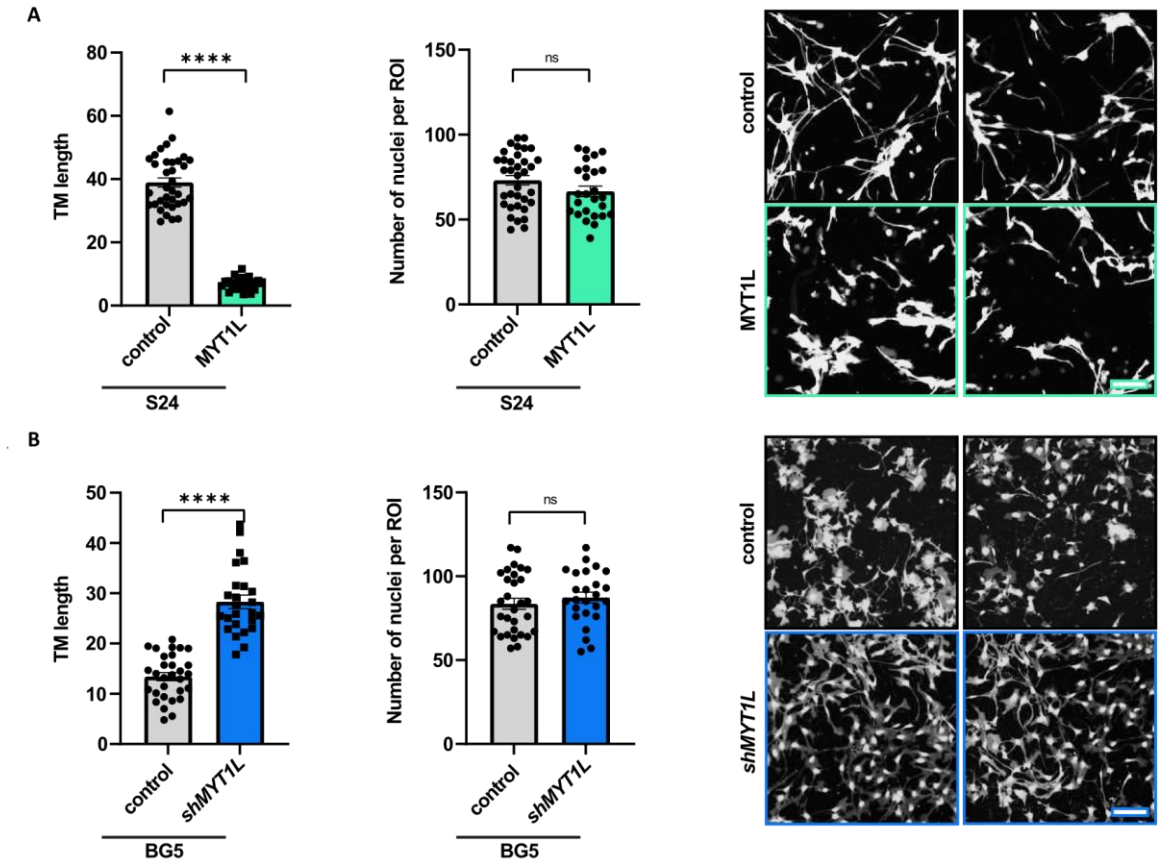

Figure 21: 2D monolayer assay showed decreased TM length upon MYT1L overexpression in S24 cell line and increased TM length upon loss of MYT1L in BG5 cell line
(A) MYT1L decreased TM length of S24 PDGCs measured by the "Sum of Euclidean diameter per number of cells per ROI". From left to right: Quantification of TM length and quantification of number of nuclei per ROI and representative images of MYT1L OE and control. (B) Reduced MYT1L levels upon shRNA-mediated knockdown increased TM length of BG5 PDGCs measured by the "Sum of Euclidean diameter per number of cells per ROI". From left to right: Quantification of TM length and quantification of number of nuclei per ROI and representative images of *shMYT1L* and control. For quantifications, ROIs with nuclei numbers ± 1x standard deviation were removed from the analysis. Data are means ± standard deviations (n = 2). Student´s t-test; ****P < 0.0001, ns= not significant. Analyzed by Dirk Hoffmann (DKFZ, Heidelberg).

4.3.7 MYT1L inhibited tumor cell invasion and proliferation *in vivo*

I showed that MYT1L had striking anti-invasive and anti-proliferative effects using different *in vitro* assays. These findings raised the possibility that expressing MYT1L in tumor cells *in vivo* may also reduce tumor growth. This was explored by implantation of S24 tdTom cells with constitutive overexpression of MYT1L into an orthotopical xenograft model combined with intravital two photon-microscopy (Osswald et al. 2015). With this approach, tumor cell proliferation and invasion can be followed in the brain in living mice. Implantation and *in vivo* 2-photon microscopy were performed by Dr. Erik Jung (former researcher Winkler lab, DKFZ Heidelberg).

Remarkably, three weeks after implantation, S24 tdTom cells with MYT1L overexpression formed smaller tumors with massively impaired tumor-cell invasion (Fig. 22). The quantification indicated a significant decrease in the absolute cell count for tumors with increased MYT1L expression compared to control.

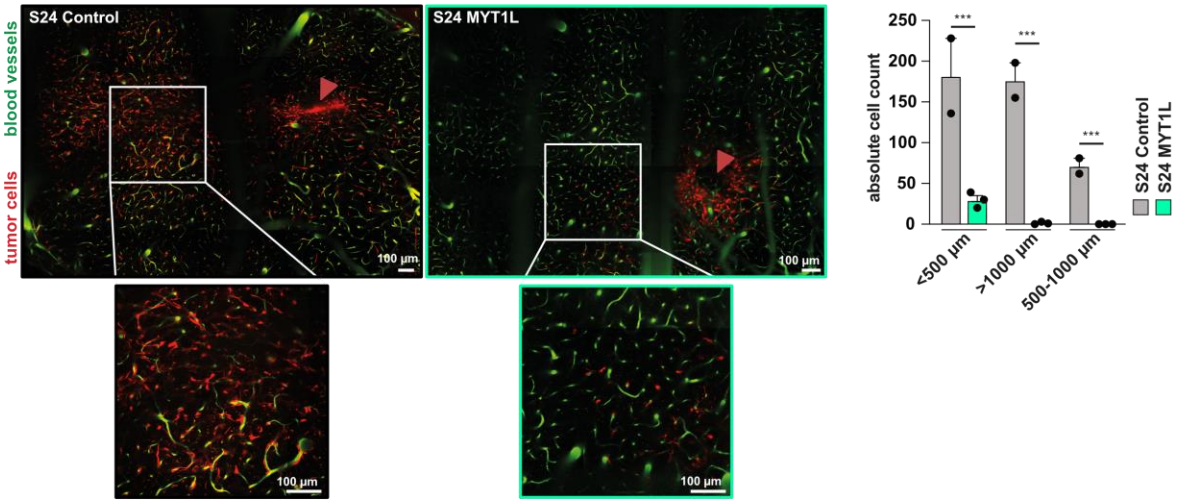

Figure 22: MYT1L overexpression *in vivo* reduced tumor cell proliferation and invasion
Proliferation and invasion were reduced in the MYT1L OE (n = 3) vs. control (n = 2) measured by the absolute cell count at different distances from the injection side (indicated by red arrow). Tumor cells (red) and blood vessels (green) of patient-derived xenografts of S24 tdTomato PDGCs with constitutive expression of MYT1L, orthotopically injected into cranial window of mice and imaged with *in vivo* 2-photon microscopy 21 days post-injection. Statistical analysis was performed using one-way ANOVA test. Data presented as mean±SD. *** $p < 0.001$. Scale bars 30 µm, 60 µm, 100 µm. Data and analysis courtesy of Dr. Erik Jung.

These results indicate that MYT1L suppresses tumor cell proliferation and progression *in vivo* and motivate further exploration of the mechanisms by which MYT1L exerts these effects.

4.3.8 MYT1L expression upregulated neuronal gene programs and downregulates glioma-associated genes

Based on the effects that MYT1L exerts on proliferation and invasion in PDGCs *in vitro* and *in vivo*, I aimed to explore whether gene expression changes that might explain this mechanistically. Three generated PDGC lines were analyzed by bulk RNA-seq: S24 and P3XX with constitutive MYT1L overexpression as well as the BG5 cell line with *MYT1L* KD together with their respective controls (Table 1).

In the S24 line 83.3% and in the P3XX line 67.7% of all DE genes were upregulated. The direct comparisons of upregulated overlapping DE genes of the two lines showed an overlap of 462 genes, which corresponds to 23.8% (Fig. 23A).

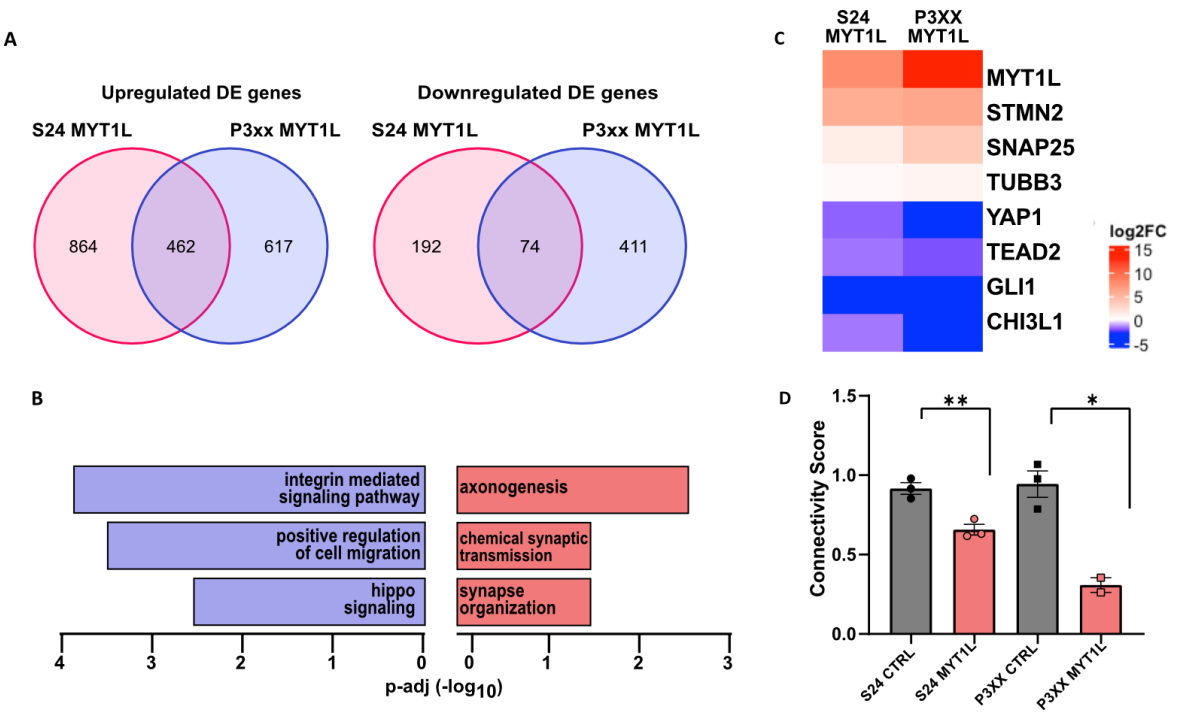

Figure 23: Gene expression changes upon MYT1L overexpression in two PDGC lines.
(A) Gene expression analysis revealed downregulated (blue) and upregulated (red) genes of S24 and P3XX. More genes (83.3% in S24 and 67.7% in P3XX) appeared to be upregulated. (B) Selected top gene ontology (GO) terms upon MYT1L overexpression in S24 PDGCs and p-adj values. Log2-fold change >|1|; p-adj. <0.01 (C) RNA-seq expression values (log2 fold change) of MYT1L and selected targets, normalized to control; n = 3 in two cell lines S24 and P3XX. Myt1l represses several proliferation-associated genes. Bulk RNA-seq data for (A-C) analyzed by Bryce Lim and Laura Rueda Gensini (DKFZ Heidelberg) (D) MYT1L reduced connectivity score in S24 and P3XX. Two-sided t-tests, * $p < 0.05$, ** $p < 0.01$. Bulk RNA-seq data analyzed by Ling Hai (DKFZ Heidelberg). S24 (CTRL n = 3, MYT1L n = 3) and P3XX (CTRL n = 3, MYT1L n = 2).

GO analysis in the two MYT1L overexpressing cell lines revealed that gene programs related to neuronal development were upregulated, including axonogenesis, chemical synaptic transmission, and synapse organization (Fig. 23B). These findings align with previous research, where MYT1L promoted neuronal fate and was utilized in neuronal reprogramming (Mall et al., 2017; Vierbuchen et al., 2010). The gene programs downregulated by MYT1L were related to integrin signaling, cell migration, and Hippo signaling. Integrin signaling is essential to the metastasis cascades, and its downregulation alongside cell migration therefore suggests that MYT1L may reduce metastatic potential (Ganguly et al., 2013). Reduction in Hippo signaling is reported for gliomas and mediates cell proliferation among other processes (Zhang et al., 2016). Thus, these results confirm the earlier observations from the AlamarBlue assays where MYT1L expression reduced proliferation in PDGCs.

Next, I focused on specific genes which appeared to be either up- or downregulated upon MYT1L overexpression. Among the top upregulated genes in both cell lines, I found the neuronal lineage specific genes STMN2, SNAP25 and TUBB3 (Fig. 23C). All three genes were described as marker genes for the NPC2-like GBM cell state identity (Neftel et al. 2019). One important gene set that

was downregulated in both cell lines was Hippo signaling pathway, including YAP1, as well as TEAD genes. Additionally, GLI1 and CHI3L1 appeared to be downregulated upon MYT1L overexpression (Fig. 23C). Both genes are associated with higher malignancy of GBM and resistance to chemo- and radiotherapy (Santoni et al. 2013; Li et al. 2022).

Further analyses by Ling Hai (Wick lab, DKFZ Heidelberg) revealed a significant decrease in connectivity score in S24 as well as P3XX lines with MYT1L overexpression (Fig. 23D). This analysis is in line with the observed reduction of TM length, indicating reduced cell connectivity in the 2D monolayer assay.

Besides the striking effects observed upon MYT1L overexpression in S24 and P3XX cell lines, I also wanted to investigate potential gene expression chances upon reduction of MYT1L levels in the BG5 PDGC line. Upon shRNA-mediated KD of MYT1L, more DE genes appeared to be upregulated (Fig. 24A). Comparison of up- and downregulated IPA conical pathways between the BG5 MYT1L KD and the two MYT1L overexpressing cell lines showed opposing effects (Fig. 24B). For example, the SNARE signaling pathway, CREB signaling pathway, and S100 family signaling pathway were found to be downregulated in the BG5 KD line. While the former two are correlated with neuronal mechanisms and functions, the latter is associated with mesenchymal transition (Wang et al. 2022a).

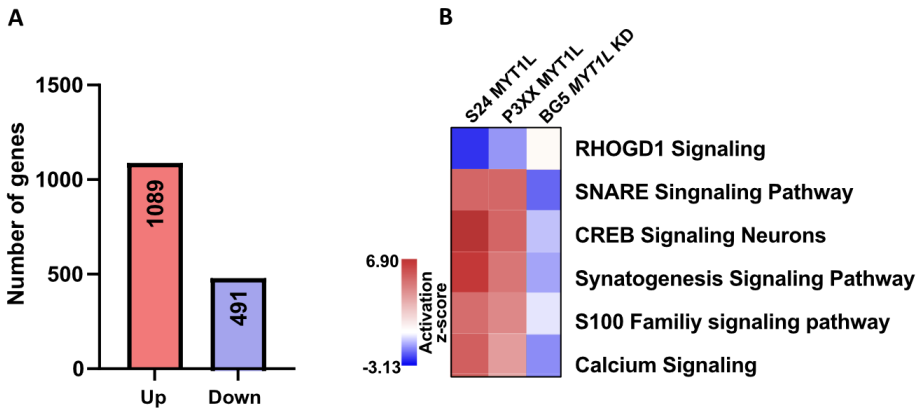

Figure 24: Gene expression changes upon MYT1L knockdown in BG5 PDGCs
(A) Gene expression analysis showed more upregulated (red) DE genes than downregulated (blue) in the BG5 cell line upon KD of *MYT1L* (B) Ingenuity Pathway Analysis (IPA) comparison of canonical pathways up- and downregulated upon MYT1L OE in S24 and P3XX and sh*MYT1L* KD in BG5. Blue: downregulated pathways, red: upregulated pathways; z-score scale ranges from -3.13 to 6.0. Bulk RNA-seq data analyzed by Bryce Lim and Laura Rueda Gensini (DKFZ Heidelberg). S24 (CTRL n = 3, MYT1L n = 3); P3XX (CTRL n = 3, MYT1L n = 2); BG5 (CTRL n = 3, *MYT1L* KD = 3).

4.4 Regulation of GBM subtype identity by MYT1L

A third aspect in the framework of unlocking phenotypic plasticity is represented by transdifferentiation. In process, tumor cells can transition into other cell states and acquire features of a different cell lineage. Depending on the acquired features, this can either reduce or promote the malignancy of the tumor. One of the most frequently described transdifferentiations processes in cancer is the epithelial to mesenchymal transition (EMT).

Findings from my bulk RNA sequencing of PDGC lines showed that MYT1L overexpression downregulated gene programs related to EMT. On the other hand, neuronal-related gene programs and marker genes of the NPC2-like GBM identity, such as STMN2, SNAP25 and TUBB3 appeared to be upregulated. Therefore, I hypothesized that MYT1L may be associated with a specific GBM subtype or even acts as a regulator of GBM subtype identity. To explore this potential connection, bulk RNA-seq data was further analyzed by Ling Hai for subtype analysis according to RNA-seq data from Neftel et al. (2019) and Wang et al. (2017). Regarding the Neftel cell state scores, MYT1L overexpression in S24 and P3XX PDGCs showed trends of increasing NPC1-like and NPC2-like scores and decreasing MES1-like and MES2-like scores (Supp. Fig. 11). The OPC-like scores showed a slight increase, and the AC-like was heterogeneous across all cell lines. Within the Wang subtype classification, scores for the mesenchymal subtype were decreased and an increase in proneural scores could be observed upon MYT1L overexpression (Fig. 25A). This is also in line with earlier analyses of single cell RNA sequencing data from Neftel et al. (2019) which showed a strong correlation of MYT1L expression with the NPC2-like cell state (Fig. 5C).

In contrast, MYT1L KD in BG5 cells showed a reduction in proneural scores, while mesenchymal subtype scores were increased (Fig. 25B).

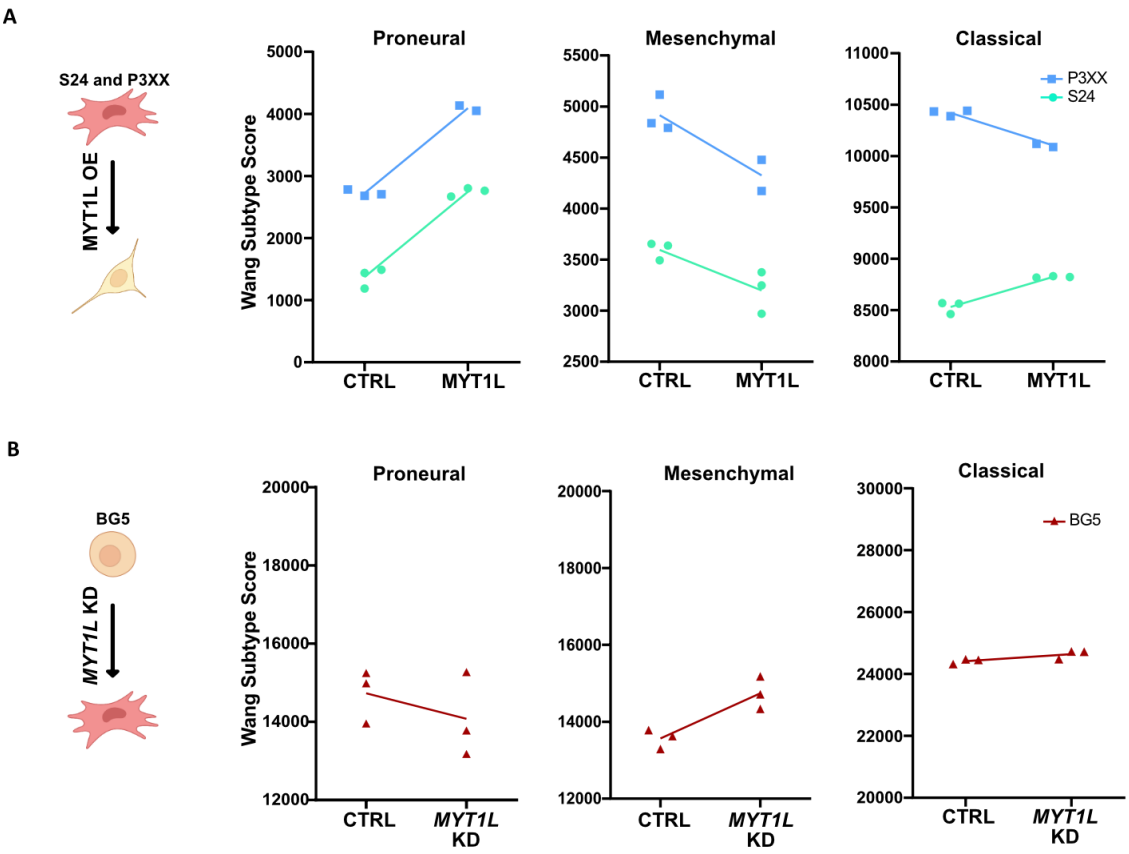

Figure 25: MYT1L induces changes in GBM subtype identity scores
(A) GBM subtype scores (Proneural, Classical, Mesenchymal by Wang) for S24 (CTRL n = 3, MYT1L n = 3), and P3XX (CTRL n = 3, MYT1L n = 2) upon MYT1L overexpression (B) GBM subtype scores (Proneural, Classical, Mesenchymal by Wang) for BG5 upon *shRNA*-mediated knockdown of MYT1L (CTRL n = 3, MYT1LKD n = 3). Line indicates mean. Wang subtype scores RNA-seq data analysis by Ling Hai (DKFZ Heidelberg).

Together, this shows that MYT1L might drive GBM subtype transdifferentiation away from mesenchymal/ MES-like subtypes towards proneural/NPC-like subtypes, where the latter is associated with better patient prognosis (Ozawa et al. 2014).

5 DISCUSSION

MATURE NEURONS COULD SERVE AS GLIOMA CELL-OF-ORIGIN

LOSS OF MYT1L ENHANCES PROLIFERATION IN ORGANOIDS BRAIN TUMOR MODEL

MYT1L ACTS AS TUMOR SUPPRESSOR IN PATIENT-DERIVED CELLS

REPRESSION OF YAP1 MAY MEDIATE THE TUMOR-SUPPRESSING EFFECTS OF MYT1L

MYT1L – A POTENTIAL MASTER REGULATOR OF NPC-LIKE GBM SUBTYPES

5. DISCUSSION

Unlocking phenotypic plasticity represents one of the new emerging cancer hallmarks and can be conceptualized by three major processes: Dedifferentiation, blocked differentiation, and transdifferentiation. Transcriptional regulators that induce and maintain cell identity can orchestrate these processes. Consequently, loss or mutations of such regulators could cause cancer formation (Hanahan 2022).

In the human brain, the transcription factor MYT1L was found to have an important function in neuronal differentiation (Mall et al. 2017; Vierbuchen et al. 2010). This suggests that dysregulation of MYT1L could impairs cellular differentiation and prevent the transition into a non-proliferative state. The fact that MYT1L is expressed lifelong most likely indicates that it is important for maintaining the fate of differentiated neurons (Cardoso-Moreira et al. 2019). Therefore, loss of MYT1L could also unlock phenotypic plasticity of differentiated neurons and promote brain tumor formation. In the following sections, I discuss findings of my doctoral study identifying mature neurons as a potential brain cancer cell-of-origin, delineating MYT1L as a tumor suppressor in brain organoid and PDGCs, *in vitro* and *in vivo*, and finally showing the capability of MYT1L to regulate tumor subtype identity.

5.1 Mature neurons could serve as glioma cell-of-origin

To investigate whether loss of MYT1L could destabilize neuronal fate, I generated GBM mouse models for lineage-restricted MYT1L and tumor suppressor deletions. By targeting mature neurons, I aimed to determine whether loss of MYT1L could cause dedifferentiation and if mature neurons can therefore be a cell-of-origin for brain cancer.

In a first approach, I performed spatially- and temporally-restricted depletion of MYT1L as well as known tumor suppressors in mature neurons of the adult mouse cortex using a neuronal synapsin promoter-driven AAV system. I showed that depletion of the tumor suppressors PTEN and TP53 (*PP*), as well as the combined depletion of PTEN, TP53 and MYT1L (*PPM*), in mature neurons induced tumor formation. Interestingly, *PPM* mice developed tumors at earlier timepoints, causing shorter overall survival of *PPM* mice compared to *PP* mice. This suggests that depletion of MYT1L in addition to depletion of the tumor suppressors PTEN and TP53, accelerates tumor formation and progression. Pathway analysis based on gene expression data supported this assumption. Specifically, pathways related to tumor growth, cell migration and immune cell adhesion appeared to be upregulated in *PPM* mice compared to *PP* mice. This analysis was based on RNA sequencing

of the virally targeted cells 8 weeks after AAV injection and further supports that tumor development starts earlier in *PPM* than in *PP* mice. Thus, the additional loss of MYT1L enhanced tumor formation. Notably, MYT1L loss alone did not induce tumor formation.

This experiment provided evidence, that MYT1L, together with other tumor suppressors, plays a crucial role in tumor formation and progression. Many advantages have been described for the use of AAV-mediated, promoter-specific gene modifications, such as lower costs, faster generation of genetic manipulation than germline manipulations and local gene targeting (Jankowsky and Zheng 2017). However, besides those strengths, AAV injections have severe weaknesses and limitations. Certain effects, such as enhanced immune responses upon AAV injection, can confound experimental results (Rogers et al. 2011). Indeed, I found several immune related pathways to be upregulated across all three injected mouse lines. These strong effects potentially masked other important gene expression changes that could provide more insights into the effects of MYT1L depletion. Another disadvantage of the system is reduced synapsin promoter-driven expression over time (Jackson et al. 2016). Reduced synapsin promoter-driven expression of the fluorescent reporter which was used to sort the cells for transcriptomic analysis could explain why the transgenes were only partly or not significantly decreased in the performed gene expression analysis. Importantly, the major weakness of this system is that our synthetic synapsin promoter may not exclusively be active in neurons and hence cre-induced recombination in non-neuronal cells cannot be excluded (Kügler et al. 2003).

Even though the AAV-based experimental approach faces serious limitations, it provides a first indication that tumor formation could indeed originate from mature neurons and that MYT1L loss might accelerate tumor formation and progression.

To overcome the described disadvantages of the AAV mouse model, I established a genetically engineered, inducible Cre-line mouse model. This technology allowed me to perform cell type specific deletions of common GBM tumor suppressors P*TEN* and *TP53*, as well as *MYT1L* depletion in the mouse brain. I targeted postmitotic excitatory neurons using CamK2aCreER^{T2} (iCK) mouse lines because it has been shown that CamK2a exhibits peak expression in neurons of the hippocampus and the mouse forebrain region (Wang et al. 2013). Homozygous depletion of *Tp53* and *Pten* in post-mitotic neurons resulted in tumor development in 20% of the animals. Two of these tumors were histopathologically characterized and showed high proliferative capacity by the presence of Ki67- and BrdU-positive cells. Furthermore, Nestin staining showed the presence of neural stem-like progenitor cells throughout the tumor but not within normal brain tissue. Moreover, GFAP and OLIG2 signal could be detected in the tumor tissue. OLIG2 marked glial tumor cells, whereas GFAP-positive reactive astrocytes formed a peri-tumoral border at the tumor margin.

Invasion and migration of those cells along the corpus callosum and the brain stem into the other hemisphere could be observed. Positive staining of phosho-S6 (pS6), a downstream target of the PI3 kinase and mammalian target of rapamycin (mTOR) pathway, indicated mTOR hyperactivation due to malfunction of PTEN and TP53. mTOR hyperactivation is associated with increasing cell proliferation and migration in GBM (Chiang and Abraham 2007).

While analysis of more tumors has to be performed to confirm these observations, initial histopathological analysis showed many of the classic features of high-grade (grade IV) gliomas, including high proliferation rates, invasion along the corpus callosum, mTOR pathway activation, as well as positive Nestin, OLIG2 and GFAP stainings. The presence of different linage markers for neural stem/progenitor cells, oligodendroglia and astrocytes may indicates elevated cell fate plasticity in the observed tumors.

Bulk RNA sequencing of prefrontal cortices of iCK *PP* mice revealed that most DE genes were downregulated, including several essential functional processes, such as cellular metabolic processes and biosynthetic processes. Previously it has been described that aberrant cellular metabolism upon loss of PTEN and TP53 enables cancer cells to adapt to their microenvironment which in turn facilitate their proliferation and tumor growth (Soga 2013). The upregulation of GFAP 4 weeks after tumor suppressor deletion might indicate early reactive astrogliosis as a response to pathological alterations in the brain (Henrik Heiland et al. 2019).

The observed tumor development upon targeting post-mitotic neurons significantly contributes to a controversial discussion about the cell-of-origin in glioma. Previous publications of Alcantara Llaguno et al. suggested that only stem cells or progenitor cells, targeted by NG2, Ascl1-, or Nestin-driven *Nf1*, *Pten* and *Tp53* deletions can give rise to tumor formation (Alcantara Llaguno and Parada 2016; Alcantara Llaguno et al. 2019). They also showed that CamK2a-driven homozygous knockout of *Nf1* and *Tp53* in combination with heterozygous knockout of the tumor suppressor *Pten* in mature neurons did not result in tumor formation, developmental or behavioral abnormalities, or neurological deficits. In their mutants, they could only observe areas of reactive astrogliosis, which was linked to paracrine reactive astrocytic response upon the neuronal loss of tumor suppressors (Alcantara Llaguno et al. 2019). These findings are not in agreement with my observations. However, my experimental approach differs from the Alcantara Llaguno et al. study as I performed homozygous knockout of the tumor suppressors *Pten* and *Tp53*. The observed tumor development in the iCK *PP* mice potentially suggests that homozygous loss of these tumor suppressors in post-mitotic neurons is sufficient to induce tumor formation. Remarkably, this would indeed support the controversial findings by Friedmann-Morvinski and colleagues (2012), that mature cells can be cell-of-origin in GBM. This study was subject to skepticism, as they induced oncogenic *H-ras* expression,

or *Nf1* and *Trp53* knockdowns broadly in the mouse brain. By driving expression from H1 and U6 promoters, genetic modifications were not exclusively limited to post-mitotic neurons in their system. In my study, I intended to overcome this weakness utilizing the described genetic models which allowed me to specifically target mature neurons. In both neuron-restricted knockout mouse models, the AAV-mediated and the genetically engineered model, I observed tumor formation.

In addition to the unexpected tumor formation in iCK *PP* mice, the observed phenotype induced by additional co-depletion of MYT1L in the iCK *PPM* model represents a highlight of this study. These mice showed significantly poorer survival compared to the iCK *PP* mouse line without tumor formation. On average, mice died as early as 44.5 days without obvious neurological abnormalities before their early sudden death. This observation might indicate that, together with tumorigenic mutations, MYT1L loss has a severe effect on the mouse brain. Bulk RNA sequencing analysis revealed upregulation of canonical pathways related to cardiovascular signaling as potential evidence for dedifferentiation processes. This was further corroborated by downregulation of many neuronal related GO terms including neuron differentiation. It is of special note that cancer related pathways, including glioma invasiveness and GBM signaling, were also found to be upregulated even though no tumors were detected in iCK *PPM* mice at the 4-week timepoints for transcriptome analysis before the mice died. Both downregulation of differentiation related Gos and upregulation of cancer related pathways support my hypothesis that the loss of MYT1L can induce dedifferentiation and consequently tumor formation. Notably, depletion of MYT1L alone did not affect the survival of mice. GO term analysis of iCK *M,* as well as iCK *PPM* mice showed downregulation of biological functions related to neuronal development, neurogenesis, and neuronal differentiation. The loss of neuronal gene expression upon loss of MYT1L reveals the important function of MYT1L in maintaining the neuronal cell fate of mature neurons and supports my hypothesis that loss of MYT1L destabilizes the neuronal fate.

To explain the sudden death of iCK *PPM* mice, the increased expression of Glutathione S-Transferase Alpha 4 (GSTA4) attracted my attention. GSTAs were found to be overexpressed in the mammalian epileptic brain (Board et al. 2000), and GST overexpression has been linked to poor prognosis of various kinds of tumors, including gliomas (Dasari et al. 2018). Recurrent unprovoked seizures represent a major feature of the epileptic brain and could potentially explain the sudden death of iCK *PPM* mice. Interestingly, seizures have also been reported in neurodevelopmental disorders associated with MYT1L mutations (Blanchet et al. 2017). Even though I did not observe spontaneous seizures, the possible correlation between seizures and the sudden death of iCK *PPM* mice needs further investigation. Additional histopathological analysis of iCK *PPM* brain sections

and electrophysiological analysis of iCK PPM mouse brains will clarify the effect of MYT1L loss on brain morphology and function.

In summary, I showed tumor development and severe phenotypes upon knockout of classical GBM tumor suppressors and MYT1L in mature neurons. This suggests that mature neurons can be the cell-of-origin in glioma. I propose that, through tumor suppressor mutations, post-mitotic neurons acquire the capacity to dedifferentiate towards a more stem-cell like state, gaining pro-proliferative features, ultimately enabling tumor formation. The loss of MYT1L, together with mutations of known tumor suppressors, likely enhances dedifferentiation processes, which was embodied by the early and sudden death observed in the iCK *PPM* mice. Combining the employed genetic mouse models with a lineage tracing approach is needed to substantiate my findings that tumor formation can indeed originate from mature neurons. While I already used membrane bound reporters (mT/mG) to confirm successful Cre-recombination in neurons of the mouse cortex in this study, additionally nuclear-specific lineage reporter systems are currently being established. Specifically tracing the cells targeted by the iCK promoter with a fluorescence marker will help to prove that only mature neurons of the mouse brain are targeted and determine the exact processes of dedifferentiation and cellular fate transformations caused by tumor suppressor mutations and loss of MYT1L in a time-resolved manner.

5.2 Loss of MYT1L enhances proliferation in organoid brain tumor models

Different studies suggest that MYT1L might play a role in tumor formation. For example, a study by Hu et al. (2013) showed that MYT1L knockdown in premalignant mouse NSCs could induce tumor formation. In GBM patients, MYT1L expression is significantly lower in tumor cells compared to normal brain tissue, and lower expression levels correlate with worse patient outcomes (Melhuish et al. 2018). Regarding the latter mentioned study, it must be mentioned that the significant survival difference between MYT1L low/high expressing patients could not be reproduced in my work. However, I was able to observe a trend that high MYT1L expression levels in patients correlate with better survival.

In this part of my study, I aimed to investigate the loss of MYT1L on tumor formation and progression by using cerebral organoids as a model system for human brain tumors. I was able to show that *MYT1L* knockdown in combination with loss of the tumor suppressors PTEN and TP53 increased cellular proliferation in human organoids. The increased tumor-like growth in the human cerebral organoid model upon depletion of *MYT1L*, *PTEN,* and *TP53* is in line with previously-observed tumor-promoting effects upon MYT1L loss in mice, as well as with the observed

correlation between lower MYT1L levels with worse GBM patient outcome (Hu et al. 2013; Melhuish et al. 2018). Additionally, the observation that MYT1L exhibits this effect only in combination with other tumor suppressors supports the notion that more than one oncogenic event is required to induce tumor formation (Kim et al. 2020).

In the brain tumor organoid model, increased cellular proliferation was observed upon MYT1L knockdown. This suggests that the targeted cells might remain in a progenitor-like state and are blocked from advancing into a non-proliferative state.

It has been previously shown, that MYT1L inhibits pro-proliferative and tumor-promoting pathways, such as Wnt, Notch, and Hedgehog signaling (Mall et al. 2017). The increased proliferation of targeted cell populations within the organoids upon loss of MYT1L can most likely be linked to the loss of repression of these pathways. However, further investigations on a mechanistic level are needed to prove this hypothesis. RNA sequencing of targeted, MYT1L depleted cells within the organoids will be performed to identify MYT1L target pathways, such as Wnt and Notch, as well as potential novel targets. In addition, experiments will be conducted to investigate MYT1L-dependent cell cycle dynamics. The increased proliferation in the organoids suggests that the loss of MYT1L may result in increased symmetric cell division rather than differentiation to a mature cell state. To gain insight into cell division changes upon MYT1L depletion at the single-cell level within organoids, a live cell-imaging approach will be used (Karzbrun et al. 2018).

5.3 MYT1L acts as tumor suppressor in patient-derived cells

The observation MYT1L loss increased tumor-like growth in the human brain tumor organoids supported its tumor-suppressive role in a human model. Therefore, I hypothesized that elevated MYT1L levels may reduce aggressive features of GBM, such as proliferation and invasion. To investigate whether MYT1L indeed acts as a tumor suppressor in GBM, I introduced MYT1L overexpression in S24 and P3XX PDGC lines. These cell lines show many features of tumor cells of the mesenchymal-like subtype (Jung et al. 2021). In PDGCs, MYT1L overexpression impaired cell migration dynamics and invasion. Interestingly, MYT1L overexpression caused PDGC spheroid core areas to expand less, indicating that MYT1L also had the capability to reduce proliferation. To analyze whether MYT1L could reduce proliferation in PDGC lines, I performed AlamarBlue assays to measure cell viability and proliferation. Indeed, MYT1L strongly decreased proliferation in the exponential growth phase of the cells. This is in line with earlier investigations by Hu et al. (2013), which showed that overexpression of MYT1L in PTEN and TP53 depleted GSCs reduced intracranial tumor formation and extended survival in mice.

Together with Heather Schloo (DKFZ Heidelberg), I further examined, whether MYT1L exerted its effects on invasion and proliferation by acting either as a repressor or activator. Based on previous publications, MYT1L was reported to act as a transcriptional repressor in neuronal differentiation (Mall et al., 2017; Manukyan et al., 2018), or transcriptional activator in early brain development (Chen et al., 2021; Kepa et al., 2017). In the glioma context, I showed, that the fusion of the DNA-binding domain of MYT1L to a repressor domain, resulted in decreased invasion and proliferation of PDGCs. This mimicked the previously described function of the full-length MYT1L and suggests that MYT1L exerts its effects through a repressive function.

In addition to the decrease in proliferation and invasion, I found that MYT1L decreased connectivity and length of tumor microtubes (TMs) in PDGCs *in vitro*. TMs are defined as membrane protrusions extended by glioma cells and are associated with GBM infiltration and treatment resistance (Wang et al. 2022b). The implication that MYT1L modulated TMs and glioma cell connectivity might represent another mechanism by which MYT1L exerts its tumor-suppressing effects. However, further functional as well as *in vivo* experiments are required to investigate which TM subtypes (non-connected or inter-connected) are affected by MYT1L and how this might influence multicellular network communication (Osswald et al. 2015; Hausmann et al. 2022).

Taken together, these results support the hypothesis that MYT1L acts as a tumor suppressor in GBM by decreasing proliferation, invasion, and connectivity *in vitro*. However, *in vitro* assays fall short in the comparison to the physiological condition of the living brain with regards to GBM heterogeneity and the complex tumor microenvironment. Therefore, I also examined the effect of MYT1L overexpression in an *in vivo* setting. Parallel to *in vitro* analysis, MYT1L overexpressing PDGCs were orthotopically implanted in a xenograft mouse model in collaboration with Dr. Erik Jung (DKFZ Heidelberg). Remarkably, 2-photon *in vivo* microscopy revealed formation of smaller tumors in the MYT1L overexpressing condition compared to control. PDGCs with MYT1L overexpression showed a massively impaired tumor-cell invasion. In a next step, orthotopic implantation of PDGCs will be performed in extended mouse cohorts to further investigate how MYT1L affects tumor cell connectivity *in vivo*.

5.4 Repression of YAP1 may mediate the tumor-suppressing effects of MYT1L

To better understand the mechanisms by which MYT1L exerts its tumor-suppressive effects in PDGCs, I performed bulk-RNA sequencing of two cell lines (S24 and P3XX) with induced MYT1L overexpression.

Transcriptomic studies and subsequent GO analysis indicated that MYT1L downregulated the expression of genes related to stem cell proliferation, thus confirming the results from earlier proliferation assays. One important gene that was downregulated in the two cell lines upon MYT1L overexpression was YAP1. As a member of the Hippo pathway, YAP1 has been described to promote growth and is also abnormally elevated in gliomas (Liu and Wang 2015). Hence, YAP1 potentially represents a MYT1L downstream target that is responsible for the tumor-suppressing effects presented in this study. This was further supported by previous findings, where overexpression of MYT1L reduced proliferation in GBM cells by directly repressing YAP1 (Melhuish et al. 2018). YAP1 acts as a transcription co-activator of target transcription factors, such as the TEAD family, and has been implicated as an oncogene (Zhao et al. 2011). These findings presented the Hippo pathway as a promising therapeutic target In GBM (Zhang et al., 2016). Notably, the FDA-approved small molecule NSC682769 inhibits the interaction of YAP1-TEAD1 and by this reduces migration, invasion, proliferation and colony formation in GBM cell lines, and increase survival in GBM mouse models (Saunders et al. 2021). The FDA-approved small molecule inhibitor Verteporfin also targets the YAP1-TEAD1 interaction and has shown remarkable preclinical results by impairing tumor invasion and enabling survival benefits in PDX mouse models (Barrette et al. 2022). These preclinical results highlight the importance of YAP1 in brain tumor progression and indicate that MYT1L might reduce these features via direct downregulation of YAP1.

5.5 MYT1L - a potential master regulator of NPC-like GBM subtypes

Globally and across all cancer types, I found MYT1L expression to be significantly decreased in GBM and LGG. However, it must be noted that the expression of MYT1L in the different cancer tissues was compared to “normal” surrounding tissue of the respective organs. The fact that MYT1L is highly and exclusively expressed in neurons of the brain and the peripheral nervous system could explain why expression levels in brain tumors, being composed of heterogenous cell types, are significantly decreased. Consequently, the decreased MYT1L levels in GBM and LGG might not indicate a role of MYT1L in brain tumors but rather show decreased number or neurons in bulk tumor tissues.

Focusing on MYT1L expression levels in brain cancers specifically, I found MYT1L to be expressed most highly in glioma, GBM, medulloblastomas and autologous nervous system tumors originating from the neural crest, such as neuroblastoma. In the case of GBM, higher MYT1L levels correlate with better survival, although these results were not significant. Interestingly, I found MYT1L to be expressed highest within the proneural subgroup of the Verhaak classification, the subgroup with the best outcome. Based on these findings, I also investigated the MYT1L expression in the more

recent subtype classification of Neftel et. al (2019), which more accurately represents the biological situation, rather than strictly separating into distinct subtypes. In this framework, cells can switch between the cellular states NPC1/2, MES1/2, OPC and AC and coexist within the same tumor with varying frequencies, influenced by the microenvironment with certain mutations and copy number variations favoring a certain state. By analyzing this dataset with the help of Bryce Lim (DKFZ Heidelberg), I found MYT1L to be almost exclusively expressed in the NPC2-like cell state. This indicated MYT1L as a potential GBM subtype marker.

In addition to the possibility that MYT1L may function as a subtype specific GBM marker, and given its effects on proliferation and invasion, MYT1L may also play an active role in driving subtype identity. This could represent a mechanism by which MYT1L reduces the malignant features of GBM by shifting cell states from more aggressive MES-like cell states towards prognostically favorable NPC-like cell states.
To explore this possibility, transcriptomic data of the S24 and P3XX PDGC lines, sharing many features of the mesenchymal subtype, were analyzed upon MYT1L overexpression to compare these samples to Wang/Verhaak subtype scores and Neftel cell state scores based on their gene expression (Neftel et al. 2019; Wang et al. 2017). The NPC1- and NPC2-like cell state scores as well as the proneural subtype scores were increased for both cell lines, whereas MES-like cell state scores were reduced after MYT1L overexpression. This shows that MYT1L can indeed shift the cell state from a mesenchymal state to the proneural/NPC-like state.

Remarkably, the inverse identity shift was observed upon knockdown of MYT1L in the BG5 PDGC line. While this cell line is mainly characterized by its NPC/proneural cell state (Hoffmann et al., unpublished data), depletion of MYT1L decreased the proneural subtype identity and increased the mesenchymal signature. The proneural to mesenchymal transition (PMT) in GBM is an equivalent process to the epithelial–mesenchymal transition (EMT) described in a variety of cancers, a key event driving invasion, aggressiveness and therapeutic resistance (Fedele et al. 2019). Therefore, understanding the mechanisms that could maintain the proneural subtype, prevent PMT or even enable transition towards the proneural subtype is highly relevant to improving the outcome and treatment strategies for GBM patients. Given the role of MYT1L in establishing and maintaining neuronal cell fate (Mall et al., 2017), I suggest that MYT1L could possibly maintain or even drive proneural/NPC-like cell state by preventing a shift towards mesenchymal signatures.

GBM identity shifts from proneural to mesenchymal subtypes could play an important role for patients, since the mesenchymal subtype is associated with a worse prognosis. In fact, tumors of

the mesenchymal subtype show high levels of tumor necrosis, increased invasiveness and enhanced migratory capacity (Joseph et al. 2015). This is in line with my observations, that MYT1L overexpression induced a shift away from the mesenchymal state accompanied with a lower degree of invasion. Furthermore, transcriptomic data revealed downregulation of gene programs related to cell motility and integrin signaling upon MYT1L overexpression. Integrins belong to the family of transmembrane adhesion receptors and have been found to activate signaling pathways, which regulate cell migration, invasion, proliferation, and survival (Ellert-Miklaszewska et al. 2020). The downregulation of integrin signaling may be one of the mechanisms underlying the decrease in cell migration and invasion induced by MYT1L *in vivo* and *in vitro*.

In summary, this part of my study showed that increasing MYT1L expression can shift patient-derived GBM cells away from a mesenchymal state towards a proneural or NPC-like state. In contrast, decreased MYT1L levels shifted NPC-like towards more mesenchymal-like signatures. However, more research is needed to explore the role of MYT1L in driving the proneural/NPC-like state. Investigation of the effects of MYT1L on subtype identity shifts and the accompanying changes in invasion, migration, and cell motility will allow identification of targets for future therapeutic intervention.

Based on the apparent transcriptomic plasticity of GBM, treatment strategies should consider the application of specific inhibitors of the mesenchymal phenotype or PMT to inhibit GBM progression. By elucidating potential mechanisms, downstream pathways, and target genes of MYT1L, this work provides exciting new insights and continuation points for ongoing glioma research. The characterization of MYT1L as a potential regulator of GBM subtype identity will hopefully lead to novel avenues for glioma therapy, to potentially lock glioma in a less infiltrative state and to find targeted treatments for specific subtypes.

6 REFERENCES

6. REFERENCES

Alcantara Llaguno, Sheila; Chen, Jian; Kwon, Chang-Hyuk; Jackson, Erica L.; Li, Yanjiao; Burns, Dennis K. et al. (2009): Malignant astrocytomas originate from neural stem/progenitor cells in a somatic tumor suppressor mouse model. In *Cancer cell* 15 (1), pp. 45–56. DOI: 10.1016/j.ccr.2008.12.006.

Alcantara Llaguno, Sheila; Sun, Daochun; Pedraza, Alicia M.; Vera, Elsa; Wang, Zilai; Burns, Dennis K.; Parada, Luis F. (2019): Cell-of-origin susceptibility to glioblastoma formation declines with neural lineage restriction. In *Nature neuroscience* 22 (4), pp. 545–555. DOI: 10.1038/s41593-018-0333-8.

Alcantara Llaguno, Sheila R.; Parada, Luis F. (2016): Cell of origin of glioma: biological and clinical implications. In *Br J Cancer* 115 (12), pp. 1445–1450. DOI: 10.1038/bjc.2016.354.

Aldape, Kenneth; Zadeh, Gelareh; Mansouri, Sheila; Reifenberger, Guido; Deimling, Andreas von (2015): Glioblastoma: pathology, molecular mechanisms and markers. In *Acta neuropathologica* 129 (6), pp. 829–848. DOI: 10.1007/s00401-015-1432-1.

Azzarelli, Roberta (2020): Organoid Models of Glioblastoma to Study Brain Tumor Stem Cells. In *Frontiers in Cell and Developmental Biology* 8, p. 220. DOI: 10.3389/fcell.2020.00220.

Barrette, Anne Marie; Ronk, Halle; Joshi, Tanvi; Mussa, Zarmeen; Mehrotra, Meenakshi; Bouras, Alexandros et al. (2022): Anti-invasive efficacy and survival benefit of the YAP-TEAD inhibitor verteporfin in preclinical glioblastoma models. In *Neuro-oncology* 24 (5), pp. 694–707. DOI: 10.1093/neuonc/noab244.

Behin, Anthony; Hoang-Xuan, Khe; Carpentier, Antoine F.; Delattre, Jean-Yves (2003): Primary brain tumours in adults. In *The Lancet* 361 (9354), pp. 323–331. DOI: 10.1016/S0140-6736(03)12328-8.

Belanich, M.; Randall, Terri; Pastor, Monica A.; Kibitel, Jeannie T.; Alas, Lori Green; Dolan, M. Eileen et al. (1996): Intracellular localization and intercellular heterogeneity of the human DNA repair protein O6-methylguanine-DNA methyltransferase. In *Cancer Chemotherapy and Pharmacology* 37 (6), pp. 547–555. DOI: 10.1007/s002800050427.

Berest, Ivan; Arnold, Christian; Reyes-Palomares, Armando; Palla, Giovanni; Rasmussen, Kasper Dindler; Giles, Holly et al. (2019): Quantification of Differential Transcription Factor Activity and Multiomics-Based Classification into Activators and Repressors: diffTF. In *Cell Reports* 29 (10), 3147-3159.e12. DOI: 10.1016/j.celrep.2019.10.106.

Berger, Shelley L. (2002): Histone modifications in transcriptional regulation. In *Current Opinion in Genetics & Development* 12 (2), pp. 142–148. DOI: 10.1016/S0959-437X(02)00279-4.

Besold, Angelique N.; Oluyadi, Abdulafeez A.; Michel, Sarah L. J. (2013): Switching metal ion coordination and DNA Recognition in a Tandem CCHHC-type zinc finger peptide. In *Inorganic chemistry* 52 (8), pp. 4721–4728.

Bhat, Krishna P.L.; Balasubramaniyan, Veerakumar; Vaillant, Brian; Ezhilarasan, Ravesanker; Hummelink, Karlijn; Hollingsworth, Faith et al. (2013): Mesenchymal Differentiation Mediated by NF-κB Promotes Radiation Resistance in Glioblastoma. In *Cancer cell* 24 (3), pp. 331–346. DOI: 10.1016/j.ccr.2013.08.001.

Bian, Shan; Repic, Marko; Guo, Zhenming; Kavirayani, Anoop; Burkard, Thomas; Bagley, Joshua A. et al. (2018): Author Correction: Genetically engineered cerebral organoids model brain tumor formation. In *Nat Methods* 15 (9), p. 748. DOI: 10.1038/s41592-018-0118-8.

Blanchet, Patricia; Bebin, Martina; Bruet, Shaam; Cooper, Gregory M.; Thompson, Michelle L.; Duban-Bedu, Benedicte et al. (2017): MYT1L mutations cause intellectual disability and variable obesity by dysregulating gene expression and development of the neuroendocrine hypothalamus. In *PLoS Genetics* 13 (8), e1006957. DOI: 10.1371/journal.pgen.1006957.

Board, P. G.; Coggan, M.; Chelvanayagam, G.; Easteal, S.; Jermiin, L. S.; Schulte, G. K. et al. (2000): Identification, characterization, and crystal structure of the Omega class glutathione transferases. In *The Journal of biological chemistry* 275 (32), pp. 24798–24806. DOI: 10.1074/jbc.M001706200.

Brat, Daniel J.; Castellano-Sanchez, Amilcar A.; Hunter, Stephen B.; Pecot, Marcia; Cohen, Cynthia; Hammond, Elizabeth H. et al. (2004): Pseudopalisades in glioblastoma are hypoxic, express extracellular matrix proteases, and are formed by an actively migrating cell population. In *Cancer research* 64 (3), pp. 920–927. DOI: 10.1158/0008-5472.CAN-03-2073.

Brennan, Cameron W.; Verhaak, Roel G. W.; McKenna, Aaron; Campos, Benito; Noushmehr, Houtan; Salama, Sofie R. et al. (2013): The somatic genomic landscape of glioblastoma. In *Cell* 155 (2), pp. 462–477. DOI: 10.1016/j.cell.2013.09.034.

Caldwell, Andrew B.; Liu, Qing; Schroth, Gary P.; Galasko, Douglas R.; Yuan, Shauna H.; Wagner, Steven L.; Subramaniam, Shankar: Dedifferentiation and neuronal repression define familial Alzheimer's disease. In *Science advances* 6 (46), eaba5933. DOI: 10.1126/sciadv.aba5933.

Cardoso-Moreira, Margarida; Halbert, Jean; Valloton, Delphine; Velten, Britta; Chen, Chunyan; Shao, Yi et al. (2019): Gene expression across mammalian organ development. In *Nature* 571 (7766), pp. 505–509.

Chen, Jiayang; Lambo, Mary E.; Ge, Xia; Dearborn, Joshua T.; Liu, Yating; McCullough, Katherine B. et al. (2021): A MYT1L syndrome mouse model recapitulates patient phenotypes and reveals altered brain development due to disrupted neuronal maturation. In *Neuron* 109 (23), 3775-3792.e14. DOI: 10.1016/j.neuron.2021.09.009.

Chen, Jiayang; Yen, Allen; Florian, Colin P.; Dougherty, Joseph D. (2022): MYT1L in the making: emerging insights on functions of a neurodevelopmental disorder gene. In *Translational psychiatry* 12 (1), p. 292. DOI: 10.1038/s41398-022-02058-x.

Chiang, Gary G.; Abraham, Robert T. (2007): Targeting the mTOR signaling network in cancer. In *Trends in molecular medicine* 13 (10), pp. 433–442.

Clement, Virginie; Sanchez, Pilar; Tribolet, Nicolas de; Radovanovic, Ivan; Ruiz i Altaba, Ariel (2007): HEDGEHOG-GLI1 signaling regulates human glioma growth, cancer stem cell self-renewal, and tumorigenicity. In *Current biology : CB* 17 (2), pp. 165–172. DOI: 10.1016/j.cub.2006.11.033.

D'Mello, Santosh R. (2019): Regulation of central nervous system development by class I histone deacetylases. In *Developmental neuroscience* 41 (3), pp. 149–165.

Dasari, Sreenivasulu; Gonuguntla, Sailaja; Ganjayi, Muni Swamy; Bukke, Suman; Sreenivasulu, Basha; Meriga, Balaji (2018): Genetic polymorphism of glutathione S-transferases: Relevance to neurological disorders. In *Pathophysiology : the official journal of the International Society for Pathophysiology* 25 (4), pp. 285–292. DOI: 10.1016/j.pathophys.2018.06.001.

Dobin, Alexander; Davis, Carrie A.; Schlesinger, Felix; Drenkow, Jorg; Zaleski, Chris; Jha, Sonali et al. (2013): STAR: ultrafast universal RNA-seq aligner. In *Bioinformatics (Oxford, England)* 29 (1), pp. 15–21. DOI: 10.1093/bioinformatics/bts635.

Drápela, Stanislav; Bouchal, Jan; Jolly, Mohit Kumar; Culig, Zoran; Souček, Karel (2020): ZEB1: a critical regulator of cell plasticity, DNA damage response, and therapy resistance. In *Frontiers in molecular biosciences* 7, p. 36.

Eder, Katalin; Kalman, Bernadette (2014): Molecular heterogeneity of glioblastoma and its clinical relevance. In *Pathology & Oncology Research* 20 (4), pp. 777–787.

Ellert-Miklaszewska, Aleksandra; Poleszak, Katarzyna; Pasierbinska, Maria; Kaminska, Bozena (2020): Integrin Signaling in Glioma Pathogenesis: From Biology to Therapy. In *International journal of molecular sciences* 21 (3). DOI: 10.3390/ijms21030888.

Fedele, Monica; Cerchia, Laura; Pegoraro, Silvia; Sgarra, Riccardo; Manfioletti, Guidalberto (2019): Proneural-Mesenchymal Transition: Phenotypic Plasticity to Acquire Multitherapy Resistance in Glioblastoma. In *International journal of molecular sciences* 20 (11). DOI: 10.3390/ijms20112746.

Friedmann-Morvinski, Dinorah; Bushong, Eric A.; Ke, Eugene; Soda, Yasushi; Marumoto, Tomotoshi; Singer, Oded et al. (2012): Dedifferentiation of neurons and astrocytes by oncogenes can induce gliomas in mice. In *Science* 338 (6110), pp. 1080–1084. DOI: 10.1126/science.1226929.

Ganguly, Anutosh; Yang, Hailing; Zhang, Hong; Cabral, Fernando; Patel, Kamala D. (2013): Microtubule Dynamics Control Tail Retraction in Migrating Vascular Endothelial CellsSuppressing Microtubule Dynamics Blocks HUVEC Migration. In *Molecular cancer therapeutics* 12 (12), pp. 2837–2846.

Gómez-Oliva, Ricardo; Domínguez-García, Samuel; Carrascal, Livia; Abalos-Martínez, Jessica; Pardillo-Díaz, Ricardo; Verástegui, Cristina et al. (2021): Evolution of Experimental Models in the Study of Glioblastoma: Toward Finding Efficient Treatments. In *Frontiers in Oncology* 10. Available online at https://www.frontiersin.org/articles/10.3389/fonc.2020.614295.

Gu, Jinhai; Li, Gang; Sun, Tao; Su, Yuhang; Zhang, Xulong; Shen, Jie et al. (2008): Blockage of the STAT3 signaling pathway with a decoy oligonucleotide suppresses growth of human malignant glioma cells. In *Journal of neuro-oncology* 89 (1), pp. 9–17. DOI: 10.1007/s11060-008-9590-9.

Guo, G.; Sun, Y.; Hong, R.; Xiong, J.; Lu, Y.; Liu, Y. et al. (2020): IKBKE enhances TMZ-chemoresistance through upregulation of MGMT expression in glioblastoma. In *Clin Transl Oncol* 22 (8), pp. 1252–1262. DOI: 10.1007/s12094-019-02251-3.

Gupta, Piyush B.; Pastushenko, Ievgenia; Skibinski, Adam; Blanpain, Cedric; Kuperwasser, Charlotte (2019): Phenotypic Plasticity: Driver of Cancer Initiation, Progression, and Therapy Resistance. In *Cell Stem Cell* 24 (1), pp. 65–78. DOI: 10.1016/j.stem.2018.11.011.

Han, Sue; Liu, Yang; Cai, Sabrina J.; Qian, Mingyu; Ding, Jianyi; Larion, Mioara et al. (2020): IDH mutation in glioma: molecular mechanisms and potential therapeutic targets. In *Br J Cancer* 122 (11), pp. 1580–1589. DOI: 10.1038/s41416-020-0814-x.

Hanahan, Douglas (2022): Hallmarks of Cancer: New Dimensions. In *Cancer Discov* 12 (1), pp. 31–46. DOI: 10.1158/2159-8290.CD-21-1059.

Hanahan, Douglas; Weinberg, Robert A. (2000): The hallmarks of cancer. In *Cell* 100 (1), pp. 57–70.

Hanahan, Douglas; Weinberg, Robert A. (2011): Hallmarks of cancer: the next generation. In *Cell* 144 (5), pp. 646–674.

Hausmann, David; Hoffmann, Dirk C.; Venkataramani, Varun; Jung, Erik; Horschitz, Sandra; Tetzlaff, Svenja K. et al. (2022): Autonomous rhythmic activity in glioma networks drives brain tumour growth. In *Nature*. DOI: 10.1038/s41586-022-05520-4.

Hegi, Monika E.; Diserens, Annie-Claire; Gorlia, Thierry; Hamou, Marie-France; Tribolet, Nicolas de; Weller, Michael et al. (2005): MGMT Gene Silencing and Benefit from Temozolomide in Glioblastoma. In *New England Journal of Medicine* 352 (10), pp. 997–1003. DOI: 10.1056/NEJMoa043331.

Henrik Heiland, Dieter; Ravi, Vidhya M.; Behringer, Simon P.; Frenking, Jan Hendrik; Wurm, Julian; Joseph, Kevin et al. (2019): Tumor-associated reactive astrocytes aid the evolution of immunosuppressive environment in glioblastoma. In *Nature Communications* 10 (1), p. 2541. DOI: 10.1038/s41467-019-10493-6.

Hu, Jian; Ho, Allen L.; Yuan, Liang; Hu, Baoli; Hua, Sujun; Hwang, Soyoon Sarah et al. (2013): Neutralization of terminal differentiation in gliomagenesis. In *Proceedings of the National Academy of Sciences* 110 (36), p. 14520. DOI: 10.1073/pnas.1308610110.

Huang, Jianbin; Wu, Shian; Barrera, Jose; Matthews, Krista; Pan, Duojia (2005): The Hippo signaling pathway coordinately regulates cell proliferation and apoptosis by inactivating Yorkie, the Drosophila Homolog of YAP. In *Cell* 122 (3), pp. 421–434. DOI: 10.1016/j.cell.2005.06.007.

Huang, Tianzhi; Song, Xiao; Xu, Dandan; Tiek, Deanna; Goenka, Anshika; Wu, Bingli et al. (2020): Stem cell programs in cancer initiation, progression, and therapy resistance. In *Theranostics* 10 (19), pp. 8721–8743. DOI: 10.7150/thno.41648.

Huse, Jason T.; Phillips, Heidi S.; Brennan, Cameron W. (2011): Molecular subclassification of diffuse gliomas: seeing order in the chaos. In *Glia* 59 (8), pp. 1190–1199. DOI: 10.1002/glia.21165.

Jackson, Kasey L.; Dayton, Robert D.; Deverman, Benjamin E.; Klein, Ronald L. (2016): Better Targeting, Better Efficiency for Wide-Scale Neuronal Transduction with the Synapsin Promoter and AAV-PHP.B. In *Frontiers in molecular neuroscience* 9, p. 116. DOI: 10.3389/fnmol.2016.00116.

Jankowsky, Joanna L.; Zheng, Hui (2017): Practical considerations for choosing a mouse model of Alzheimer's disease. In *Molecular neurodegeneration* 12 (1), p. 89. DOI: 10.1186/s13024-017-0231-7.

Joseph, Justin V.; Conroy, Siobhan; Pavlov, Kirill; Sontakke, Pallavi; Tomar, Tushar; Eggens-Meijer, Ellie et al. (2015): Hypoxia enhances migration and invasion in glioblastoma by promoting a mesenchymal shift mediated by the HIF1α–ZEB1 axis. In *Cancer Letters* 359 (1), pp. 107–116. DOI: 10.1016/j.canlet.2015.01.010.

Jung, Erik; Osswald, Matthias; Blaes, Jonas; Wiestler, Benedikt; Sahm, Felix; Schmenger, Torsten et al. (2017): Tweety-Homolog 1 Drives Brain Colonization of Gliomas. In *The Journal of Neuroscience* 37 (29), p. 6837. DOI: 10.1523/JNEUROSCI.3532-16.2017.

Jung, Erik; Osswald, Matthias; Ratliff, Miriam; Dogan, Helin; Xie, Ruifan; Weil, Sophie et al. (2021): Tumor cell plasticity, heterogeneity, and resistance in crucial microenvironmental niches in glioma. In *Nature Communications* 12 (1), p. 1014. DOI: 10.1038/s41467-021-21117-3.

Kameyama, Toshiki; Matsushita, Fumio; Kadokawa, Yuzo; Marunouchi, Tohru (2011): Myt/NZF family transcription factors regulate neuronal differentiation of P19 cells. In *Neuroscience letters* 497 (2), pp. 74–79.

Karzbrun, Eyal; Kshirsagar, Aditya; Cohen, Sidney R.; Hanna, Jacob H.; Reiner, Orly (2018): Human Brain Organoids on a Chip Reveal the Physics of Folding. In *Nature physics* 14 (5), pp. 515–522. DOI: 10.1038/s41567-018-0046-7.

Kaufman, Charles K.; Mosimann, Christian; Fan, Zi Peng; Yang, Song; Thomas, Andrew J.; Ablain, Julien et al. (2016): A zebrafish melanoma model reveals emergence of neural crest identity during melanoma initiation. In *Science* 351 (6272), aad2197. DOI: 10.1126/science.aad2197.

Kepa, Agnieszka; Martinez Medina, Lourdes; Erk, Susanne; Srivastava, Deepak P.; Fernandes, Alinda; Toro, Roberto et al. (2017): Associations of the intellectual disability gene MYT1L with helix–loop–helix gene expression, hippocampus volume and hippocampus activation during memory retrieval. In *Neuropsychopharmacology* 42 (13), pp. 2516–2526.

Kim, Hyun Jung; Park, Jung Won; Lee, Jeong Ho (2020): Genetic Architectures and Cell-of-Origin in Glioblastoma. In *Frontiers in Oncology* 10, p. 615400. DOI: 10.3389/fonc.2020.615400.

Kim, Seongbin; Oh, Hyoseon; Choi, Sang Han; Yoo, Ye-Eun; Noh, Young Woo; Cho, Yisul et al. (2022): Postnatal age-differential ASD-like transcriptomic, synaptic, and behavioral deficits in Myt1l-mutant mice. In *Cell Reports* 40 (12), p. 111398. DOI: 10.1016/j.celrep.2022.111398.

Kim, Yona; Varn, Frederick S.; Park, Sung-Hye; Yoon, Byung Woo; Park, Hye Ran; Lee, Charles et al. (2021): Perspective of mesenchymal transformation in glioblastoma. In *Acta Neuropathologica Communications* 9 (1), p. 50. DOI: 10.1186/s40478-021-01151-4.

Klughammer, Johanna; Kiesel, Barbara; Roetzer, Thomas; Fortelny, Nikolaus; Nemc, Amelie; Nenning, Karl-Heinz et al. (2018): The DNA methylation landscape of glioblastoma disease progression shows extensive heterogeneity in time and space. In *Nature medicine* 24 (10), pp. 1611–1624.

Krefft, Olivia; Jabali, Ammar; Iefremova, Vira; Koch, Philipp; Ladewig, Julia (2018): Generation of Standardized and Reproducible Forebrain-type Cerebral Organoids from Human Induced Pluripotent Stem Cells. In *Journal of visualized experiments : JoVE* (131). DOI: 10.3791/56768.

Kuleshov, Maxim V.; Jones, Matthew R.; Rouillard, Andrew D.; Fernandez, Nicolas F.; Duan, Qiaonan; Wang, Zichen et al. (2016): Enrichr: a comprehensive gene set enrichment analysis web server 2016 update. In *Nucleic acids research* 44 (W1), W90-7. DOI: 10.1093/nar/gkw377.

Lancaster, Madeline A.; Knoblich, Juergen A. (2014): Generation of cerebral organoids from human pluripotent stem cells. In *Nature protocols* 9 (10), pp. 2329–2340. DOI: 10.1038/nprot.2014.158.

Lancaster, Madeline A.; Renner, Magdalena; Martin, Carol-Anne; Wenzel, Daniel; Bicknell, Louise S.; Hurles, Matthew E. et al. (2013): Cerebral organoids model human brain development and microcephaly. In *Nature* 501 (7467), pp. 373–379. DOI: 10.1038/nature12517.

Lawrence, Michael S.; Stojanov, Petar; Mermel, Craig H.; Robinson, James T.; Garraway, Levi A.; Golub, Todd R. et al. (2014): Discovery and saturation analysis of cancer genes across 21 tumour types. In *Nature* 505 (7484), pp. 495–501. DOI: 10.1038/nature12912.

Lee, Laura J.; Papadopoli, David; Jewer, Michael; Del Rincon, Sonia; Topisirovic, Ivan; Lawrence, Mitchell G.; Postovit, Lynne-Marie (2021): Cancer Plasticity: The Role of mRNA Translation. In *Trends in Cancer* 7 (2), pp. 134–145. DOI: 10.1016/j.trecan.2020.09.005.

Li, Fei; Qi, Bing; Le Yang; Wang, Bao; Gao, Li; Zhao, Minggao; Luo, Lanxin (2022): CHI3L1 predicted in malignant entities is associated with glioblastoma immune microenvironment. In *Clinical immunology (Orlando, Fla.)* 245, p. 109158. DOI: 10.1016/j.clim.2022.109158.

Liu, Yong-Chang; Wang, Yan-zhou (2015): Role of Yes-associated protein 1 in gliomas: pathologic and therapeutic aspects. In *Tumor Biology* 36 (4), pp. 2223–2227. DOI: 10.1007/s13277-015-3297-2.

Liu, Yunpeng; Shi, Ning; Regev, Aviv; He, Shan; Hemann, Michael T. (2020): Integrated regulatory models for inference of subtype-specific susceptibilities in glioblastoma. In *Mol. Syst. Biol.* 16 (9), e9506. DOI: 10.15252/msb.20209506.

Lo, Hui-Wen; Zhu, Hu; Cao, Xinyu; Aldrich, Amy; Ali-Osman, Francis (2009): A novel splice variant of GLI1 that promotes glioblastoma cell migration and invasion. In *Cancer research* 69 (17), pp. 6790–6798. DOI: 10.1158/0008-5472.CAN-09-0886.

Louis, David N.; Ohgaki, Hiroko; Wiestler, Otmar D.; Cavenee, Webster K.; Burger, Peter C.; Jouvet, Anne et al. (2007): The 2007 WHO classification of tumours of the central nervous system. In *Acta neuropathologica* 114 (2), pp. 97–109. DOI: 10.1007/s00401-007-0243-4.

Louis, David N.; Perry, Arie; Reifenberger, Guido; Deimling, Andreas von; Figarella-Branger, Dominique; Cavenee, Webster K. et al. (2016): The 2016 World Health Organization Classification of Tumors of the Central Nervous System: a summary. In *Acta neuropathologica* 131 (6), pp. 803–820. DOI: 10.1007/s00401-016-1545-1.

Love, Michael I.; Huber, Wolfgang; Anders, Simon (2014): Moderated estimation of fold change and dispersion for RNA-seq data with DESeq2. In *Genome biology* 15 (12), p. 550. DOI: 10.1186/s13059-014-0550-8.

Lu, Jie; Yang, Yi; Guo, Gaochao; Liu, Yang; Zhang, Zhimeng; Dong, Shicai et al. (2017): IKBKE regulates cell proliferation and epithelial-mesenchymal transition of human malignant glioma via the Hippo pathway. In *Oncotarget* 8 (30), pp. 49502–49514. DOI: 10.18632/oncotarget.17738.

Mall, Moritz; Kareta, Michael S.; Chanda, Soham; Ahlenius, Henrik; Perotti, Nicholas; Zhou, Bo et al. (2017): Myt1l safeguards neuronal identity by actively repressing many non-neuronal fates. In *Nature* 544 (7649), pp. 245–249. DOI: 10.1038/nature21722.

Mansfield, Patricia; Constantino, John N.; Baldridge, Dustin (2020): MYT1L: A systematic review of genetic variation encompassing schizophrenia and autism. In *American journal of medical genetics. Part B, Neuropsychiatric genetics : the official publication of the International Society of Psychiatric Genetics* 183 (4), pp. 227–233. DOI: 10.1002/ajmg.b.32781.

Manukyan, Arkadi; Kowalczyk, Izabela; Melhuish, Tiffany A.; Lemiesz, Agata; Wotton, David (2018): Analysis of transcriptional activity by the Myt1 and Myt1l transcription factors. In *Journal of cellular biochemistry* 119 (6), pp. 4644–4655.

Marques, Carolina; Unterkircher, Thomas; Kroon, Paula; Oldrini, Barbara; Izzo, Annalisa; Dramaretska, Yuliia et al. (2021): NF1 regulates mesenchymal glioblastoma plasticity and aggressiveness through the AP-1 transcription factor FOSL1. In *eLife* 10. DOI: 10.7554/eLife.64846.

Matsushita, Fumio; Kameyama, Toshiki; Kadokawa, Yuzo; Marunouchi, Tohru (2014): Spatiotemporal expression pattern of Myt/NZF family zinc finger transcription factors during mouse nervous system development. In *Developmental Dynamics* 243 (4), pp. 588–600.

Melhuish, Tiffany A.; Kowalczyk, Izabela; Manukyan, Arkadi; Zhang, Ying; Shah, Anant; Abounader, Roger; Wotton, David (2018): Myt1 and Myt1l transcription factors limit proliferation in GBM cells by repressing

YAP1 expression. In *Biochimica et biophysica acta. Gene regulatory mechanisms* 1861 (11), pp. 983–995. DOI: 10.1016/j.bbagrm.2018.10.005.

Meng, Zhipeng; Moroishi, Toshiro; Guan, Kun-Liang (2016): Mechanisms of Hippo pathway regulation. In *Genes & development* 30 (1), pp. 1–17. DOI: 10.1101/gad.274027.115.

Mignone, John L.; Kukekov, Valery; Chiang, Ann-Shyn; Steindler, Dennis; Enikolopov, Grigori (2004): Neural stem and progenitor cells in nestin-GFP transgenic mice. In *The Journal of comparative neurology* 469 (3), pp. 311–324. DOI: 10.1002/cne.10964.

Miller, Kimberly D.; Ostrom, Quinn T.; Kruchko, Carol; Patil, Nirav; Tihan, Tarik; Cioffi, Gino et al. (2021): Brain and other central nervous system tumor statistics, 2021. In *CA A Cancer J Clin* 71 (5), pp. 381–406. DOI: 10.3322/caac.21693.

Mills, Jason C.; Stanger, Ben Z.; Sander, Maike (2019): Nomenclature for cellular plasticity: are the terms as plastic as the cells themselves? In *The EMBO journal* 38 (19), e103148. DOI: 10.15252/embj.2019103148.

Miyai, Masafumi; Tomita, Hiroyuki; Soeda, Akio; Yano, Hirohito; Iwama, Toru; Hara, Akira (2017): Current trends in mouse models of glioblastoma. In *J Neurooncol* 135 (3), pp. 423–432. DOI: 10.1007/s11060-017-2626-2.

Neftel, Cyril; Laffy, Julie; Filbin, Mariella G.; Hara, Toshiro; Shore, Marni E.; Rahme, Gilbert J. et al. (2019): An Integrative Model of Cellular States, Plasticity, and Genetics for Glioblastoma. In *Cell* 178 (4), 835-849.e21. DOI: 10.1016/j.cell.2019.06.024.

Ogawa, Junko; Pao, Gerald M.; Shokhirev, Maxim N.; Verma, Inder M. (2018): Glioblastoma Model Using Human Cerebral Organoids. In *Cell Reports* 23 (4), pp. 1220–1229. DOI: 10.1016/j.celrep.2018.03.105.

Osswald, Matthias; Jung, Erik; Sahm, Felix; Solecki, Gergely; Venkataramani, Varun; Blaes, Jonas et al. (2015): Brain tumour cells interconnect to a functional and resistant network. In *Nature* 528 (7580), pp. 93–98. DOI: 10.1038/nature16071.

Overholtzer, Michael; Zhang, Jianmin; Smolen, Gromoslaw A.; Muir, Beth; Li, Wenmei; Sgroi, Dennis C. et al. (2006): Transforming properties of YAP, a candidate oncogene on the chromosome 11q22 amplicon. In *Proceedings of the National Academy of Sciences of the United States of America* 103 (33), pp. 12405–12410.

Ozawa, Tatsuya; Riester, Markus; Cheng, Yu-Kang; Huse, Jason T.; Squatrito, Massimo; Helmy, Karim et al. (2014): Most human non-GCIMP glioblastoma subtypes evolve from a common proneural-like precursor glioma. In *Cancer cell* 26 (2), pp. 288–300.

Pak, Changhui; Grieder, Sarah; Yang, Nan; Zhang, Yingsha; Wernig, Marius; Sudhof, Thomas (2018): Rapid generation of functional and homogeneous excitatory human forebrain neurons using Neurogenin-2 (Ngn2). In *Protocol Exchange*. DOI: 10.1038/protex.2018.082.

Papavassiliou, Kostas A.; Papavassiliou, Athanasios G. (2022): Transcription factors in glioblastoma – Molecular pathogenesis and clinical implications. In *Biochimica et Biophysica Acta (BBA) - Reviews on Cancer* 1877 (1), p. 188667. DOI: 10.1016/j.bbcan.2021.188667.

Parsons, D. Williams; Jones, Siân; Zhang, Xiaosong; Lin, Jimmy Cheng-Ho; Leary, Rebecca J.; Angenendt, Philipp et al. (2008): An integrated genomic analysis of human glioblastoma multiforme. In *Science* 321 (5897), pp. 1807–1812. DOI: 10.1126/science.1164382.

Patel, Anoop P.; Tirosh, Itay; Trombetta, John J.; Shalek, Alex K.; Gillespie, Shawn M.; Wakimoto, Hiroaki et al. (2014): Single-cell RNA-seq highlights intratumoral heterogeneity in primary glioblastoma. In *Science* 344 (6190), pp. 1396–1401.

Perekatt, Ansu O.; Shah, Pooja P.; Cheung, Shannon; Jariwala, Nidhi; Wu, Alex; Gandhi, Vishal et al. (2018): SMAD4 Suppresses WNT-Driven Dedifferentiation and Oncogenesis in the Differentiated Gut Epithelium. In *Cancer research* 78 (17), pp. 4878–4890. DOI: 10.1158/0008-5472.CAN-18-0043.

Phillips, Heidi S.; Kharbanda, Samir; Chen, Ruihuan; Forrest, William F.; Soriano, Robert H.; Wu, Thomas D. et al. (2006): Molecular subclasses of high-grade glioma predict prognosis, delineate a pattern of disease progression, and resemble stages in neurogenesis. In *Cancer cell* 9 (3), pp. 157–173. DOI: 10.1016/j.ccr.2006.02.019.

Piao, Yuji; Liang, Ji; Henry, Verlene; Holmes, Lindsay; Groot, John F. de (2013): Abstract 1612: Targeting intercellular adhesion molecule-1 (ICAM-1) prolongs glioblastoma survival in combination with bevacizumab. In *Cancer research* 73 (8_Supplement), p. 1612. DOI: 10.1158/1538-7445.AM2013-1612.

Rogers, Geoffrey L.; Martino, Ashley T.; Aslanidi, George V.; Jayandharan, Giridhara R.; Srivastava, Arun; Herzog, Roland W. (2011): Innate Immune Responses to AAV Vectors. In *Frontiers in microbiology* 2, p. 194. DOI: 10.3389/fmicb.2011.00194.

Rosebrock, Daniel; Arora, Sneha; Mutukula, Naresh; Volkman, Rotem; Gralinska, Elzbieta; Balaskas, Anastasios et al. (2022): Enhanced cortical neural stem cell identity through short SMAD and WNT inhibition in human cerebral organoids facilitates emergence of outer radial glial cells. In *Nature cell biology* 24 (6), pp. 981–995. DOI: 10.1038/s41556-022-00929-5.

Sandmann, Thomas; Bourgon, Richard; Garcia, Josep; Li, Congfen; Cloughesy, Timothy; Chinot, Olivier L. et al. (2015): Patients With Proneural Glioblastoma May Derive Overall Survival Benefit From the Addition of Bevacizumab to First-Line Radiotherapy and Temozolomide: Retrospective Analysis of the AVAglio Trial. In *J Clin Oncol* 33 (25), pp. 2735–2744. DOI: 10.1200/JCO.2015.61.5005.

Santoni, Matteo; Burattini, Luciano; Nabissi, Massimo; Morelli, Maria Beatrice; Berardi, Rossana; Santoni, Giorgio; Cascinu, Stefano (2013): Essential role of Gli proteins in glioblastoma multiforme. In *Current protein & peptide science* 14 (2), pp. 133–140. DOI: 10.2174/1389203711314020005.

Saunders, Jacquelyn T.; Holmes, Brent; Benavides-Serrato, Angelica; Kumar, Sunil; Nishimura, Robert N.; Gera, Joseph (2021): Targeting the YAP-TEAD interaction interface for therapeutic intervention in glioblastoma. In *J Neurooncol* 152 (2), pp. 217–231. DOI: 10.1007/s11060-021-03699-6.

Schönrock, Anna; Heinzelmann, Elisa; Steffl, Bianca; Demirdizen, Engin; Narayanan, Ashwin; Krunic, Damir et al. (2022): MEOX2 homeobox gene promotes growth of malignant gliomas. In *Neuro-oncology* 24 (11), pp. 1911–1924. DOI: 10.1093/neuonc/noac110.

Shafi, Ovais; Siddiqui, Ghazia (2022): Tracing the origins of glioblastoma by investigating the role of gliogenic and related neurogenic genes/signaling pathways in GBM development: a systematic review. In *World Journal of Surgical Oncology* 20 (1), p. 146. DOI: 10.1186/s12957-022-02602-5.

Shen, Shensi; Clairambault, Jean (2020): Cell plasticity in cancer cell populations. In *F1000Research* 9. DOI: 10.12688/f1000research.24803.1.

Sidaway, Peter (2017): Glioblastoma subtypes revisited. In *Nature Reviews Clinical Oncology* 14 (10), p. 587. DOI: 10.1038/nrclinonc.2017.122.

Stupp, Roger; Hegi, Monika E.; Mason, Warren P.; van den Bent, Martin J.; Taphoorn, Martin J. B.; Janzer, Robert C. et al. (2009): Effects of radiotherapy with concomitant and adjuvant temozolomide versus radiotherapy alone on survival in glioblastoma in a randomised phase III study: 5-year analysis of the EORTC-NCIC trial. In *The Lancet. Oncology* 10 (5), pp. 459–466. DOI: 10.1016/S1470-2045(09)70025-7.

Stupp, Roger; Mason, Warren P.; van den Bent, Martin J.; Weller, Michael; Fisher, Barbara; Taphoorn, Martin J.B. et al. (2005): Radiotherapy plus Concomitant and Adjuvant Temozolomide for Glioblastoma. In *New England Journal of Medicine* 352 (10), pp. 987–996. DOI: 10.1056/NEJMoa043330.

Stupp, Roger; Taillibert, Sophie; Kanner, Andrew; Read, William; Steinberg, David M.; Lhermitte, Benoit et al. (2017): Effect of tumor-treating fields plus maintenance temozolomide vs maintenance temozolomide alone on survival in patients with glioblastoma: a randomized clinical trial. In *Jama* 318 (23), pp. 2306–2316.

Venkataramani, Varun; Schneider, Matthias; Giordano, Frank Anton; Kuner, Thomas; Wick, Wolfgang; Herrlinger, Ulrich; Winkler, Frank (2022): Disconnecting multicellular networks in brain tumours. In *Nature reviews. Cancer* 22 (8), pp. 481–491. DOI: 10.1038/s41568-022-00475-0.

Verhaak, Roel G. W.; Hoadley, Katherine A.; Purdom, Elizabeth; Wang, Victoria; Qi, Yuan; Wilkerson, Matthew D. et al. (2010): Integrated genomic analysis identifies clinically relevant subtypes of glioblastoma characterized by abnormalities in PDGFRA, IDH1, EGFR, and NF1. In *Cancer cell* 17 (1), pp. 98–110. DOI: 10.1016/j.ccr.2009.12.020.

Vierbuchen, Thomas; Ostermeier, Austin; Pang, Zhiping P.; Kokubu, Yuko; Südhof, Thomas C.; Wernig, Marius (2010): Direct conversion of fibroblasts to functional neurons by defined factors. In *Nature* 463 (7284), pp. 1035–1041.

Vishnoi, Kanchan; Viswakarma, Navin; Rana, Ajay; Rana, Basabi (2020): Transcription Factors in Cancer Development and Therapy. In *Cancers* 12 (8). DOI: 10.3390/cancers12082296.

Visser, Otto; Ardanaz, Eva; Botta, Laura; Sant, Milena; Tavilla, Andrea; Minicozzi, Pamela (2015): Survival of adults with primary malignant brain tumours in Europe; Results of the EUROCARE-5 study. In *European journal of cancer (Oxford, England : 1990)* 51 (15), pp. 2231–2241. DOI: 10.1016/j.ejca.2015.07.032.

Visvader, Jane E. (2011): Cells of origin in cancer. In *Nature* 469 (7330), pp. 314–322.

Wang, Haopeng; Mao, Xiang; Ye, Lei; Cheng, Hongwei; Dai, Xingliang (2022a): The Role of the S100 Protein Family in Glioma. In *J. Cancer* 13 (10), pp. 3022–3030. DOI: 10.7150/jca.73365.

Wang, Qianghu; Hu, Baoli; Hu, Xin; Kim, Hoon; Squatrito, Massimo; Scarpace, Lisa et al. (2017): Tumor Evolution of Glioma-Intrinsic Gene Expression Subtypes Associates with Immunological Changes in the Microenvironment. In *Cancer cell* 32 (1), 42-56.e6. DOI: 10.1016/j.ccell.2017.06.003.

Wang, Xinjun; Zhang, Chunzhao; Szábo, Gábor; Sun, Qian-Quan (2013): Distribution of CaMKIIα expression in the brain in vivo, studied by CaMKIIα-GFP mice. In *Brain research* 1518, pp. 9–25. DOI: 10.1016/j.brainres.2013.04.042.

Wang, Xinyue; Liang, Jianhao; Sun, Haitao (2022b): The Network of Tumor Microtubes: An Improperly Reactivated Neural Cell Network With Stemness Feature for Resistance and Recurrence in Gliomas. In *Frontiers in Oncology* 12, p. 921975. DOI: 10.3389/fonc.2022.921975.

Weller, Michael; Butowski, Nicholas; Tran, David D.; Recht, Lawrence D.; Lim, Michael; Hirte, Hal et al. (2017): Rindopepimut with temozolomide for patients with newly diagnosed, EGFRvIII-expressing glioblastoma (ACT IV): a randomised, double-blind, international phase 3 trial. In *The Lancet. Oncology* 18 (10), pp. 1373–1385. DOI: 10.1016/S1470-2045(17)30517-X.

Wen, Patrick Y.; Weller, Michael; Lee, Eudocia Quant; Alexander, Brian M.; Barnholtz-Sloan, Jill S.; Barthel, Floris P. et al. (2020): Glioblastoma in adults: a Society for Neuro-Oncology (SNO) and European Society of Neuro-Oncology (EANO) consensus review on current management and future directions. In *Neuro-oncology* 22 (8), pp. 1073–1113. DOI: 10.1093/neuonc/noaa106.

Whyte, Warren A.; Orlando, David A.; Hnisz, Denes; Abraham, Brian J.; Lin, Charles Y.; Kagey, Michael H. et al. (2013): Master transcription factors and mediator establish super-enhancers at key cell identity genes. In *Cell* 153 (2), pp. 307–319. DOI: 10.1016/j.cell.2013.03.035.

Wick, Wolfgang; Kessler, Tobias (2018): New glioblastoma heterogeneity atlas—a shared resource. In *Nature Reviews Neurology* 14 (8), pp. 453–454.

Wöhr, Markus; Fong, Wendy M.; Janas, Justyna A.; Mall, Moritz; Thome, Christian; Vangipuram, Madhuri et al. (2022): Myt1l haploinsufficiency leads to obesity and multifaceted behavioral alterations in mice. In *Molecular autism* 13 (1), p. 19. DOI: 10.1186/s13229-022-00497-3.

Xiang Chaomei; Frietze Karla K.; Bi Yingtao; Li Yanwen; Dal Pozzo Valentina; Pal Sharmistha et al. (2021): RP58 Represses Transcriptional Programs Linked to Nonneuronal Cell Identity and Glioblastoma Subtypes in Developing Neurons. In *Molecular and Cellular Biology* 41 (7), e00526-20. DOI: 10.1128/MCB.00526-20.

Xiao, Yong; Wang, Zhen; Zhao, Mengjie; Deng, Yanxiang; Yang, Mingyu; Su, Graham et al. (2022): Single-Cell Transcriptomics Revealed Subtype-Specific Tumor Immune Microenvironments in Human Glioblastomas. In *Frontiers in immunology* 13, p. 914236. DOI: 10.3389/fimmu.2022.914236.

Xie, Qian; Mittal, Sandeep; Berens, Michael E. (2014): Targeting adaptive glioblastoma: an overview of proliferation and invasion. In *Neuro-oncology* 16 (12), pp. 1575–1584. DOI: 10.1093/neuonc/nou147.

Xu, Liang; Chen, Ye; Huang, Yulun; Sandanaraj, Edwin; Yu, John S.; Lin, Ruby Yu-Tong et al. (2021): Topography of transcriptionally active chromatin in glioblastoma. In *Science advances* 7 (18). DOI: 10.1126/sciadv.abd4676.

Yuan, Salina; Norgard, Robert J.; Stanger, Ben Z. (2019): Cellular Plasticity in Cancer. In *Cancer Discov* 9 (7), pp. 837–851. DOI: 10.1158/2159-8290.CD-19-0015.

Zglinicki, Thomas von; Wan, Tengfei; Miwa, Satomi (2021): Senescence in Post-Mitotic Cells: A Driver of Aging? In *Antioxidants & Redox Signaling* 34 (4), pp. 308–323. DOI: 10.1089/ars.2020.8048.

Zhao, Bin; Li, Li; Lu, Qing; Wang, Lloyd H.; Liu, Chen-Ying; Lei, Qunying; Guan, Kun-Liang (2011): Angiomotin is a novel Hippo pathway component that inhibits YAP oncoprotein. In *Genes & development* 25 (1), pp. 51–63. DOI: 10.1101/gad.2000111.

Zheng, Siyuan; Chheda, Milan G.; Verhaak, Roel G. W. (2012): Studying a complex tumor: potential and pitfalls. In *Cancer journal (Sudbury, Mass.)* 18 (1), pp. 107–114. DOI: 10.1097/PPO.0b013e3182431c57.

7. SUPPLEMENTS

7.1 Supplementary Figures

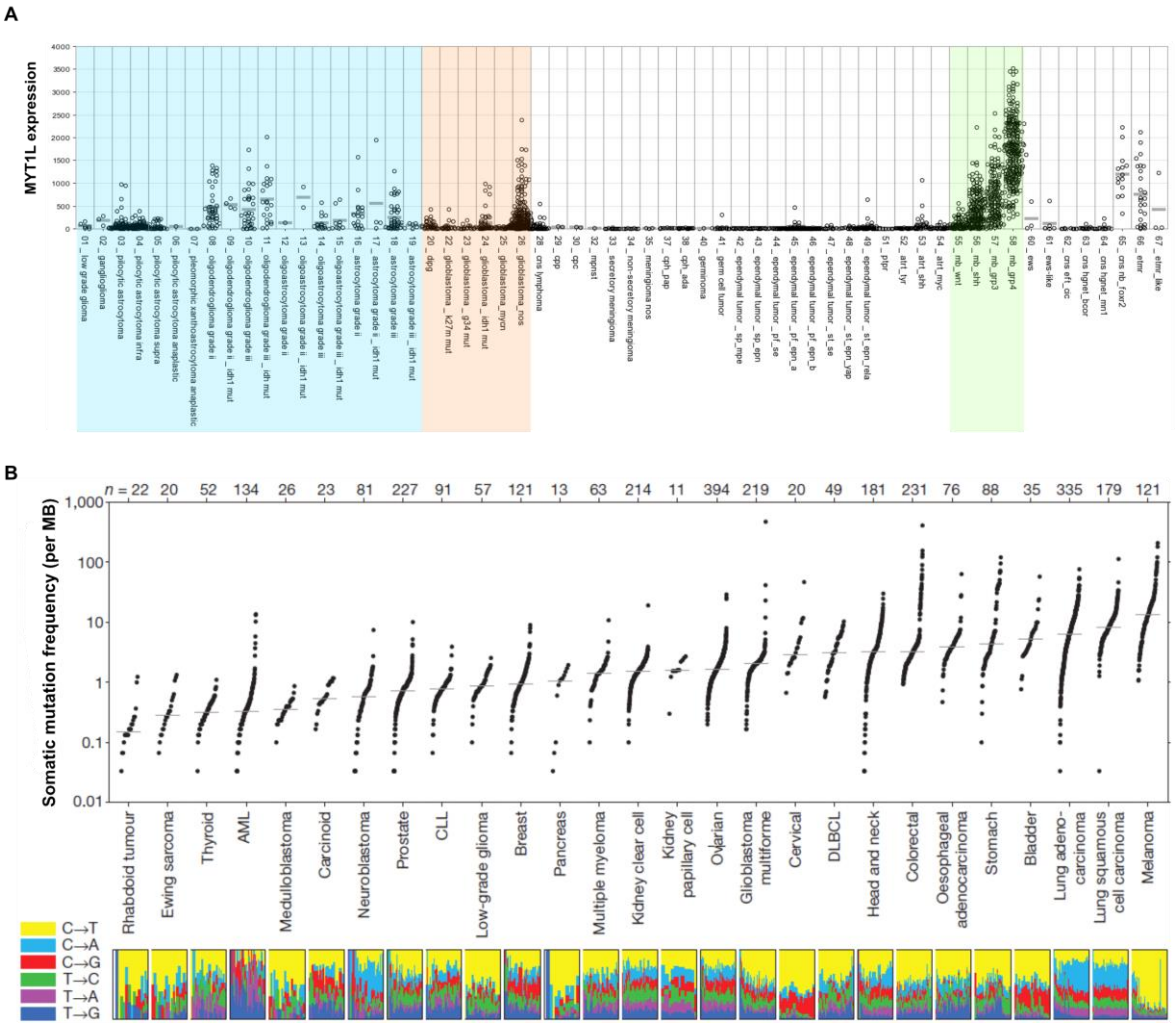

Supp. Figure 1: Expression on *MYT1L* in brain cancer and general mutation frequency of *MYT1L* in cancer. (A) Expression of *MYT1L* in DKFZ brain cancer databases. The highest expression was observed in some gliomas (marked in blue), GBM (red) and especially medulloblastoma (green). Data provided by Marcel Kool (DKFZ Heidelberg). (B) Frequency (mutations/Mb) of somatic mutations in whole exomes across various cancers.

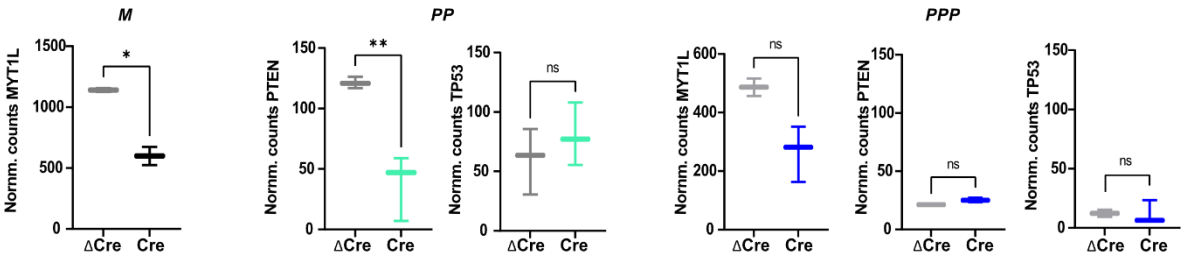

Supp. Figure 2: Normalized counts

Analysis of normalized counts of respective target genes *Myt1l, Pten* and *Tp53* in mouse models *Myt1lflox (M), Pten Tp53 flox (PP)* and *Pten Tp53 Myt1l flox (PPM)* mice. Bulk RNA-sequencing was performed of FACS-sorted GFP-positive nuclei isolated from mice intracranial injected with AAV-Syn-GFP-Cre or AAA-Syn-GFP-ΔCre. n(*M*+SynCre)=2 ; n(*M*+SynΔCre)=2; n(*PP*+SynCre)=3; n(*PP*+SynΔCre)=3; n(*PPM*+SynCre)=4 ; n(*PPM*+SynΔCre)=2.

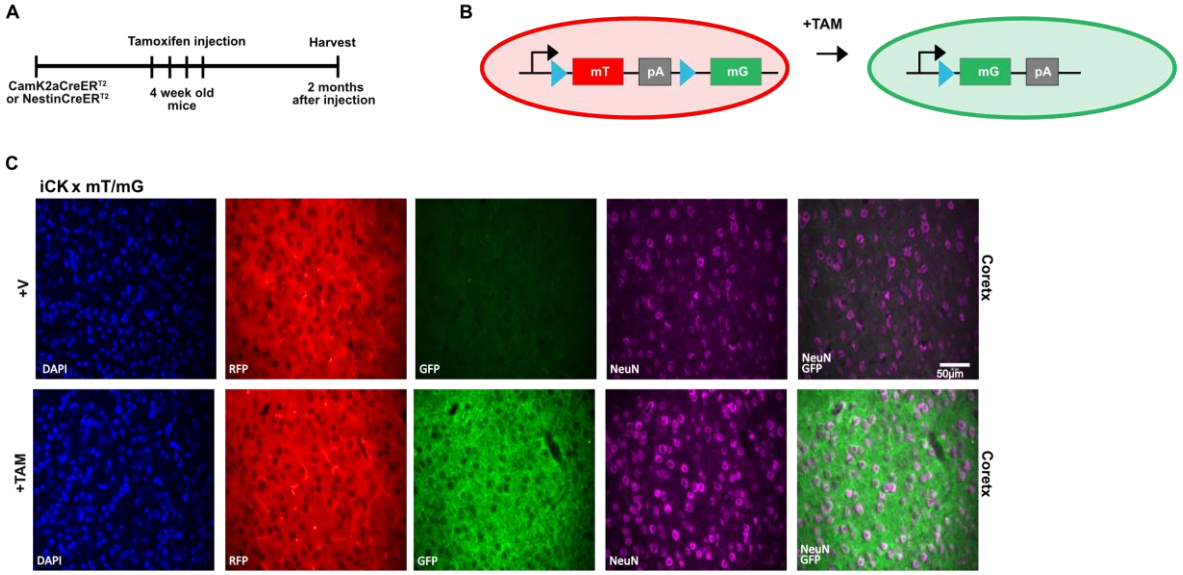

Supp. Figure 3: CamK2a-creERT2 mT/mG and Nestin-creERT2 mT/mG reporter mouse lines

(A) Timeline of tamoxifen/vehicle injection in CamK2a-creERT2 mT/mG and Nestin-creERT2 mT/mG reporter and analyses. (B) Schematic diagram of the mT/mG construct before and after Cre-mediated recombination. mT/mG reporter mice consist of a Camk2a or Nestin promoter driving a loxP-flanked coding sequence of membrane-targeted tandem dimer Tomato (mT) resulting in tdTomato expression with membrane localization. Tamoxifen (TAM) injections induces Cre-mediated recombination and the mT sequence is excised allowing the expression of membrane-targeted enhanced green fluorescent protein (mG). (C) Immunofluorescence staining of CamK2a-creERT2 mT/mG reporter brain sections one month after induction confirms successful reconstitution upon tamoxifen (TAM) injection shown by GFP expression in the highly positive cortex region. Scale bar 50 µm.

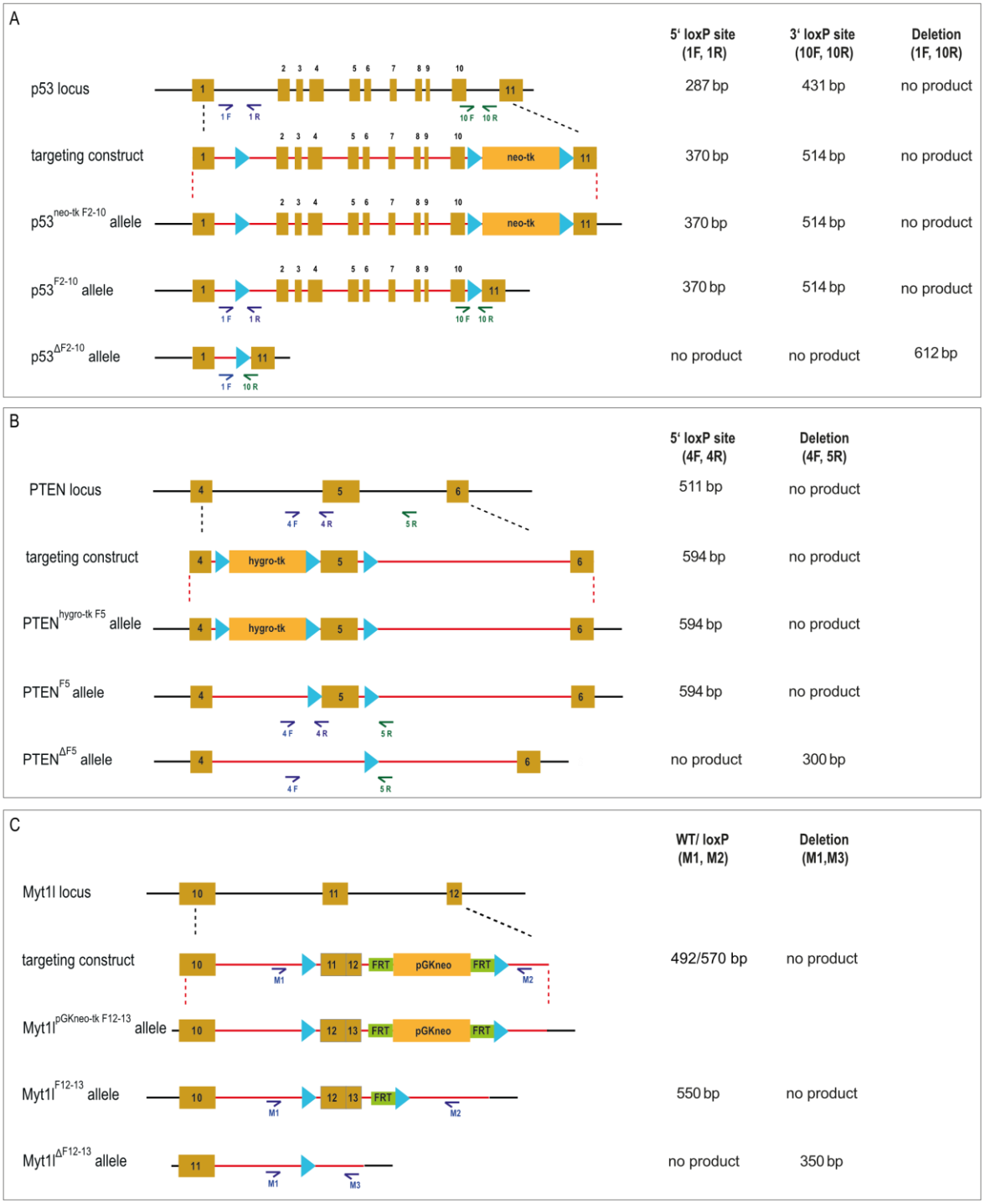

Supp. Figure 4: Design of conditional mouse lines Tp53 flox, Pten flox, and Myt1l flox
(A)Design of conditional mouse line Tp53 flox: Exons 2-10 are flanked by loxP sites. (B) Design of conditional mouse line Pten flox: Exon 5 are flanked by loxP sites. (C) Design of conditional mouse line Myt1l flox: Exons 11 and 12 are flanked by loxP sites. For each line binding sites of primers are shown used for genotyping. Blue triangle: LoxP sites; orange boxes: Exons; green box: FRT sequence elements; neo-tk: neomycin phosphotransferase-thymidine-kinase; hygro-tk: hygromycin- thymidine-kinase; pGKneo: phosphoglycerate kinase I promoter driving the neomycin phosphotransferase gene.

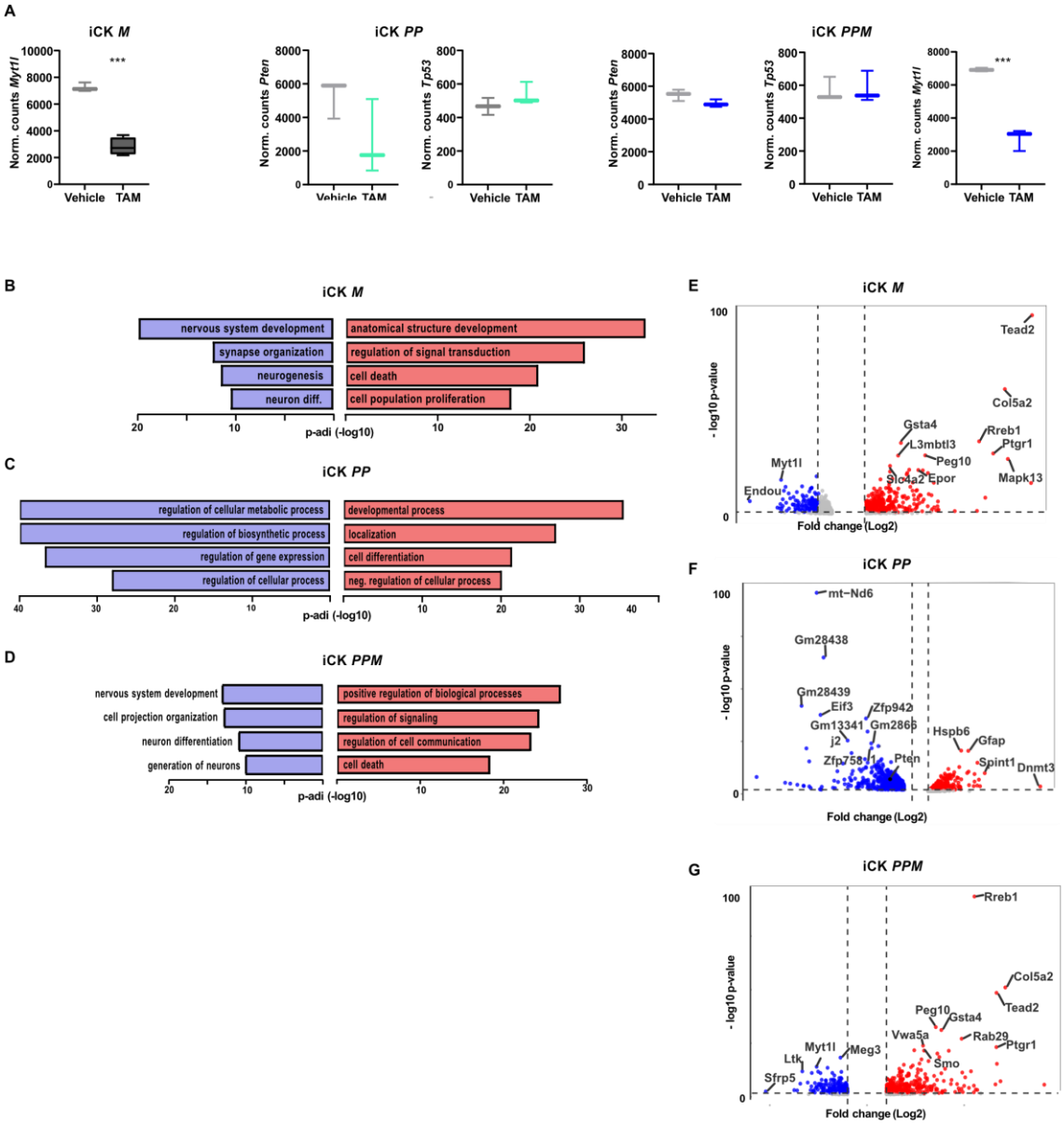

Supp. Figure 5: Gene expression analysis of iCK mouse model

Bulk RNA-sequencing was performed of cells isolated from the prefrontal cortex 4 weeks after injection of Camk2a-creER^{T2} (iCK) Myt1l (M), iCK Pten Tp53 flox (PP) and iCK Pten Tp53 Myt1l flox (PPM) mice. (A) Analysis of normalized counts of respective target genes Myt1l, Pten and Tp53. Myt1l was significantly reduced in iCK M and iCKPPM model. (B-D) Selected top gene ontology (GO) terms and p-adj values. (E-G) Volcano plot or upregulated and downregulated genes. Log2-fold chance >|0.5|; p-adj. <0.01. n(iCK M + TAM)= 4; n(iCK M + V)= 3 ; n(iCK PP +TAM)=2; n(iCK PP +V)=3; n(PPM +TAM)=3; n(PPM +V)=3.

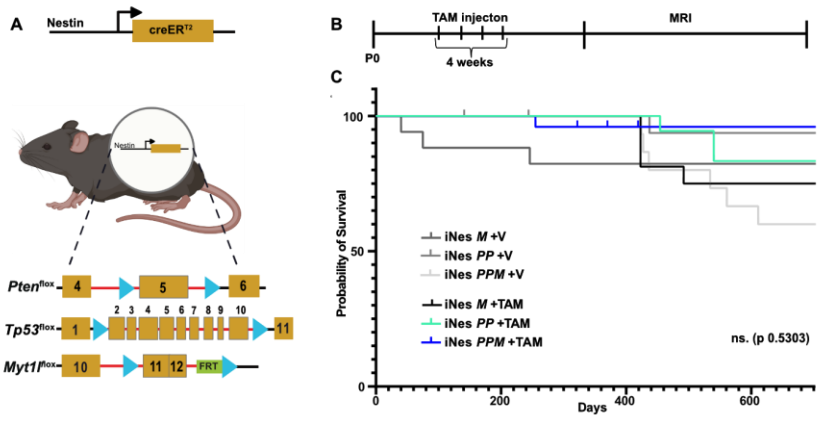

Supp. Figure 6: Destabilization of neuronal fate in progenitor cells
(A) Cartoon of Nestin-creER^{T2} driven mouse model. Tamoxifen injection results in depletion of the respective exons in the models Nestin-creER^{T2} Myt1l flox (iNes M), iNes Pten Tp53 flox (PP) and iNes Pten Tp53 Myt1l flox (PPM). (B) Timeline of Tamoxifen (TAM)/Vehicle injection and analyses. (C) Kaplan-Meier curves for TAM treated and Vehicle mice. Low-rank (Mantel-Cox) test; ns.= not significant.

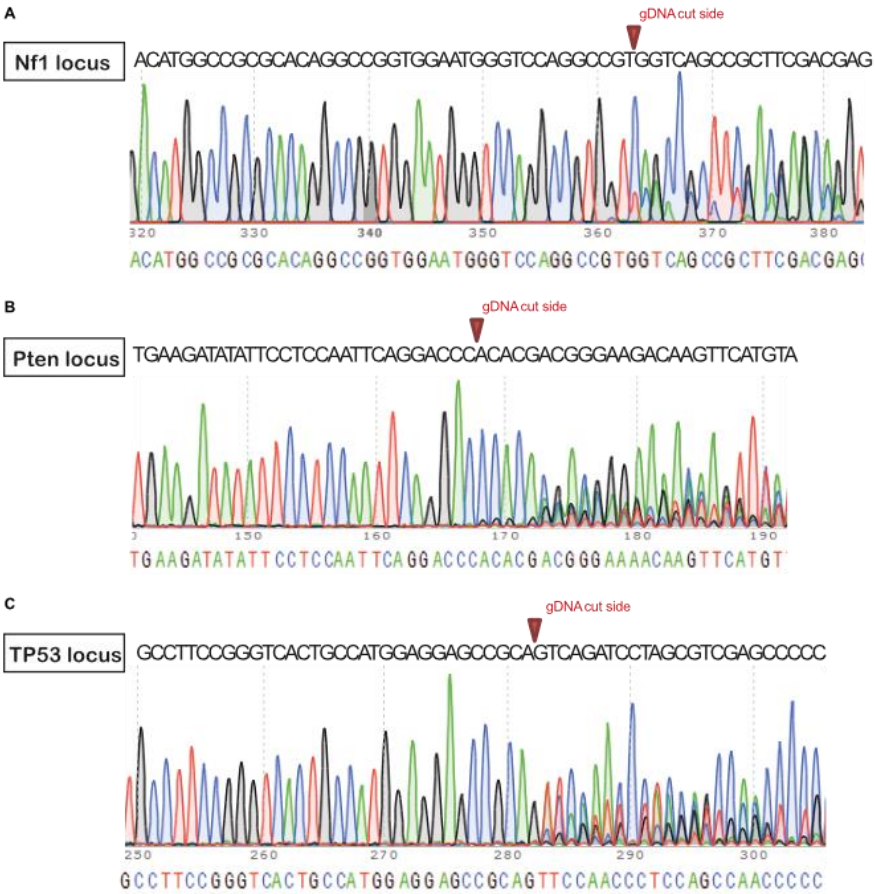

Supp. Figure 7: sgRNA cut sides in respective gene loci of NF1, PTEN and TP53
Sanger sequencing results of genomic DNA, isolated at day 7 from human embryonic stem cells (hESCs) after lentiviral transfection. (A) Red arrow shows cut side of sgNF1 within the Nf1 locus. (B) Red arrow shows cut side of sgPTEN within the PTEN locus. (C) Red arrow shows cut side of sgTP53 within the TP53 locus.

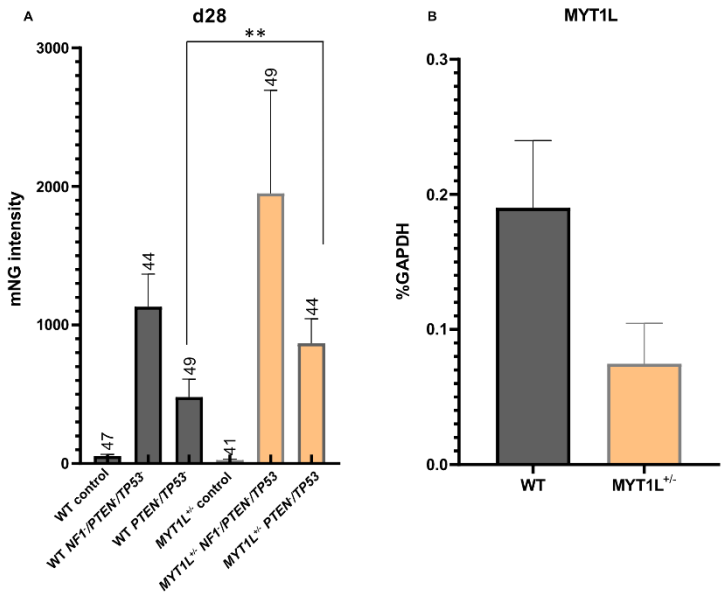

Supp. Figure 8: MYT1L depletion promotes tumour-like growths in organoids

(A) Quantification of mNeonGreen (mNG+) clonal expansion in cerebral organoids at day 28 after tumor suppressor mutagenesis in WT cerebral organoids or organoids with a heterozygous depletion of MYT1L (*MYT1L*$^{+/-}$). Increased mNG intensity in tumor organoids with reduces MYT1L levels was observed. Left to right: WT control (n=47), WT *NF1-/-PTEN-/-TP53-/-* (n=44), WT *PTEN-/-TP53-/-* (n=49), *MYT1L*$^{+/-}$ control (n=41), *MYT1L*$^{+/-}$ *NF1-/-PTEN-/-TP53-/-* (n=49), *MYT1L*$^{+/-}$ *PTEN-/-TP53-/-* (n=44); 4 batches. ** p < 0.01. (B) MYT1L protein level reduces in mNG+ cells, isolated form WT and *MYT1L*$^{+/-}$ cerebral organoids.

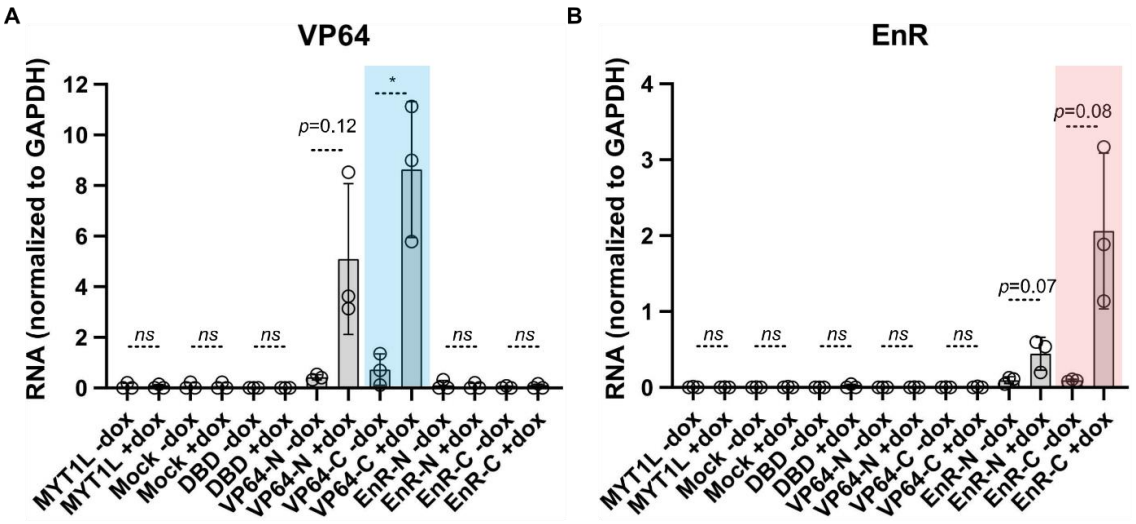

Supp. Figure 9: RNA expression of fusion constructs

(A) RNA expression of VP64 activator fusion construct after 7 days of induction of S24 tdTomato spheroids. In blue: Used VP64 C-terminus fusion construct. (B) RNA expression EnR repressor fusion construct after 7 days of induction of S24 tdTomato spheroids. In red: Used EnR C-terminus fusion construct. (A+B) The C-terminus constructs displayed higher expression than the N-terminus constructs. For that reason, the C-terminus fusion contructs were selected for the performed assays. (n = 3-4 biological replicates), normalized to GAPDH. Bar graphs represent mean values, error bars = s.d., two-sided t-tests; * p < 0.05, **, p < 0.01, ns = not significant.

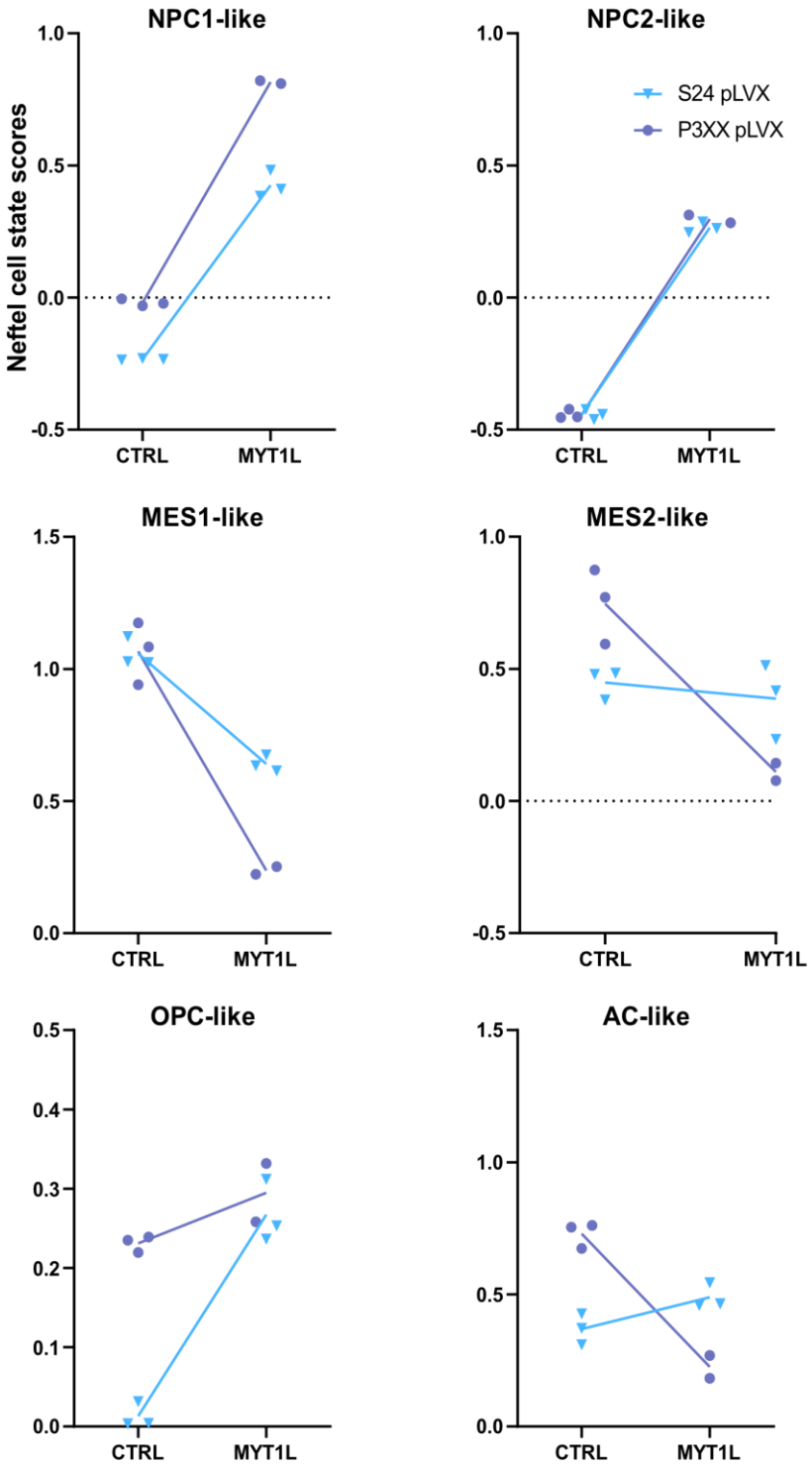

Supp. Figure 10: MYT1L induces changes in GBM subtype identity scores
Glioblastoma Neftel cell state scores for S24 (CTRL n = 3, MYT1L n = 3), and P3XX (CTRL n = 3, MYT1L n = 2). RNA-seq data analysis by Ling Hai. Line indicates mean.

7.2 Declaration

I hereby declare that I have written and submitted the dissertation “The role of MYT1L in brain cancer formation, progression and plasticity” myself and in this process have not used any other sources than those expressly indicated.

I hereby declare that I have not applied to be examined at any other institution, nor have I used the dissertation in this or any other form at any other institution as an examination paper, nor submitted it to any other faculty as a dissertation.

Date Elisa Heinzelmann

7.3 Acknowledgments

Here I am, writing the last sentences of my PhD thesis and try to find words to thank all the people who supported me during this time. A time full of challenges and hurdles that I had to accept and overcome – to finally celebrate the success. Many people have played a large part in this journey, for which I want to say thank you!

First of all, I want to thank all the fantastic present and past members of the Mall lab. Without you great colleagues, my time as a PhD would have been a lot harder. Thank you for making my PhD time fun, with all the scientific input, serious PhD meetings and evening pleasures!

I thank Moritz Mall for offering me a position in his lab, supporting me to become a confident and proud scientist. I want to acknowledge all members of the “team cancer” for the great team spirit, all the exciting collaborative experiments, and for sharing the excitement about MYT1L. At this point I would like to name a few people of the Mall lab and the team cancer, whom I would like to say a special thank you: Betti, Jana, Bryce, Manu, Jule und Laura – our PhD crew (plus our Post-doc Taishi), for sharing all the up and downs but also all the memorable and exciting moments. Lea, Felix, Heather, Mona and Maria-Luisa – who gave me amazing support in my project. Sophie, Dirk and Erik – the GBM experts and great collaborators. And Sarah and Tim for their technical support.

I want to thank the center for preclinical research, in particular the animal care takers, the DKFZ core facilities for light microscopy, the NGS core facility, and the Single Cell Sequencing-Open Lab.

I also want to thank my Thesis Advisory Committee, Prof. Dr. Henrik Kaessmann, Prof. Dr. Peter Angel, Dr. Lui Haikun and Dr. Moritz Mall.

The most special thanks go to my family and friends, who are always there for me. Most important, Mama, Papa und Lea - I don't know what to do without you! And finally, I want to thank Manu for always being there for me, keeping me warm, wiping away my tears and making me laugh again. I’m happy to share all future adventures with you!